Order Number 9304689

Picosecond photoluminescence from semiconductors under static and dynamic stress

Lee, Shun, Ph.D.

City University of New York, 1992

U·M·I
300 N. Zeeb Rd.
Ann Arbor, MI 48106

PICOSECOND PHOTOLUMINESCENCE FROM SEMICONDUCTORS UNDER STATIC AND DYNAMIC STRESS

by

SHUN LEE

A dissertation submitted to the Graduate Faculty in Physics in partial fulfillment of the requirements for the degree of Doctor of Philosophy, The City University of New York.

1992

This manuscript has been read and accepted for the Graduate Faculty in Physics in satisfaction of the dissertation requirement for the degree of Doctor of Philosophy.

8/7/92
Date

Robert R Alfano
Chair of Examining Committee

9/22/92
Date

Joseph B. Xiong
Executive Officer

Prof. Ping P. Ho

Prof. Fred H. Pollak

Prof. Kai Shum

Supervisory Committee

The City University of New York

Abstract

PICOSECOND PHOTOLUMINESCENCE FROM SEMICONDUCTORS UNDER STATIC AND DYNAMIC STRESS

by

SHUN LEE

Advisor: Professor R. R. Alfano

In this thesis, picosecond laser generated shock waves are used to apply stress to a semiconductor. The effects of dynamic (shock) compression on the semiconductors Gallium Selenide, Cadmium Selenide, and Gallium Arsenide are studied using photoluminescence techniques. The stress dependence of the radiative lifetimes in Gallium Arsenide is also studied with time resolved photoluminescence experiments.

In the shock compression experiments on Gallium Selenide, the spontaneous and stimulated photoluminescence is attributed to an exciton exciton scattering mechanism. The shock compression changes the band gap. The line broadening is related uniquely to the transient nature of shock compression.

The shock profile has been measured in shock compression experiments on Cadmium Selenide. The time evolution of the stress components from a shock wave propagating along the [001] direction in Gallium Arsenide is obtained from

the splittings and shifts of the photoluminescence spectra. The first observation of shock compression of a Gallium Arsenide quantum well along its growth direction has been observed.

Static uniaxial compression experiments are performed to study the hole dynamics in Gallium Arsenide. Three major strain effects have been observed in this time and frequency resolved photoluminescence experiment. The lines associated with the two topmost valence subbands shift with stress. The stress dependence of the effective mass causes an enhancement of the absorption coefficient. The photoluminescence has a nonexponential time dependence. The bimolecular recombination coefficient B is independent of stress, while the recombination constant A has the stress dependence of the matrix elements. It is found that the effective lifetime of the v1 holes decreases as a function of stress.

Acknowledgements

I am grateful to my parents, family, and friends for their support and encouragement. I would like to thank Professors Robert R. Alfano, Robert H. Callender, Ping P. Ho, Fred H. Pollak, Kai Shum, and Dr. Shing S. Yao for their guidance. I would especially like to thank Professor Robert R. Alfano for his helpful suggestions and encouragement. Much thanks to Professors Robert H. Callender and William Miller for encouraging me to become a physicist. I would like to thank Dr. Apostolos G. Doukas, Dr. Mitra Dutta, Dr. Rohana Garuthara, Dr. Paul Harris, Dr. Xing Z. Lu, and Mr. Hao Qiang for their help, support, and encouragement. Also, much thanks to my friends and colleagues at the Institute of Ultrafast Spectroscopy and Lasers and the physics department of the City College of the City University of New York for their help and encouragement.

I gratefully acknowledge support from the Office of Naval Research, Hamamatsu Photonics K. K., the Institute of Ultrafast Spectroscopy and Lasers, the City College and the Graduate School of the City University of New York, the NY State-Funded University Fellowship, and the Marshak Fellowship.

Table of Contents

List of Figures

I. Introduction

1.1 Thesis Statement

In this thesis, the effects of dynamic stress on the semiconductors Gallium Selenide (GaSe), Cadmium Selenide (CdSe), and Gallium Arsenide (GaAs) are investigated using a pump-probe photoluminescence technique. Using this novel technique, shock compression effects that can be observed are:

(1) the picosecond laser generated shock wave duration;

(2) the time behavior of the stress components of the shock wave; and

(3) the motion of the semiconductor lattice behind the shock front, and its influence on the carrier dynamics.

The application of static compressive uniaxial stress is expected to change the carrier dynamics. In this thesis, the lifetimes of the holes in GaAs and its dependence on static compressive uniaxial stress are studied using energy and time resolved photoluminescence spectroscopy.

1.2 Introduction to Thesis

Over the past three decades, systems composed of semiconductor materials have attracted a tremendous amount of experimental and theoretical investigations. Stress, which is defined as the force per unit area, is an useful concept in describing the dynamics of 3-dimensional systems. Studies of stressed semiconductors not only provide information about the behavior of semiconductors under stress but also help to improve the theoretical understanding of unstressed semiconductors (see for example the reviews by Paul,[1] Hamann,[2] Pollak,[3] Murri *et. al.*,[4] Martinez,[5] Jayaraman,[6] and Pollak[7]). An introduction to static stress and its influence on the electronic properties of semiconductors is given in chapter II of this thesis.

Stress in a semiconductor can be generated in many ways; from stressing the sample between two levers[8] or two diamonds,[6] to stress from the difference in expansion coefficients[9] or lattice spacings.[10] Another way of applying stress is to generate shock waves. A shock wave is characterized by a shock front. A shock front is a narrow boundary moving with supersonic speed which separates a region under stress from the original unstressed region (see figure 1.2.1). Shock waves are described in chapter III of this thesis. One method of generating shock waves is to use ultrafast laser pulses.[11,12] An introduction to laser generated shock waves is given in chapter III of this thesis.

In this thesis, picosecond laser generated shock waves are used for dynamic compression of the semiconductors GaSe, CdSe, and GaAs. Stress causes changes

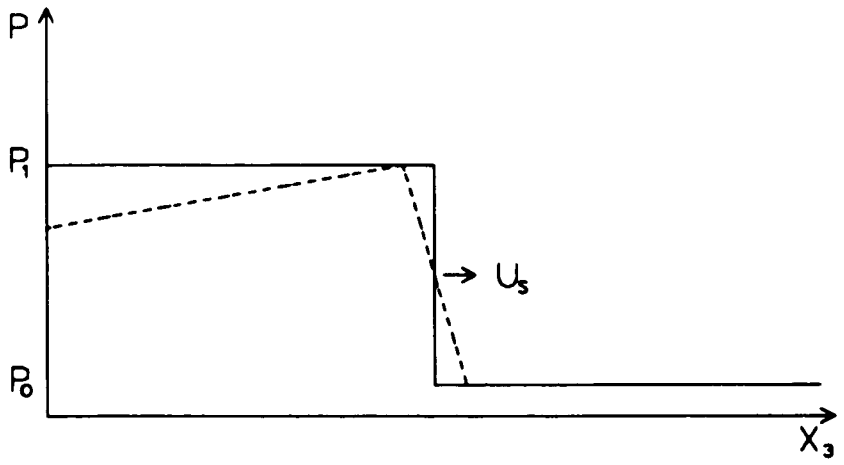

Figure 1.2.1. Schematic representation of a shock wave. The shock front of both the idealized (—) and the realistic (---) shock wave is propagating with speed U_S along the x_3 axis of a sample.

in the semiconductor lattice. This in turn causes the semiconductor band structure as well as the associated wave functions to change. These stress induced changes causes the photoluminescence (PL) to change. Using a pump probe PL technique, these stress induced changes can be monitored. In addition to the band edge shifts which have already been observed under static compression, new phenomena unique to dynamic compression via shock waves can be observed. One such phenomena is the evolution of the stress components parallel (longitudinal stress component) and perpendicular (transverse stress components) to the direction of shock propagation in a semiconductor lattice. The effects of shock compression on GaSe, CdSe, and GaAs are discussed in chapter IV of this thesis.

This thesis is organized into six chapters. In the second chapter, there is an introduction to static stress research together with the relevant mathematical background for stress and strain. This is followed by an introduction to the use of shock waves as a method for applying stress with particular focus on using a laser to generate the shock compression, in chapter III. In chapter IV, the results of PL experiments of GaSe, CdSe, and GaAs under stress are presented. In section 4.2, the effects of shock compression of GaSe are explained in the framework of an exciton exciton scattering theory. In section 4.3, the shock profile in CdSe is obtained from the shifts in the transitional energies under stress. This experiment also suggests the possibility of monitoring both the longitudinal and transverse stress components of the shock wave in GaAs. The main focus of this thesis is on GaAs. In section 4.4, the determination of the time evolution of the transverse and

longitudinal stress components of the shock wave in GaAs is presented. In section 4.5, the hole dynamics in GaAs under static uniaxial compression which have been studied via time resolved PL are presented. What has been learn during this thesis research are summarized in chapter V. Finally, possible future research suggested by this thesis are indicated in chapter VI.

II. Static Stress

2.1 Introduction

In the study of the dynamics of macroscopic objects, the forces applied to an object are usually distributed over finite areas. It is therefore useful to introduce the concept of stress (which is defined as the force per unit area). Typical units of stress are $1kbar = 0.1GPa = 10^8 N\,m^{-2} = 10^9 dyne\,cm^{-2} = 1.45\times10^4 psi = 1.45\times10^4 lb\,in^{-2} = 2.09\times10^6 lb\,ft^{-2} = 7.5\times10^5 torr = 7.5\times10^5 mm\,Hg = 987 atm$.

Application of stress to an object results in deformation (and perhaps motion) of the object. Consider for example the unstressed cubic isotropic object (with dimensions $L\times L\times L$) which is shown in figure 2.1.1a, application of a uniform stress (in the x_3 direction) to the object causes the cubic solid to deform (see figure 2.1.1b). Under stress, the object's new dimensions are $[L + \Delta L_1]\times[L + \Delta L_2]\times[L + \Delta L_3]$, where $\Delta L_i \equiv \varepsilon_{ii} L$ is the change in L along the i axis and a new quantity known as the strain (ε_{ii}) has been introduced. Strain is the fractional change in the length in a object. Note[13] that a positive strain implies an increase in the length of the object. The mathematical formulation of strain and stress is described in detail in the next section (2.2).

Strain causes structural, electrical, and optical properties of semiconductors to change. The various semiconductor properties which change under stress[14] are for example: removal of degeneracies,[15-17] shifts in the band edges,[18-23] and changes

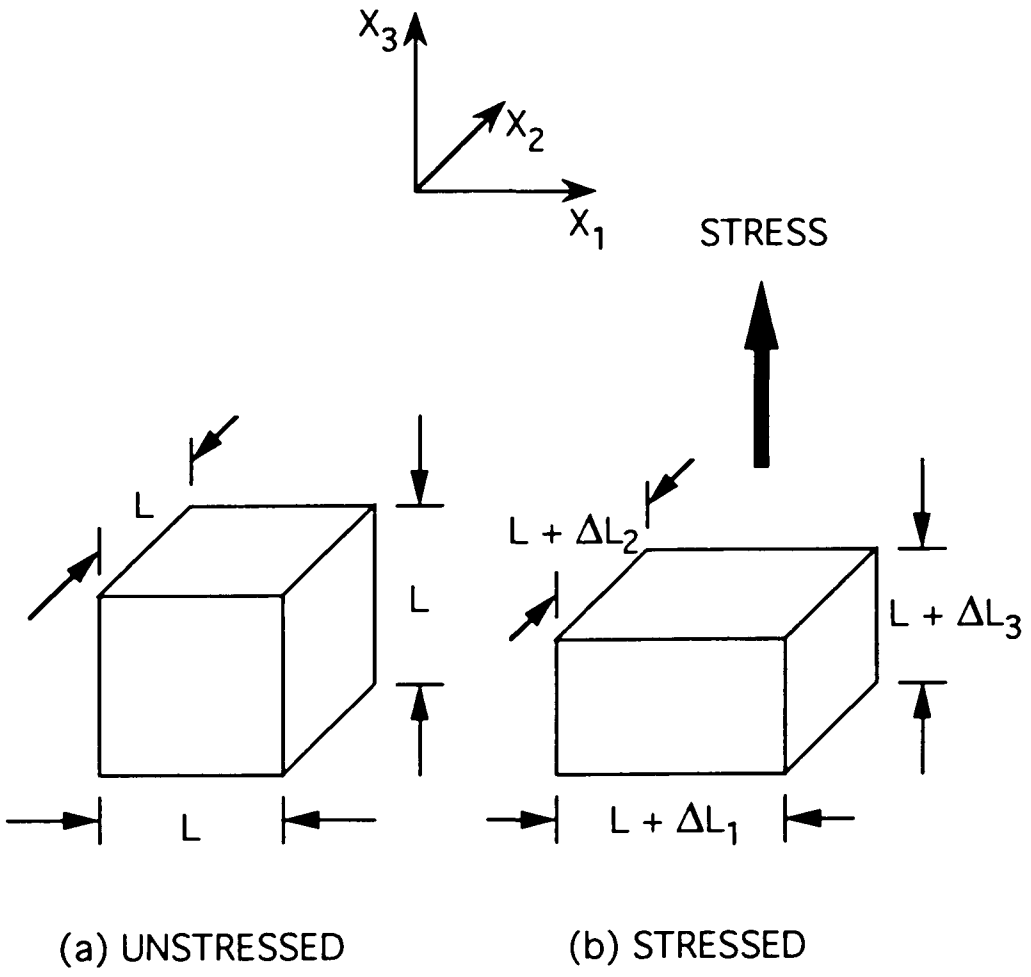

Figure 2.1.1. A schematic representation of a) unstressed and b) stressed object.

in the curvatures (effective masses)[14,24-32] of the electronic band structure. Other effects of strain in a semiconductor include changes in the interband matrix elements,[14,33,34] as well as changes of the vibrational modes.[35-37]

To obtain a physical picture of how strain influence the electronic and vibrational properties of semiconductors, consider a semiconductor with a simple cubic lattice. The lattice constant $d_1 = d_2 = d_3 = d_o$ is determined by the minimum in the potential energy of the semiconductor crystal (see figure 2.1.2a). Consider a semiconductor stressed along the x_3 axis, so that the new lattice constant along the x_3 axis is $d_3' > d_o$. Under stress, the potential energy plotted as a function of the x_1 (or x_2) lattice constant (see figure 2.1.2b) still has the same general shape as shown in figure 2.1.2a. In general, the minimum of the curve does not occur at d_o and the new lattice constant for the $x_1 - x_2$ planes then becomes $d_1' = d_2' = d_{\perp}$. Therefore, there will be a decrease in the length along the x_1 (x_2) axis for $d_{\perp} < d_o$, (or conversely, an increase in length for $d_{\perp} > d_o$).

These changes in the lattice constants and lattice type (i.e., the original simple cubic lattice is distorted into a tetragonal lattice) cause the electronic and vibrational band structure to change. This is due to the dependence of the electronic and vibrational band structure on the (lattice) potential. Consider the simplified example of a chain of three ions (see figure 2.1.3a), the ion in the center is under the influence of the force from the two end ions. For small deviations from the equilibrium position, the restoring force (F or potential ϕ) experienced by the central ion can be

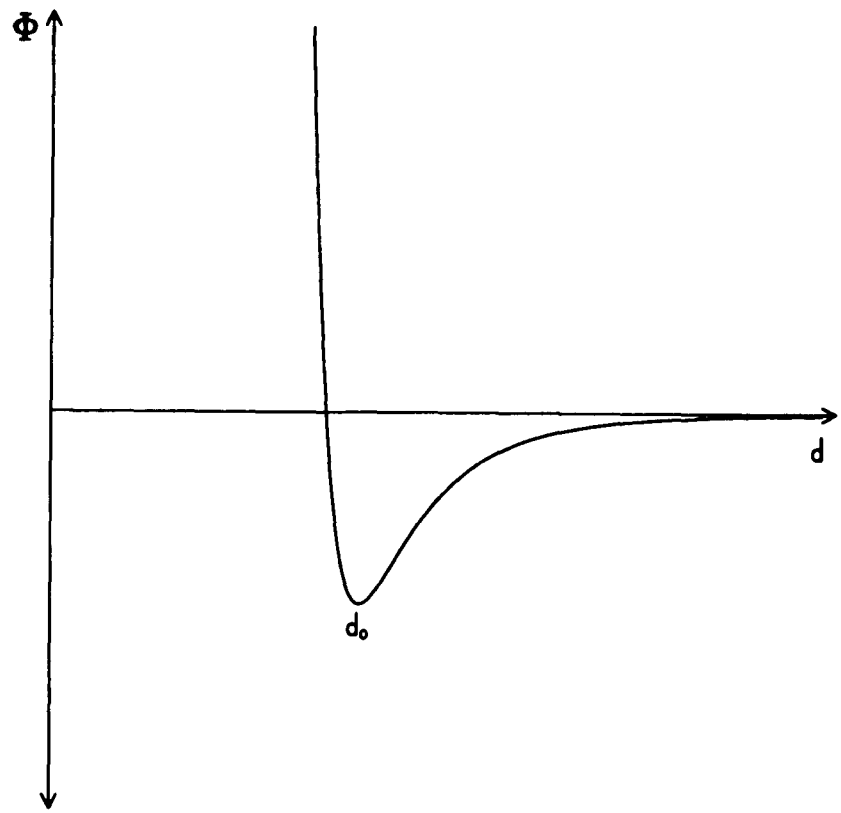

Figure 2.1.2a. A plot of the potential energy as a function of the lattice constant for an unstrained crystal.

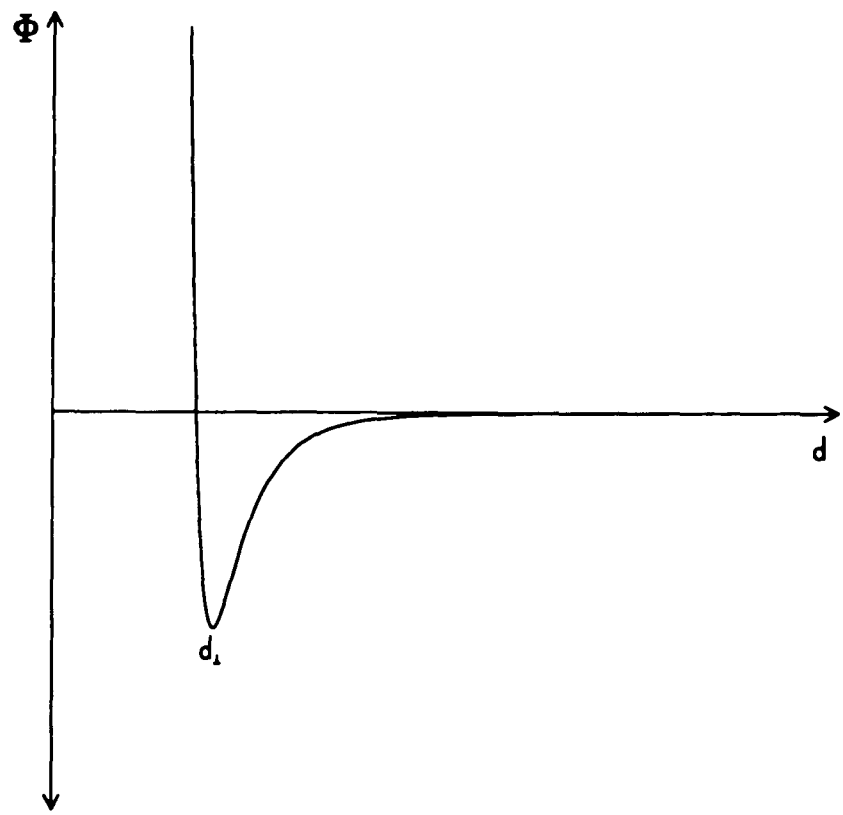

Figure 2.1.2b. A plot of the potential energy as a function of the lattice constant for a strained crystal.

approximated by $F = kx \equiv -\nabla\phi$. It is immediately obvious that when the separation between the ions decrease (see figure 2.1.3b), the restoring force (F' or potential ϕ') on the central ion has been changed to $F' = k'x \equiv -\nabla\phi'$. This implies that for a semiconductor under strain, the vibrational modes change (due to $k' \neq k$) and the electronic band structure changes (due to $\phi' \neq \phi$). Of course, the situation in a 3-dimensional lattice is much more complicated but this physical picture is still applicable.

This simple three ion chain model can be the basis for the analysis of a 3-dimensional crystal. However, the number of coupled equations involved will be tremendous and at present, impossible to solve (without simplifications). Researchers have therefore devised alternate schemes for calculating the band structure. One enormously successful technique is to formulate a Hamiltonian for the semiconductor crystal using group theory. This approach is based on a very powerful idea. Consider a system which have certain symmetries (e.g., the system rotated by 90° is identical to the original system), the equation(s) describing this system must also have these symmetries, otherwise, the equation(s) do not accurately describe this system.[38] (Note,[13] the equation(s) must include the symmetry of the system but it is possible for the equation(s) to possess more symmetry than the system.) Therefore, the strain Hamiltonian can be written as the sum of products (of various operators of interest) which are invariant under the symmetry of the system. For example, $H_\varepsilon = \sum_i D_i[L_k, \bar{\sigma}_l, \varepsilon_{mn}]$, where $\mathbf{L}$ is the orbital angular momentum operator, $\bar{\sigma}$ is the spin angular momentum operator, ε_{ij} is the strain tensor, and D_i are constants.

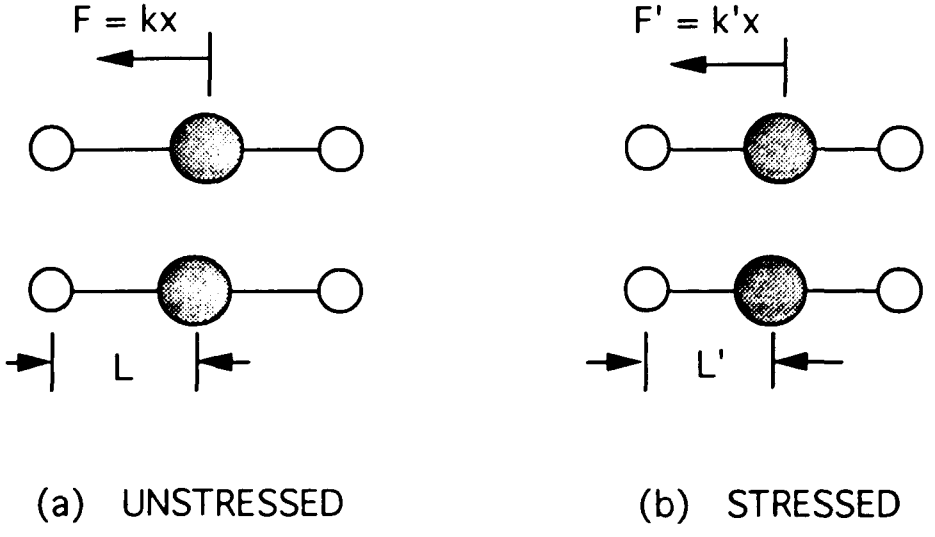

Figure 2.1.3. Schematic representation of a) unstrained, and b) strained chain of three ions.

Using this technique, the strain Hamiltonians for cubic and wurzite lattices have been constructed by Pikus,[39] Kleiner and Roth,[15] Pollak,[19] Suzuki and Hensel,[28] and Cho.[40] For example, the strain Hamiltonians for zincblend materials are[19]

$$H_c = -a_c^z \left(\varepsilon_{11} + \varepsilon_{22} + \varepsilon_{33} \right) , \tag{2.1.1a}$$

$$H_{orb} = a_1^z \left(\varepsilon_{11} + \varepsilon_{22} + \varepsilon_{33} \right) + 3b_1^z \left[\varepsilon_{11} \left(L_1^2 - \frac{1}{3} L^2 \right) + c.p. \right]$$

$$+ 2\sqrt{3} d_1^z \left[\varepsilon_{12} \{ L_1, L_2 \} + c.p. \right] , \tag{2.1.1b}$$

and

$$H_{spin} = 2a_2^z \left(\varepsilon_{11} + \varepsilon_{22} + \varepsilon_{33} \right) \mathbf{L} \cdot \bar{\sigma} + 6b_2^z \left[\varepsilon_{11} \left(L_1 \bar{\sigma}_1 - \frac{1}{3} \mathbf{L} \cdot \bar{\sigma} \right) + c.p. \right]$$

$$+ 2\sqrt{3} d_2^z \left[\varepsilon_{12} (L_1 \bar{\sigma}_2 + L_2 \bar{\sigma}_1) + c.p. \right] , \tag{2.1.1c}$$

where a_c^z, a_1^z, a_2^z, b_1^z, b_2^z, d_1^z, and d_2^z are the deformation potentials, ε_{ij}'s are the strain components, $\mathbf{L}$ and $\bar{\sigma}$ are the orbital and spin angular momentum operators, respectively. It is interesting to note that the strain Hamiltonians for the valence band use the orbital and spin angular momentum operators instead of the total angular momentum operator ($\mathbf{J}$). Using the total angular momentum operator in the construction of the strain Hamiltonian implies that the coupling between the $\left[J = \frac{3}{2}, J_3 = \frac{1}{2} \right]$ and $\left[J = \frac{1}{2}, J_3 = \frac{1}{2} \right]$ wave functions can be neglected.

The total Hamiltonian for zincblend materials can be written as[14]

$$H = H_k + H_{so} + H_c + H_{orb} + H_{spin} + H_{exc} \quad , \tag{2.1.2}$$

where

$$H_k = -\frac{\hbar^2}{2m}\nabla^2 + V(r) + \frac{\hbar^2 k^2}{2m} + \frac{\hbar}{m}\mathbf{k}\cdot\mathbf{p} \quad , \tag{2.1.3}$$

$$H_{so} = \frac{\Delta_o}{3}\left[2\mathbf{L}\cdot\bar{\sigma} - 1\right] \quad , \tag{2.1.4}$$

H_{exc} is the exciton Hamiltonian, and Δ_o is the spin-orbit splitting. From the strain Hamiltonians 2.1.1a, 2.1.1b, and 2.1.1c and the spin-orbit interaction Hamiltonian 2.1.4, the stress induced shifts of the band edges can be calculated using perturbation theory. This is described in detail in sections 4.3 and 4.4.

For certain experimental conditions, excitons can have a strong influence on the experimental observations. The exciton part of the Hamiltonian can be written as[41]

$$H_{exc} = E_b^{ex} + \frac{\Delta_{ex}}{2}\bar{\sigma}_h\cdot\bar{\sigma}_c \quad , \tag{2.1.5}$$

where $\bar{\sigma}_h$ is the valence hole spin angular momentum operator, $\bar{\sigma}_c$ is the conduction electron spin angular momentum operator, Δ_{ex} is the spin exchange parameter, and E_b^{ex} is the exciton binding energy. Note that E_b^{ex} in equation 2.1.5 can be stress dependent. This effect will be seen in the shock compression experiments on GaSe (section 4.2). For the CdSe and GaAs shock compression experiments, no excitons are present and excitons effects need not be considered.

In the semiconductors GaSe, CdSe, and GaAs that are studied in this thesis, there have already been experimental studies of the static stress dependence of the band edges. In GaSe, the changes in the band edges have been studied using photoconductivity,[42] absorption,[43] absorption and transmission,[44] and absorption and PL.[45] In CdSe, the changes in the band edges have been studied with the changes in reflectance.[41,46] In GaAs, the changes in the band edges have been studied using PL,[22,23,47-49] absorption,[50] electroreflectance,[17,33] and photoreflectance.[18] In GaAs quantum wells, biaxial strain has been used to apply a stress along the growth direction.[51] These changes in the band edges will be the dominate feature of the shock compression experiments described in chapter 4.

Strain effects can also influence carrier dynamics. The rate of photon emission due to the transition of an electron from the conduction band to one of the valence bands[52] is

$$\frac{4e^2}{3\hbar c^3} E_{c-v}^2 | < c | \hat{\mathbf{e}} \cdot \mathbf{p} | v > | ^2 \ , \qquad (2.1.6)$$

where E_{c-v} is the separation in energy between the conduction band and the valence band, and $| < c | \hat{\mathbf{e}} \cdot \mathbf{p} | v > | ^2$ is the matrix element for dipole transition from the conduction band to the valence band. It can be seen from equation 2.1.6 that the radiative lifetime is stress dependent via the matrix elements and E_{c-v}. The principle reason for the stress dependence of the matrix elements is due to the modification of the wave functions by the strain Hamiltonian. A specific example of this is shown in appendix A5. The stress dependence of the matrix elements has

been seen[33] from the intensity of the piezo-electroreflectance in GaAs. The stress dependence of the hole lifetimes has been indirect inferred from line shape analysis of resonance Raman scattering in GaAs.[53,54] In this thesis, the stress dependence of the lifetimes of the holes in n-GaAs will be studied using time resolved PL.

2.2 Stress and Strain

In this section, the general theoretical background needed to understand stressed semiconductors will be described. Stress and strain are useful concepts in describing the dynamics of 3-dimensional systems. A "stress" (second rank) tensor σ_{ij} describes the vector force $\vec{f}$ relative to the normal vector of an area $\vec{a}$,

$$\partial f^i \equiv \sigma_{ij}\, \partial a^j \quad . \tag{2.2.1}$$

Note that this can be written as $\sigma_{ij} = \sigma_{ij}^S + \sigma_{ij}^A$, where $\sigma_{ij}^S \equiv \frac{1}{2}\left[\sigma_{ij} + \sigma_{ij}\right]$ is a symmetrical tensor and $\sigma_{ij}^A \equiv \frac{1}{2}\left[\sigma_{ij} - \sigma_{ij}\right]$ is an anti-symmetrical tensor. Similarly, a "strain" (second rank) tensor Ξ_{ij} relates the displacement vector $\vec{u}$ to a corresponding position vector $\vec{x}$,

$$\partial u^i \equiv \Xi_{ij}\, \partial x^j \quad . \tag{2.2.2}$$

This can be written as $\Xi_{ij} = \Xi_{ij}^S + \Xi_{ij}^A$, where $\Xi_{ij}^S \equiv \frac{1}{2}\left[\Xi_{ij} + \Xi_{ij}\right]$ is a symmetrical tensor and $\Xi_{ij}^A \equiv \frac{1}{2}\left[\Xi_{ij} - \Xi_{ij}\right]$ is an anti-symmetrical tensor.

How a system elastically deforms under a force is described by the elastic compliance tensor $\tilde{c}_{ijkl}$ (or the elastic stiffness tensor c_{ijkl}) which relates the stress to the strain,

$$\Xi_{ij} \equiv \tilde{c}_{ijkl}\, \sigma_{kl} \quad , \tag{2.2.3a}$$

or

$$\sigma_{ij} \equiv c_{ijkl}\, \Xi_{kl} \quad . \tag{2.2.3b}$$

Equation 2.2.3 describes the infinitesimal elastic deformation of a solid under an applied stress (Hooke's law). For finite deformations, the relationship between an applied stress and the resultant deformation is no longer linear (i.e., expressions involve a sum of products of Ξ_{ij}). For large stress, the deformation is inelastic (i.e., removal of the applied stress does not totally remove the deformation). However, for the magnitude of stress ($\leq 20kbar$) that is applied in the experiments to be described in chapter 4, equation 2.2.3 is sufficient.

If there are no torques on the system and rotations are not considered,[13,55] then $\sigma_{ij} = \sigma_{ji}$ and $\Xi_{ij} = \Xi_{ji}$, respectively. The elastic compliance tensor is also symmetric. The stress tensor σ_{ij} is then redefine as

$$\sigma_{ij} \equiv \sigma_{ij}^{S} \quad . \tag{2.2.4a}$$

The strain tensor ε_{ij} is then redefine as

$$\varepsilon_{ij} \equiv \Xi_{ij}^{S} = \frac{1}{2}\left[\Xi_{ij} + \Xi_{ji}\right] = \frac{1}{2}\left[\frac{\partial u_i}{\partial x_j} + \frac{\partial u_j}{\partial x_i}\right] \quad . \tag{2.2.4b}$$

By convention, the stress tensor σ_{ij} and the strain tensor ε_{ij} are often written as six-vectors. That is,

$$\mathbf{T} \equiv \begin{bmatrix} \sigma_{11} \\ \sigma_{22} \\ \sigma_{33} \\ \sigma_{23} \\ \sigma_{31} \\ \sigma_{12} \end{bmatrix} \quad \textit{and} \quad \boldsymbol{\varepsilon} \equiv \begin{bmatrix} \Sigma_1 \\ \Sigma_2 \\ \Sigma_3 \\ \Sigma_4 \\ \Sigma_5 \\ \Sigma_6 \end{bmatrix} \quad , \tag{2.2.5a}$$

where the conventional normal strains ($\Sigma_1 \equiv \varepsilon_{11}$, $\Sigma_2 \equiv \varepsilon_{22}$, and $\Sigma_3 \equiv \varepsilon_{33}$) are given

by

$$\Sigma_i \equiv \frac{\partial u_i}{\partial x_i} \quad \text{for } (i = 1, 2, 3) \ , \tag{2.2.5b}$$

and the (engineering) shear components ($\Sigma_4 \equiv 2\varepsilon_{23}$, $\Sigma_5 \equiv 2\varepsilon_{31}$, and $\Sigma_6 \equiv 2\varepsilon_{12}$) are

$$\Sigma_i \equiv \frac{\partial u_j}{\partial x_k} + \frac{\partial u_k}{\partial x_j} \qquad \begin{cases} \text{for } i = 4, & j = 2 \text{ and } k = 3 \\ 5, & 3 \qquad 1 \\ 6, & 1 \qquad 2 \end{cases} . \tag{2.2.5c}$$

The elastic compliance tensor $\tilde{c}_{ijkl}$ is then rewritten as $s_{\nu\mu}$ with $\nu, \mu = 1, 2, 3, 4, 5, 6$. That is,

$$\mathbf{s} \equiv \begin{bmatrix} S_{11} & S_{12} & S_{13} & S_{14} & S_{15} & S_{16} \\ S_{12} & S_{22} & S_{23} & S_{24} & S_{25} & S_{26} \\ S_{13} & S_{23} & S_{33} & S_{34} & S_{35} & S_{36} \\ S_{14} & S_{24} & S_{34} & S_{44} & S_{45} & S_{46} \\ S_{15} & S_{25} & S_{35} & S_{45} & S_{55} & S_{56} \\ S_{16} & S_{26} & S_{36} & S_{46} & S_{56} & S_{66} \end{bmatrix} . \tag{2.2.6}$$

Relationship 2.2.3a is then written as

$$\boldsymbol{\varepsilon} = \mathbf{sT} \ . \tag{2.2.7}$$

For a hydrostatic pressure P, the stress vector has the following form:

$$\mathbf{T} \equiv \begin{bmatrix} -P \\ -P \\ -P \\ 0 \\ 0 \\ 0 \end{bmatrix} . \tag{2.2.8}$$

Consider GaAs for example. The elastic compliance for GaAs is[56]

$$\mathbf{s} \equiv \begin{pmatrix} S_{11}^z & S_{12}^z & S_{12}^z & 0 & 0 & 0 \\ S_{12}^z & S_{11}^z & S_{12}^z & 0 & 0 & 0 \\ S_{12}^z & S_{12}^z & S_{11}^z & 0 & 0 & 0 \\ 0 & 0 & 0 & S_{44}^z & 0 & 0 \\ 0 & 0 & 0 & 0 & S_{44}^z & 0 \\ 0 & 0 & 0 & 0 & 0 & S_{44}^z \end{pmatrix}, \tag{2.2.9}$$

where $S_{11}^z = 1.2\times10^{-3}kbar^{-1}$, $S_{12}^z = -0.4\times10^{-3}kbar^{-1}$, and $S_{44}^z = 1.7\times10^{-3}kbar^{-1}$. For a hydrostatic pressure P, the strains (from equations 2.2.7, 2.2.9, and 2.2.8) are

$$\varepsilon_{11} = \varepsilon_{22} = \varepsilon_{33} = -\left(S_{11}^z + 2S_{12}^z\right)P \tag{2.2.10a}$$

and

$$2\varepsilon_{23} = 2\varepsilon_{31} = 2\varepsilon_{12} = 0 \quad . \tag{2.2.10b}$$

For a $10kbar$ hydrostatic pressure, the strains are $\varepsilon_{11} = \varepsilon_{22} = \varepsilon_{33} = -0.4\times10^{-3}kbar^{-1}(10kbar) = -0.4\%$. Consider a cube of GaAs with dimensions $1\times1\times1cm^3$, under stress the length becomes $l' \equiv l + \Delta l \equiv l + \varepsilon l = 1cm + (-0.004)(1cm) = 0.996cm$. Therefore, the volume becomes $V' = 0.996\times0.996\times0.996cm^3 = 0.988cm^3$. This implies a 1.2% increase in the density of the GaAs sample under a $10kbar$ hydrostatic pressure.

Similarly, the stress vector for a [001] compressive uniaxial stress X has the form:

$$\mathbf{T} \equiv \begin{pmatrix} 0 \\ 0 \\ -X \\ 0 \\ 0 \\ 0 \end{pmatrix} . \tag{2.2.11}$$

Again considering GaAs, the strains using equations 2.2.7, 2.2.9, and 2.2.11 are

$$\varepsilon_{11} = \varepsilon_{22} = -S_{12}^{z} X \quad , \tag{2.2.12a}$$

$$\varepsilon_{33} = -S_{11}^{z} X \quad , \tag{2.2.12b}$$

and

$$2\varepsilon_{23} = 2\varepsilon_{31} = 2\varepsilon_{12} = 0 \quad . \tag{2.2.12c}$$

For a $X = 10kbar$ [001] compressive uniaxial stress, the strain along [001] is $\varepsilon_{33} = -1.2\times10^{-3}kbar^{-1}(10kbar) = -1.2\%$, and the strains perpendicular to [001] are $\varepsilon_{11} = \varepsilon_{22} = 0.4\times10^{-3}kbar^{-1}(10kbar) = 0.4\%$. Considering a cube of GaAs with dimensions $1\times1\times1cm^3$, under [001] stress the length along [001] becomes $l' \equiv l + \Delta l \equiv l + \varepsilon l = 1cm + (-0.012)(1cm) = 0.988cm$. Similarly, the lengths perpendicular to [001] becomes $l' \equiv l + \Delta l \equiv l + \varepsilon l = 1cm - (-0.004)(1cm) = 1.004cm$. The volume under [001] $10kbar$ uniaxial stress becomes $V' = 0.988\times1.004\times1.004cm^3 = 0.996cm^3$. This implies a 0.4% increase in the density of the GaAs sample under a [001] $10kbar$ compressive uniaxial stress.

The stress vector for a compressive uniaxial stress X at an angle θ from [001] axis in the $(1\bar{1}0)$ plane can be obtained by rotating the stress vector 2.2.11. The transformation of a tensor is given by

$$T_{ij} = \left[\alpha^{-1} \right]_{ik} \left[\alpha^{-1} \right]_{jl} \tilde{T}_{kl} \quad , \tag{2.2.13}$$

where for a continuous coordinate transformation, α is simply the 3×3 rotation matrix. The stress vector for a uniaxial stress X at an angle θ from [001] axis in the $(1\bar{1}0)$ plane is

$$\mathbf{T} \equiv \begin{bmatrix} \frac{-X}{2}\sin^2\theta \\ \frac{-X}{2}\sin^2\theta \\ -X\cos^2\theta \\ \frac{-X}{\sqrt{2}}\sin\theta\cos\theta \\ \frac{-X}{\sqrt{2}}\sin\theta\cos\theta \\ \frac{-X}{2}\sin^2\theta \end{bmatrix} . \tag{2.2.14}$$

The linear elastic relationship (2.2.7) between an applied force described by a stress vector (σ_{ij}) and the resultant distortion of the lattice (ε_{kl}) is the basis upon which the shock compression and the static uniaxial stress experiments will be studied.

III. Dynamic Stress

3.1 Shock Waves

A shock wave is defined by the presence of a shock front. A shock front is a boundary moving with supersonic speed. This moving boundary separates two regions which have different thermodynamic parameters. To help clarify this definition of a shock wave, consider an idealized shock wave, where the wave front is stepwise with a uniform pressure region behind it (see figure 1.2.1). The wave front is moving, and the stressed region (with pressure P_1) is growing at the expense of the unstressed region (with pressure P_o). For actual shock waves, this idealized picture of the shock wave is only an approximation. Usually, the shock front has a width of $1nm$ to 10^3nm. The duration of the shock pressure behind the shock front is typically 10^3nm to 10^6nm. In general, the shock pressure profile is nonuniform and nonsteady (i.e., time dependent). Even though the shock wave is nonsteady and nonuniform, it must obey the conservation of mass, momentum, and energy.

For a laboratory or Eulerian coordinate system (i.e., one that is fixed in space),[57] the conservation requirements in a one dimensional system (with no energy sources or sinks) are:

1) mass conservation,

$$\left[\left[\partial_t \rho\right]_{x3} + u\left[\partial_{x3}\rho\right]_t\right] = -\rho\left[\partial_{x3}u\right]_t \quad ; \qquad (3.1.1a)$$

2) momentum conservation,

$$\left[\partial_{x3}\sigma_{33}\right]_t = -\rho\left[\left[\partial_t u\right]_{x3} + u\left[\partial_{x3}u\right]_t\right] \quad ; \text{ and} \qquad (3.1.1b)$$

3) energy conservation,

$$\left[\left[\partial_t E\right]_{x3} + u\left[\partial_{x3}E\right]_t\right] = -\frac{\sigma_{33}}{\rho}\left[\partial_{x3}u\right]_t$$

$$= \left[-\frac{\sigma_{33}}{\rho}\right]\left[-\frac{1}{\rho}\right]\left[\left[\partial_t \rho\right]_{x3} + u\left[\partial_{x3}\rho\right]_t\right] \quad ; \qquad (3.1.1c)$$

where ρ is the density, $u(x, t)$ is the particle velocity, σ_{33} is the stress, E is the energy, $\left[\partial_{x3}\right]_t \equiv \left[\frac{\partial}{\partial x_3}\right]_t$, and $\left[\partial_t\right]_{x3} \equiv \left[\frac{\partial}{\partial t}\right]_{x_3}$.

Another common frame of reference is the Langrangian coordinate system where the coordinate system follows a particle in the flow.[57] In this system, $x_3 \equiv x_3(h, t)$, where x_3 (h) is the particle position at time t $(t = 0)$. The particle velocity is then $u = \left[\partial_t x_3\right]_h$, where $\left[\partial_t\right]_h \equiv \left[\frac{\partial}{\partial t}\right]_h$. Using

$$\left[\partial_t\right]_h = \left[\partial_t\right]_{x3} + u\left[\partial_{x3}\right]_t \quad , \qquad (3.1.2)$$

and the relation between the density ρ and the initial density ρ_o ($\rho dx_3 = \rho_0 dh$ from mass conservation), the conservation requirements in the Eulerian system can be transformed into the Langrangian system. From equation 3.1.1, they are:

1) mass conservation,

$$\left[\left[\partial_t \rho\right]_h\right] = -\rho\frac{\rho}{\rho_0}\left[\partial_h u\right]_t \quad ; \qquad (3.1.3a)$$

2) momentum conservation,

$$\left[\partial_{x3}\sigma_{33}\right]_t = -\rho\left[\left[\partial_t u\right]_h\right] \ ; \text{ and} \tag{3.1.3b}$$

3) energy conservation,

$$\left[\left[\partial_t E\right]_h\right] = \left[-\frac{\sigma_{33}}{\rho}\right]\left[-\frac{1}{\rho}\right]\left[\left[\partial_t \rho\right]_h\right] \ ; \tag{3.1.3c}$$

where $\left[\partial_h\right]_t \equiv \left[\frac{\partial}{\partial h}\right]_t$. The conservation requirements are simplier in the Langrangian picture.

By definition, an idealized shock wave (see figure 1.2.1) has a stress σ_{33}, density ρ, energy E, and particle velocity u, which are constant (i.e., independent of both x and t) behind the shock front (moving with velocity U_S). The conservation relationship 3.1.1 simplify to:

1) mass conservation,

$$\rho_o U_S = \rho\left[U_S - u\right] \ ; \tag{3.1.4a}$$

2) momentum conservation,

$$\sigma_{33} - (\sigma_{33})_o = \rho_o U_S u \ ; \text{ and} \tag{3.1.4b}$$

3) energy conservation,

$$E - E_o = \frac{1}{2}\left[\sigma_{33} + (\sigma_{33})_o\right]\left[\frac{1}{\rho_o} - \frac{1}{\rho}\right] \ . \tag{3.1.4c}$$

These are often called the jump conditions or Hugoniot equations, which relate the

stressed region to the unstressed region.

In addition to the three conservation equations, another relationship (often called the specifying equation, stress-strain equation, constitutive equation, or equation of state depending on the form of the equation) is needed to completely determine the system. For example, given an equation of state

$$f(\sigma_{33}, \rho, E) = 0 \quad , \tag{3.1.5}$$

equations 3.1.4, an initial state ($(\sigma_{33})_o$, ρ_o, E_o), and a measured shock velocity U_S, the shocked region parameters (σ_{33}, ρ, E, u) are uniquely determined since there are four independent equations for the four unknowns. Therefore, a test of whether equation 3.1.5 is the correct equation of state for this system, is the comparison of the calculated parameters (using equations 3.1.4 and 3.1.5) with the measured parameters (e.g., σ_{33} and u).

One of the ways that stress can be measured is to observe the PL.[58] In this thesis, this use of the PL as a stress monitor is extended. By making use of the fact that a nonhydrostatic stress causes degenerate energy band edges to split, the transverse stress (σ_{22}) as well as the longitudinal stress (σ_{33}) can be simultaneously determined by the observed PL. Using this technique, the equilibration of the longitudinal and transverse stress components of the shock wave can be observed (and is described in section 4.4). In addition to measuring the stress components of the shock wave, an analysis of the change in the PL line shape can reveal phenomena related directly to the shock propagation.

Some of the effects that have already been observed in shock compression of semiconductors are changes in the conductivity,[59-61] induced polarization,[60,62,63] change of the Hall coefficient,[64] phase transitions,[65-67] and shifts of the PL.[58] In this thesis, interesting new shock phenomena can be seen, such as the motion of the lattice under shock compression (described in section 4.2).

Shock waves can be generated in many ways. The most common way is to use explosives.[68] The explosives are used to generate the shock wave in the sample directly or to accelerate a projectile (a flat flyer plate) which impacts onto a sample (or into a sample mounted on a target plate). Shock pressures of up to $4Gbar$ have been generated using nuclear explosions.[69] Shock pressures of up to $2Mbar$ have been generated using flyer plates driven by explosions.[68] There have also been modifications of this plate impact method by using either compressed gasses[70] or magnetic fields[71] to accelerate the plate. Shock pressures of up to $5Mbar$ ($100kbar$) have been generated using flyer plates driven by compressed gasses[70] (magnetic fields[71]). Shock waves can also be generated using ultrafast laser pulses.[72,73] Shock pressures of up to $50Mbar$ have been generated using laser pulses.[74-78] In this thesis, picosecond laser pulses (with modest intensities) will be used to generate shock waves with peak pressures of $< 20kbar$. The process of laser generated shock waves is described in the next section.

3.2 Laser Generated Shock Waves

The generation of a transient pressure wave in a sample using a laser pulse can be broken into three stages. In the first stage, there is deposition of energy into the sample from the laser pulse, but no plasma generation. In the second stage, there continues to be deposition of energy from the laser pulse, and plasma is being generated from the sample. There is, of course, lost of energy from the plasma into the surroundings in this second stage. The third stage is signaled by the end of the laser pulse with the plasma decaying via various energy losses.

In the first stage, as the front part of the laser pulse hits the sample, only a fraction of the energy is absorbed with the rest being reflected. With $E_L(t)$ defined as the amount of laser pulse energy which has pass through an area during a time interval t, the time of this first stage (τ_1) is defined by $E_L(\tau_1) \equiv f_1 \bar{E}_L$, where $\bar{E}_L$ is the total energy of the laser pulse. In this first stage, the laser energy reflected is $Q_R = R\, f_1 \bar{E}_L$, and the laser energy absorbed in a volume $V_A \equiv A/\alpha$ is $Q_A = (\,1 - R\,)\, f_1 \bar{E}_L$, where R is the reflectivity, α is the absorption coefficient, and A is the spot size of the laser.

In this first stage, the laser energy deposited into the sample volume V_A is

$$Q(z) = (\,1 - R\,)\, f_1 \bar{E}_L \left[\frac{\alpha}{A} \right] e^{-\alpha z} \quad . \tag{3.2.1}$$

The deposition of energy into the sample causes the temperature to increase. The temperature increase is given by $\Delta T(z) = \dfrac{Q(z)}{C}$, where C is the specific heat per

unit volume. This increase in temperature will cause a change in volume $\Delta V = V_o(3\beta)\Delta T$, where β is the linear expansion coefficient. The pressure exerted by this change in volume is $\Delta P = B\frac{\Delta V}{V_o}$, where B is the bulk modulus. Therefore, the stress due to heating[79] is

$$\sigma_{ij} = -B(3\beta)\frac{Q(z)}{C}\delta_{ij} \quad . \tag{3.2.2}$$

To get an idea of the magnitude of the stress due to heating, consider for example the situation where $f_I\bar{E}_L = 10\mu J$, $A = 2\times10^{-3}cm^2$, and $\tau_I = 100fs$, and for an Aluminum sample, the relevant constants (from the 1963 AIP Handbook) are $B = 758kbar$, $\beta = 3\times10^{-5}K^{-1}$, $R = 0.9$, $\alpha = 10^6cm^{-1}$, and $C = 2J\,cm^{-3}K^{-1}$. Using these values in equation 3.2.2 yields a thermal stress of ~$0.4kbar$.

There is also an impulsive pressure due to the momentum of the photons either reflected or absorbed. The impulsive pressure P_I is related to the change in momentum Δp per unit time Δt. In the first stage, the change in momentum is $\Delta p = 2\frac{Q_R}{c} + \frac{Q_A}{c}$, where c is the speed of light. Therefore,

$$P_I \approx \frac{1}{A}\frac{\Delta p}{\Delta t} \approx \frac{(1+R)f_I\bar{E}_L}{A\tau_I c} \quad . \tag{3.2.3}$$

To get an idea of the magnitude of the impulsive pressure consider for example the situation where $f_I\bar{E}_L = 10\mu J$, $A = 2\times10^{-3}cm^2$, $\tau_I = 100fs$, and $c = 3\times10^{-5}cm\,fs^{-1}$, and a sample with $R = 0.9$. Using these values in equation 3.2.3 yields a pressure of $P_I \approx 0.03kbar$.

The transition from the first to the second stage is a gradual one. Taking the start of the second stage as when enough energy is deposited by the laser for some of the sample surface to vaporize (i.e., ablation). The generated plasma heats and also exerts pressure on the sample. This plasma reaches a constant density[80] because as the plasma density exceeds ρ_o most of the photons are absorbed by the plasma causing the density to decrease; conversely, if the density is less then ρ_o, the photons are absorbed by the sample surface and via ablation, the plasma density increases.

This expansion of a constant density plasma is no longer true, if the plasma is confined between the sample surface and a overlay which is transparent to the laser pulse. When the expansion of the plasma is limited by the overlay, the plasma density increases (via ablation of the sample surface) until the plasma is dense enough to absorb all the photons. Then, all of the photons go into heating the plasma.

Finally, the end of the laser pulse signals the start of the third stage. In this stage, there is a net loss of energy and mass from the plasma. The plasma starts to dissipate. How long the plasma lasts depends on the rate of loss of energy and mass to the surroundings. Note that for the situation where there is a transparent overlay, the energy losses due to plasma expansion and mass blow off are virtually eliminated. In both cases, there is loss of energy via transfer of thermal energy to the surrounding, emission of radiation (from the IR to x-ray),[81] and deposition from the plasma onto the sample (and if present, the transparent overlay).

For the last two stages, the pressure being transmitted into the sample is mainly due to the pressure of the plasma on the sample.[81] There is also some contribution to the pressure from the heating of the sample by the plasma. To get an idea of the magnitude of the pressure exerted by the plasma, consider a very simple model. By modeling the plasma as an ideal monatomic gas, it is easy to obtain a value for the magnitude of the pressure. The pressure of an ideal gas is $P = \frac{1}{V}nRT$. The temperature of an ideal monatomic gas is related to the internal energy by $U = \frac{3}{2}nRT$. Assuming that $U = Q_E(1 - f_I)\bar{E}_L$ (where Q_E is the net efficiency of the coupling of the laser energy into the plasma), the pressure of the plasma is $P = \frac{2Q_E}{3V}(1 - f_I)\bar{E}_L \equiv \frac{2Q_E}{3L_P}\left[\frac{(1 - f_I)\bar{E}_L}{A}\right]$, where the volume of the plasma is $V \equiv L_P A$. For the situation where $(1 - f_I)\bar{E}_L = 25mJ$, $A = 2\times10^{-3}cm^2$, $\tau_I = 100fs$, and with $Q_E = 0.1$ and $L_P = 10\mu m$, the pressure exerted by the plasma is ~$8kbar$. This extremely simple model for the plasma should not be taken seriously since the interaction of the laser pulse with the plasma as well as the decay of the plasma is very complex. The pressure exerted by the plasma decreases as the plasma starts to dissipate.

The above describes the formation of a transient pressure wave. The pressure generated in the first stage is generally negligible compared to the last two stages. Generally, for picosecond and nanosecond laser pulses, the generation of the plasma in stage 2 is extremely rapid, so that the moving boundary known as a shock front

is generated and the transient pressure wave is known as a shock wave. Even if the plasma generation is slow, eventually a shock front will form as the pressure wave travels[82] (provided the energy propagation losses are not too great). The experimental implementation of shock wave generation using picosecond laser pulses is described in the next section.

3.3 Experimental Method for Laser Generated Shock Compression

To generate the shock wave, a mode-locked picosecond Nd^{+3}:*YAG* laser (Continuum) is used (see figure 3.3.1). The laser oscillator (OSC) is composed of a (21*mm* diameter by 5*mm* thick) concave dielectric mirror with a 79*cm* radius of curvature, a 93*mm* long (7*mm* diameter) 0.9% Nd^{+3}:*YAG* laser rod (with hard dielectric AR coatings on the Brewster cut faces), and an etalon. The laser rod is pumped by 2 linear (2*atm* Krypton) flashlamps. This laser is mode-locked and Q-switched by 1*mm* of mode-locking dye #9740 (Eastman Kodak) in 1,2 dichloroethane (Eastman Kodak) which is in optical contact with the concave mirror. The mode-locking is actively assisted by an acousto-optic crystal (IntraAction) in this oscillator cavity.

From this oscillator cavity (OSC), a train of ~10 pulses is beam expanded by a telescope. Out of this train of pulses, one pulse is selected by a pulse slicer (see PS in figure 3.3.1). The pulse slicer is composed of a dielectric polarizer, a double-crystal Pockels cell (Lasermetrics), and a Glan-Taylor polarizer. The P polarized pulse train (see figure 3.3.2) is deviated by the Glan-Taylor polarizer onto a fast photodiode which triggers an avalanche chain of NPN transistors. The output from the avalanche transistors is applied to the double-crystal Pockels cell ($V_{\lambda/2} = 3.6kV$) causing one of the pulses in the train to become S polarized. This S polarized laser pulse then passes through the Glan-Taylor polarizer undeviated.

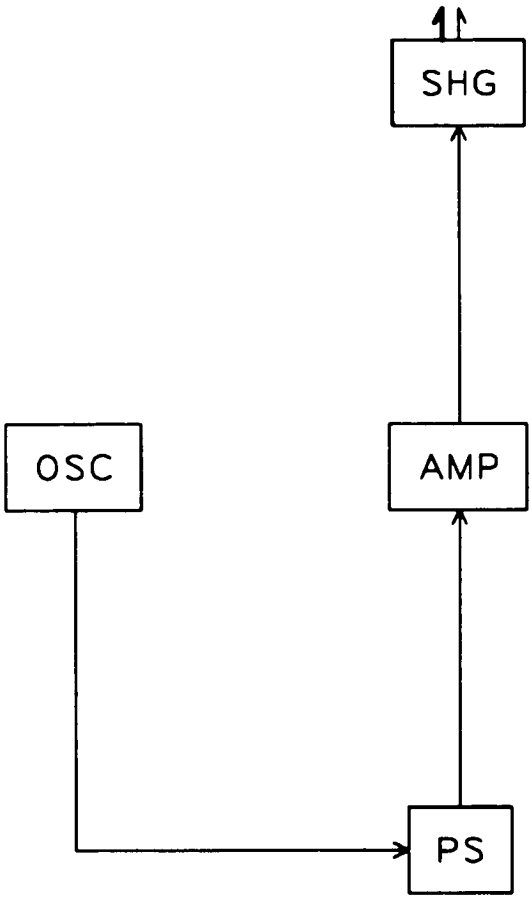

Figure 3.3.1. Block diagram of the picosecond mode-locked laser, where OSC is the laser oscillator, PS is the pulse slicer, AMP is the laser amplifier, and SHG is the second harmonic generator.

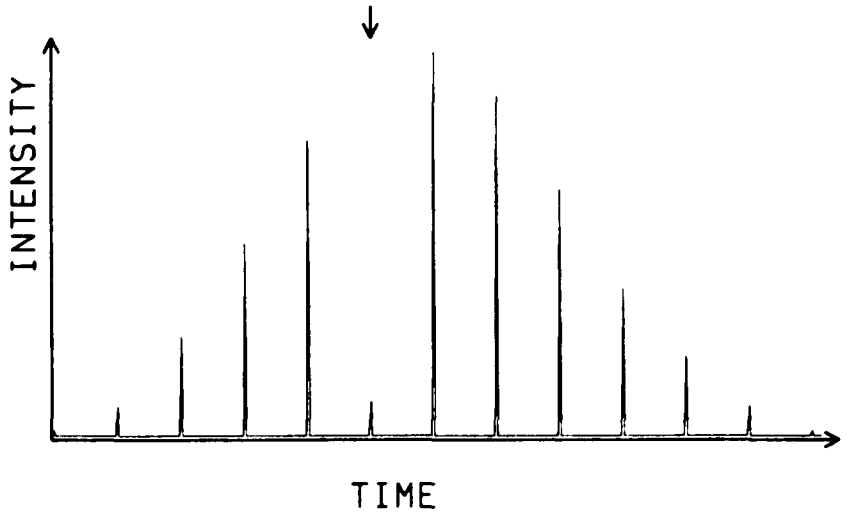

Figure 3.3.2. Picture of a pulse train which is deviated by the Glan-Taylor polarizer in the pulse slicer (PS). The arrow shows the position of the pulse which is undeviated by the Glan-Taylor polarizer.

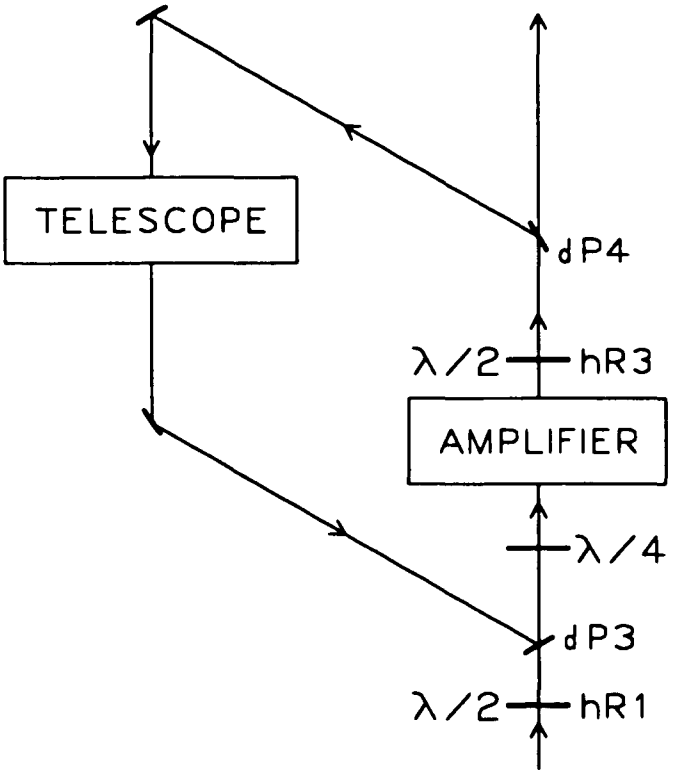

Figure 3.3.3. Schematic diagram of laser amplifier (AMP in figure 3.3.1) where dP3 & dP4 are dielectric polarizers and hR1 & hR3 are $\lambda/2$ plates.

The pulse which is selected by the double-crystal Pockels cell is then amplified in a double pass amplifier (AMP in figure 3.3.1). The amplifier geometry is displayed in figure 3.3.3. The incident pulse is P polarized by an $\lambda/2$ plate (hR1) which allows it to pass a dielectric polarizer (dP3). The pulse is then amplify by a 115*mm* long (9.52*mm* diameter) 0.9% Nd^{+3}:*YAG* laser rod (with hard dielectric AR coatings on the 2^o cut faces) which is pump by 4 linear 2*atm* Krypton flashlamps. A $\lambda/4$ plate is used to compensate for the birefringence[83] of the amplifier rod. The pulse is then S polarized by an $\lambda/2$ plate (hR3) which allows it to reflect off a dielectric polarizer (dP4). After beam expansion by a telescope, dielectric mirrors bring the pulse back to the dP3 polarizer for a second pass through the amplifier rod. The double amplified pulse is then P polarized by the hR3 $\lambda/2$ plate, which allows it to pass through the dP4 polarizer. The output from the amplifier (AMP) is sent into a second harmonic generator (SHG). In the SHG, a portion of the 30*ps* 1.06μm amplified laser (pump) pulse is converted by a (98% D) *KD*P* type I crystal (Inrad) to the second harmonic (532*nm* 27*ps*) for use as the probe pulse.

The (~35*mJ*) 30*ps* 1.06μm laser pump pulse is separated from the (~3μJ) 27*ps* 532*nm* laser probe pulse by a harmonic beam splitter (BS in figure 3.3.4). The pump pulse is then focused to a ~500μm spot size by a 15*cm* focal length plano-convex lens (FL1) onto a 20μm thick aluminum foil to generate the shock wave (see figure 3.3.5). The shock-wave in the aluminum foil can then propagate into the semiconductor sample (which is in mechanical contact with the foil). The semiconductor sample and the aluminum foil are supported by two quartz discs (see

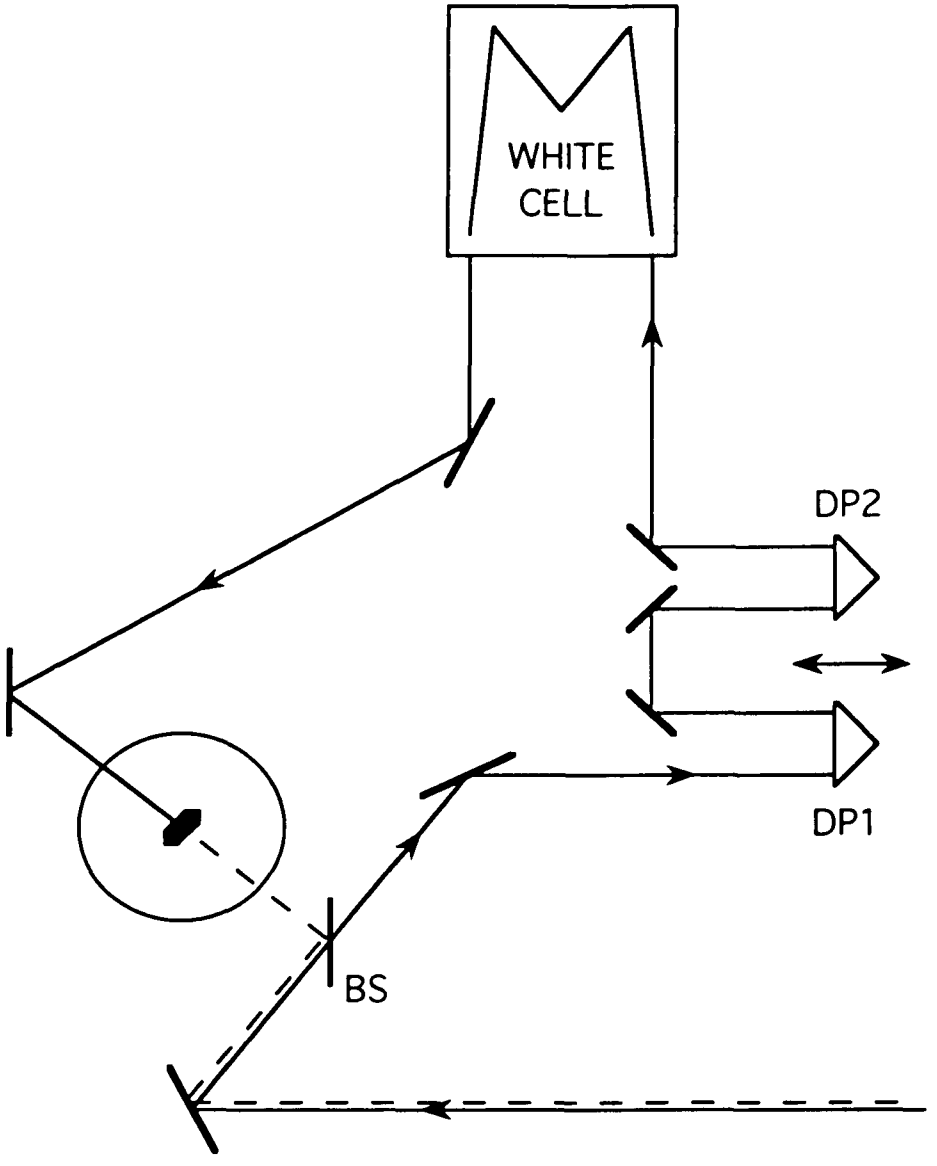

Figure 3.3.4. Schematic diagram of the shock compression experimental set up (see text).

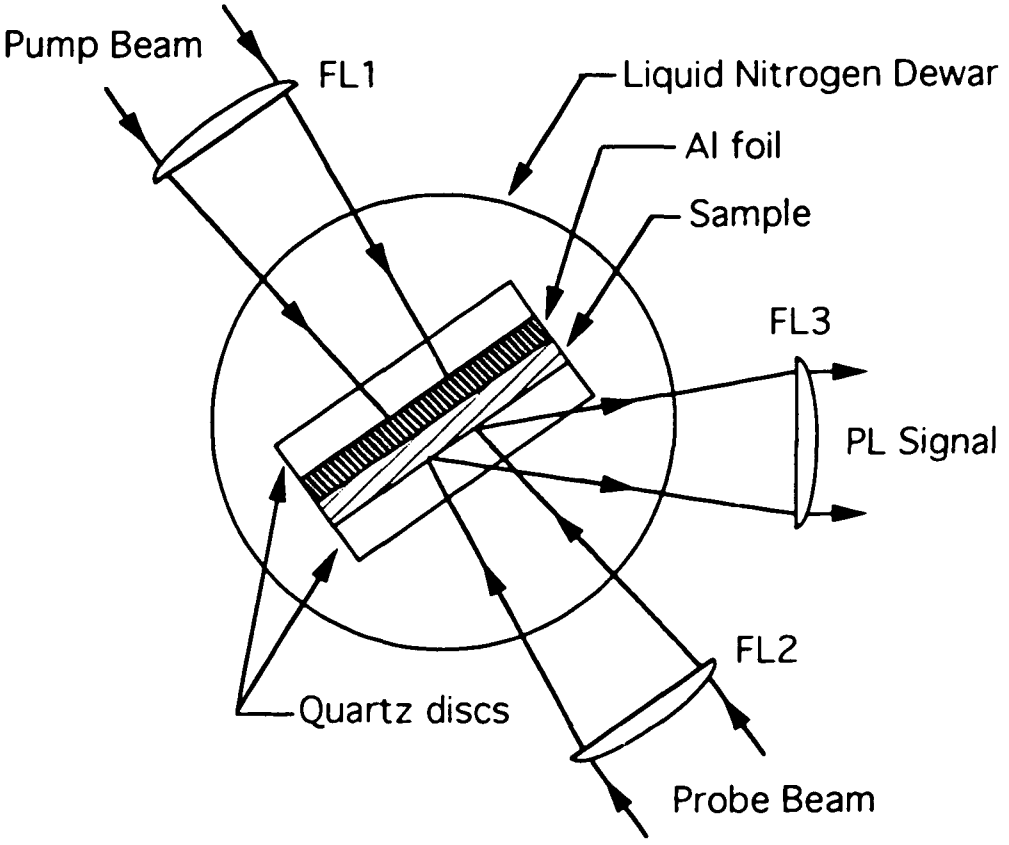

Figure 3.3.5. Schematic diagram of the shock compression sample geometry (see text). FL1, FL2, and FL3 are 15*cm* focal length plano-convex lenses.

figure 3.3.5) in a copper sample holder. For low temperature measurements, the sample holder together with the semiconductor sample, aluminum foil, and quartz discs are suspended in a liquid nitrogen optical dewar (see figure 3.3.5).

In order to study the effects of shock wave on the semiconductor, a probe pulse is needed to photoexcite the semiconductor to its non-equilibrium state. The probe pulse which is separated from the pump pulse by a harmonic beam splitter (see BS in figure 3.3.4) can be delayed relative to the pump pulse by prisms (DP1 & DP2) and a white cell. This delay between the pump and probe allows the study of different slices of the shock profile from changes in the photoluminescence emitted from the semiconductor.

The PL from the electron-hole plasma (EHP) generated by the probe pulse is dispersed by a 275*mm* crossed Czerny-Turner spectrograph with a 300 *grooves/mm* grating (Jarrell-Ash) and detected by a multi-alkali photocathode coupled to a photodiode array via a microchannel plate (Princeton Applied Research). The cooled photodiode array ($T = -15^{o}C$) is control by an optical multichannel analyzer (Princeton Applied Research) which is interfaced to a PDP11/23+ minicomputer (Digital Equipment).[84] For data analysis, the collected data are transferred from the PDP11/23+ minicomputer to a VAX11/780 computer (Digital Equipment).

IV. Semiconductors Under Stress

4.1 Introduction

In this chapter, the results of PL experiments of GaSe, CdSe, and GaAs under stress are presented. In section 4.2, the effects of shock compression of GaSe will be explained in the framework of an exciton exciton scattering theory. In section 4.3, the shock profile in CdSe is obtained from the shifts in the transition energies under stress. This experiment also suggests the possibility of monitoring both the longitudinal and transverse stress components of the shock wave in GaAs. In section 4.4, the determination of the time evolution of the transverse and longitudinal stress components of the shock wave in GaAs is presented. In section 4.5, the hole dynamics in GaAs under static uniaxial compression which have been studied via time resolved PL is presented. In section 4.6, the determination of the transverse and longitudinal stress components of the shock wave in a GaAs quantum well is presented.

4.2 Gallium Selenide

The first sample that is studied under shock compression is Gallium Selenide (GaSe).[85,86] The main effect of the shock compression on GaSe is to change the band gap energy. The decrease of the band gap energy causes characteristic changes in the PL spectra within the framework of the exciton exciton scattering model. These changes in the PL spectra as well as a shock induced line broadening effect will be described in section 4.2B. The background information needed to explain the changes in the PL under shock compression is described in the next section.

4.2A Unstressed GaSe

GaSe is a III-VI semiconductor which crystalizes in a layered structure. Each layer is composed of double planes of Gallium atoms sandwiched by single planes of Selenium atoms.[87] Single crystals of GaSe can have layers stacked with period three (γ polytype) and with period two (β and ε polytypes). The ε polytype has D_{3h} hexagonal symmetry.[88]

For the PL experiment, a 50μm ε-GaSe single crystal is coupled to a 20μm aluminum foil with mineral oil, which is then sandwiched between two 6.35mm thick Pyrex discs. The aluminum foil is necessary only for the shock experiment and does not affect the PL spectra. The c axis of the crystal is perpendicular to the front surface. The probe pulse which is collinear with the c axis is focused to a

350μm diameter spot on the front surface of the sample. PL data are recorded with the sample at room temperature. A representative spectra of the spontaneous PL from GaSe for a probe energy of $400nJ$ is shown in figure 4.2.1. It can be seen that the spontaneous PL has a symmetric line shape (with a FWHM of ~$112meV$) which peaks at ~$1965meV$.

Two possible models for the PL spectra are the electron hole plasma (EHP) model and the exciton exciton scattering model. The line shape due to the EHP model has been given by Yoshikuni *et. al.*[89] as

$$I_{sp}(h\nu) = I_{sp}^{o}(h\nu - \tilde{E}_g)^{1/2} e^{-\beta_c (h\nu - \tilde{E}_g)} \quad , \tag{4.2.1}$$

where I_{sp}^{o} is a constant, $\tilde{E}_g \equiv E_p - \frac{1}{2\beta_c}$ is the reduced band gap energy, E_p is the peak energy of the emission band, $\beta_c \equiv \left[k_b T_c \right]^{-1}$, and T_c is the carrier temperature. The EHP line shapes (equation 4.2.1) for $E_p = 1973meV$ and $T_c = 300K$, $400K$, $500K$, and $600K$ are shown in figure 4.2.2, together with the experimental line shape (from the unshocked GaSe spontaneous emission PL shown in figure 4.2.4).

For the exciton exciton scattering model, the line shape has been calculated by Moriya and Kushida[90] using second order perturbation theory. For the process of two excitons scattering into an electron hole pair with the emission of a photon (expressed symbolically as $[E_K^{1/2}, E_K^{1/2}] \rightarrow [h\nu, e\text{-}h]$), the initial energy of this process is

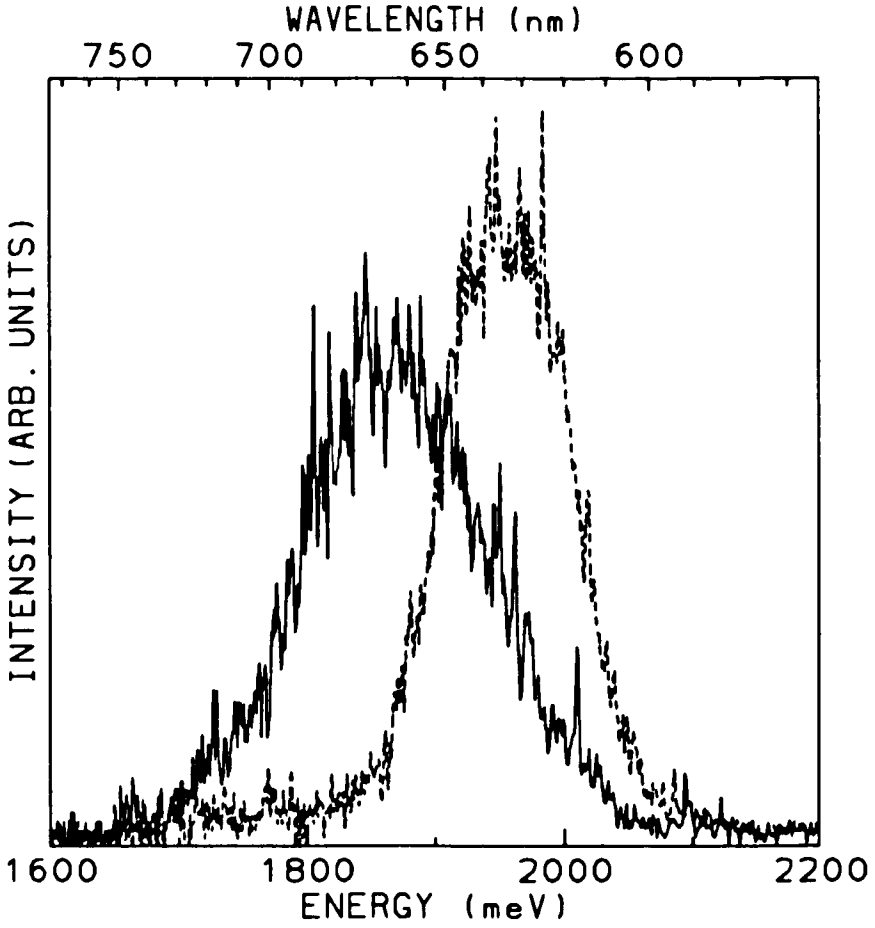

Figure 4.2.1. A plot of the unshocked (---) and shocked (—) spontaneous emission spectra from GaSe at low probe intensity ($400nJ$).

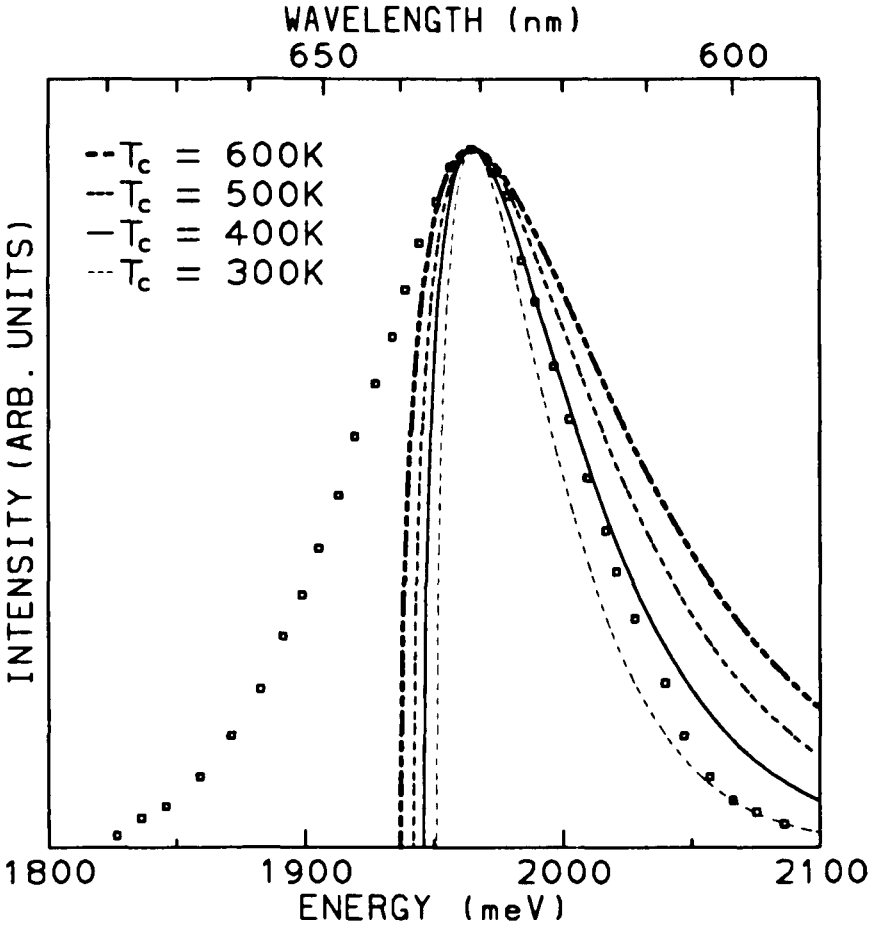

Figure 4.2.2. A plot of the spontaneous emission from GaSe together with the line shapes due to the EHP model (equation 4.2.1) for various temperatures T_c (see text).

$$E_i \equiv \left[E_x + \frac{\hbar^2 K^2}{2m_x} \right] + \left[E_x + \frac{\hbar^2 K'^2}{2m_x} \right] , \qquad (4.2.2a)$$

and the final energy is

$$E_f \equiv h\nu + \left[E_x + E_b + \frac{\hbar^2 k_e^2}{2m_e} \right] + \frac{\hbar^2 k_h^2}{2m_h} , \qquad (4.2.2b)$$

where $E_x \equiv E_g - E_b$, E_g is the bandgap energy, E_b is the binding energy of exciton, and K, k_e, and k_h ($m_x \equiv m_e + m_h$, m_e, and m_h) are the wave vector (effective mass) of the exciton, electron, and hole, respectively. The line shape for the $[E_K^{j'}, E_K^{j'}] \rightarrow [h\nu, e\text{-}h]$ process is[90]

$$I_{sp}(h\nu) = \frac{I_{sp}^{eo}\, \rho(h\nu)\beta_x h\nu}{(h\nu - E_x)^2 + (\pi\alpha/\varepsilon)E_x^2} I_{xx} , \qquad (4.2.3a)$$

where

$$I_{xx} \equiv \int_0^\infty d\xi \int_0^\infty dt \frac{\sqrt{\xi}}{(1 + \xi/E_b)^4}\, e^{-t\, -\beta_x^2 (E_x - E_b - h\nu - \xi)^2/4t} , \qquad (4.2.3b)$$

I_{sp}^{eo} is a constant, $\rho(h\nu)$ is the density of photon modes, ε is the dielectric constant, $\beta_x \equiv \left[k_b T_x \right]^{-1}$, and T_x and α are the temperature and the polarizability of exciton, respectively. Equation 4.2.3a has a Lorentzian form ($[(\omega - \omega_o)^2 + \gamma^2\omega_o^2]^{-1}$) multiplied by several factors, and is therefore expected to give a distorted Lorentzian line shape. Note that as γ increases, the width of the line shape increases. The dimensionless parameter $\gamma = \pi\alpha/\varepsilon$ describes the coupling between the photons and the excitons.

The theoretical line shape calculated using equation 4.2.3 (with the exciton-

photon coupling coefficient $\pi\alpha/\varepsilon = 3.3\times10^{-3}$, $T_x = 500K$, $E_b = 20meV$, and $E_x = 2.0eV$) is shown in figure 4.2.3 together with the experimental line shape (from the unshocked GaSe spontaneous emission PL shown in figure 4.2.4).

From a comparison[91] of figures 4.2.2 and figure 4.2.3, it is clear that the spontaneous emission comes from exciton exciton scattering into an electron hole pair with emission of a photon.

Stimulated emission is observed by increasing the probe energy beyond the threshold energy of $5\times10^{7}W/cm^{2}$. A representative spectra of the stimulated PL is shown in figure 4.2.4 (for a probe energy of $3\mu J$). The stimulated PL emission line peaks at ~$1890meV$ (with a FWHM of ~$20meV$). In this figure, the spontaneous PL emission is also observable at ~$1965meV$ (with a FWHM of ~$100meV$).

The stimulated emission line shape for unsaturated gain is given by

$$I_{st}(h\nu) = I_{st}^{eo} e^{(g(h\nu)\,l)} \quad . \tag{4.2.4}$$

The spectral gain due to the $[E_K^{1}, E_K^{1}] \rightarrow [h\nu, e-h]$ process has been given by Moriya and Kushida[92] as

$$g(h\nu) = I_g^{eo}\, I_{sp}(h\nu)\left[\, 1-\eta e^{\beta_x[h\nu-(E_g-2E_b)]}\right] \quad , \tag{4.2.5}$$

where

$$\eta = \left[\frac{n_e n_h}{n_x}\right]\left[\frac{m_x^2}{m_e m_h}\right]^{3/2} \quad , \tag{4.2.6}$$

I_g^{eo} is a constant, and n_x, n_e, and n_h are the density of the exciton, electron, and

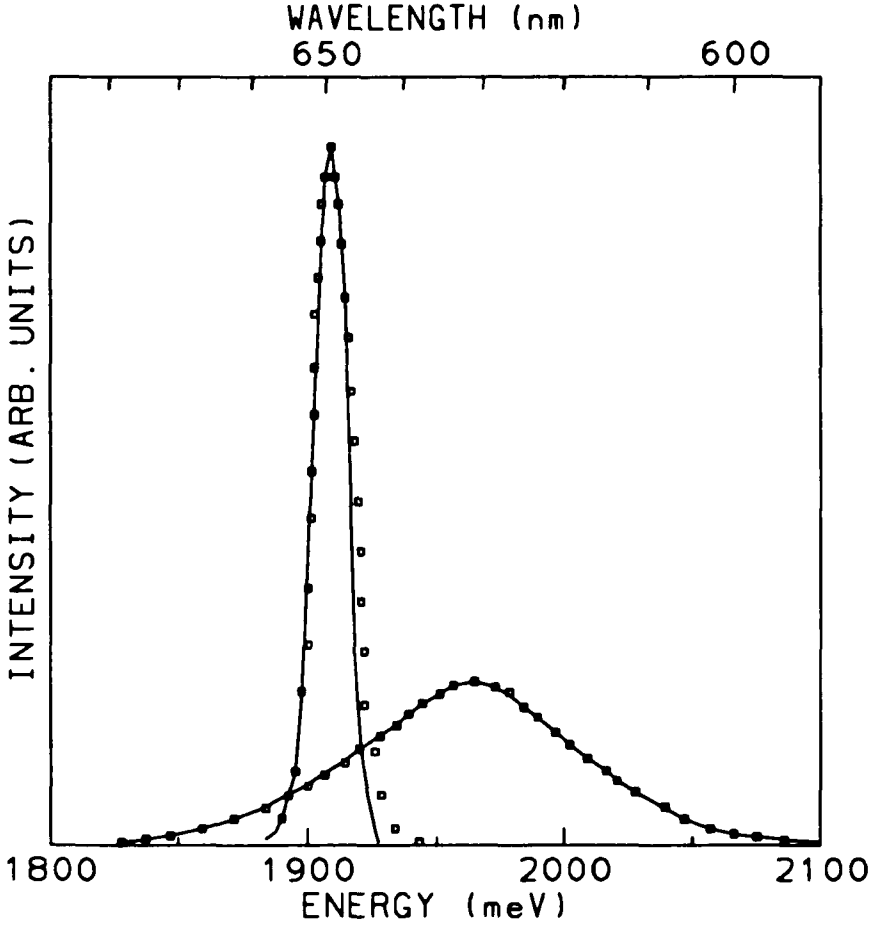

Figure 4.2.3. A plot of the spontaneous and stimulated emission from GaSe together with the fit using equations 4.2.3 and 4.2.4 (see text).

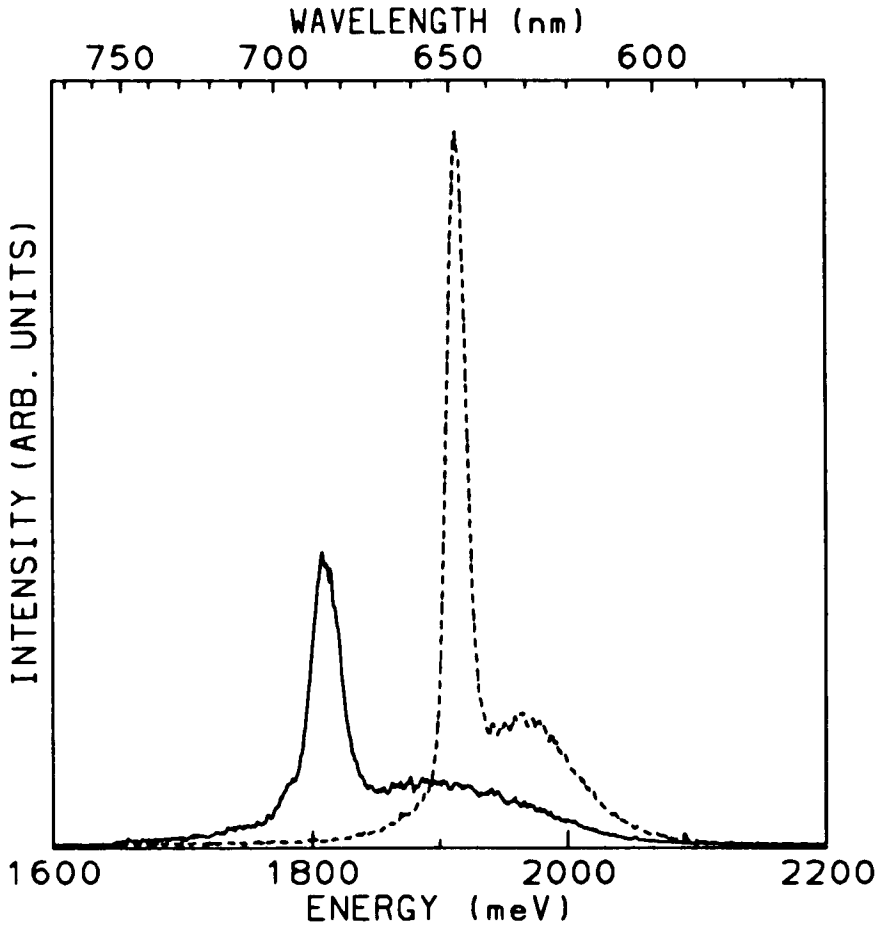

Figure 4.2.4. A plot of the unshocked (---) and shocked (—) stimulated emission spectra from GaSe at high probe intensity ($3\mu J$).

hole, respectively. The theoretical line shape calculated using equations 4.2.4 and 4.2.5 (with the exciton-photon coupling coefficient $\pi\alpha/\varepsilon = 3.3\times10^{-3}$, $T_x = 500K$, $E_b = 20meV$, $E_x = 2.0eV$) and $\eta = 2.0$ is shown in figure 4.2.3 together with the experimental line shape (from the unshocked GaSe stimulated emission PL shown in figure 4.2.4).

4.2B Shock Compressed GaSe

In this section, the changes of the GaSe PL under shock compression are described on the basis of the exciton exciton scattering model. For the shock compression experiment, a $35mJ$ pump pulse which is collinear and counter-propagating relative to the probe pulse is focused to a $450\mu m$ diameter spot on the aluminum foil in order to generate the shock wave. Data are recorded with the sample at room temperature. A representative spectra of the PL from the unshocked and shock GaSe for two different probe energies is shown in figures 4.2.1 and 4.2.4 ($400nJ$ and $3\mu J$, respectively). In figure 4.2.1, the spontaneous PL emission from the unshocked GaSe peaks at ~$1965meV$ (with a FWHM of ~$110meV$). Under shock compression, the spontaneous PL emission from GaSe red shifts to ~$1880meV$ (with a broaden FWHM of ~$170meV$). In figure 4.2.4 the spontaneous PL emission from the unshocked GaSe peaks at ~$1965meV$ (with a FWHM of ~$100meV$). Due to the higher probe energy, there is also stimulated PL emission from the unshocked GaSe at ~$1910meV$ (with a FWHM of ~$20meV$). Under shock compression, the spontaneous PL emission from GaSe red shifts to ~$1890meV$ (with a broaden FWHM of ~$190meV$). The stimulated PL emission from GaSe also red shifts (to ~$1810meV$) and broadens (with a FWHM of ~$30meV$).

In figure 4.2.1, a spectral red shift of ~$28nm$ (~$85meV$) of the spontaneous emission line from GaSe can be observed under shock compression. To obtain the

pressure dependence of the PL peak, consider the peak energy E_p from equation 4.2.2. Implicit in this equation is the conservation of energy, $E_f = E_i$. By neglecting the contributions due to changes in kinetic energy, this becomes

$$E_p \approx E_x - E_b = E_g - 2E_b \quad . \tag{4.2.7}$$

From the reported pressure dependence of the energy gap,[93]

$$\frac{\partial E_g}{\partial \sigma_{33}} = -6.2 meV/kbar \quad , \tag{4.2.8}$$

and exciton binding energy,

$$\frac{\partial E_b}{\partial \sigma_{33}} = -0.6 meV/kbar \quad , \tag{4.2.9}$$

equation 4.2.7 yields

$$\frac{\partial E_p}{\partial \sigma_{33}} = -5.0 meV/kbar \quad . \tag{4.2.10}$$

A $\sim 85 meV$ red shift corresponds to a shock pressure of $17 kbar$. This agrees with shock pressure measurements using an x-cut quartz transducer.

Another significant feature of the spontaneous emission line from GaSe under shock compression is the broadening of the spectral line width (see figure 4.2.1). One possible line width broadening mechanism is pressure inhomogeneity. However, the shock pressure (~20% transverse and $\sim 0.5 kbar$ longitudinal) inhomogeneity is not enough to explain the observed broadening. Another possible line width broadening mechanism is the change in the temperature of the excitons under

shock compression. This temperature change implies a change in the distribution of the excitons as a function of momentum ($|\mathbf{K}|$). Because of the Doppler effect, the frequency of the emitted radiation from the excitons is slightly different for excitons with different momentums. The Doppler line width has been calculated by Yariv[94] and is given by

$$\delta_D \lambda = \frac{2\lambda_p}{c} \left[\frac{2 ln 2}{\beta_x m_x} \right]^{1/2} . \tag{4.2.11}$$

From equation 4.2.11, the observed broadening would require the exciton temperature to increase to $1700K$ from $434K$. However, the observed shock compression data does not show any significant temperature increase.[95] Also, thermal broadening causes the line shape to be Gaussian in disagreement with the observed Lorentzian line shape.

A mechanism which can explain the significant line broadening is the shock wave induced collision broadening.[86] In this mechanism, the excitons suffer phase-perturbing collisions with the lattice molecules which are moving with particle velocity u behind the shock front. The collisional frequency for each exciton is

$$f_c \approx a_x^2 u n_{mol} , \tag{4.2.12}$$

where a_x is the Bohr radius of the exciton and n_{mol} is the molecular density. Using equation 3.1.4b, this becomes

$$f_c \approx a_x^2 \left[\frac{\sigma_{33}}{\rho_0 U_s} \right] n_{mol} . \tag{4.2.13}$$

The line broadening is then

$$\Delta\lambda = \frac{\lambda_o^2}{c}\Delta\nu = \frac{\lambda_o^2}{c}\,\frac{2f_c}{\pi} = \frac{\lambda_o^2}{c}\left[\frac{2a_x^2 n_{mol}}{\pi\rho_0 U_s}\right]\sigma_{33} \quad . \tag{4.2.14}$$

Using[96] $a_x = 3.1nm$ and $n_{mol} = 2\times10^{22}cm^{-3}$,

$$\Delta\lambda \approx [1.3nm/kbar]\sigma_{33} \quad . \tag{4.2.15}$$

For $\sigma_{33} = 17kbar$, $\Delta\lambda = 22nm$ in agreement with the experimental data (see figure 4.2.5).

For the stimulated emission line (see figure 4.2.4), a red shift and broadening is also observed. However, the red shift (~$36nm$ or ~$100meV$) of the stimulated emission line is larger than the spontaneous emission shift (~$24nm$ or ~$70meV$). There is also an observed intensity decrease. The broadening of the stimulated emission is a direct consequence of the broadening of the spontaneous emission (equation 4.2.5). The larger red shift as well as the intensity decrease can be explained by the reduction of the (exciton exciton scattering) gain due to the shock wave induced band gap shrinkage. An increase in the effective value of η causes both an decrease in intensity and a larger red shift. From equation 4.2.5, the pressure dependence of η is

$$\eta_S = \eta\left[e^{-\beta_x\left[\frac{\partial E_g}{\partial P} - 2\frac{\partial E_b}{\partial P}\right]}\right] \quad . \tag{4.2.16}$$

The observed decrease in intensity is given by

$$\frac{I_{st}^S}{I_{st}} = e^{(g_S - g)l} \quad . \tag{4.2.0}$$

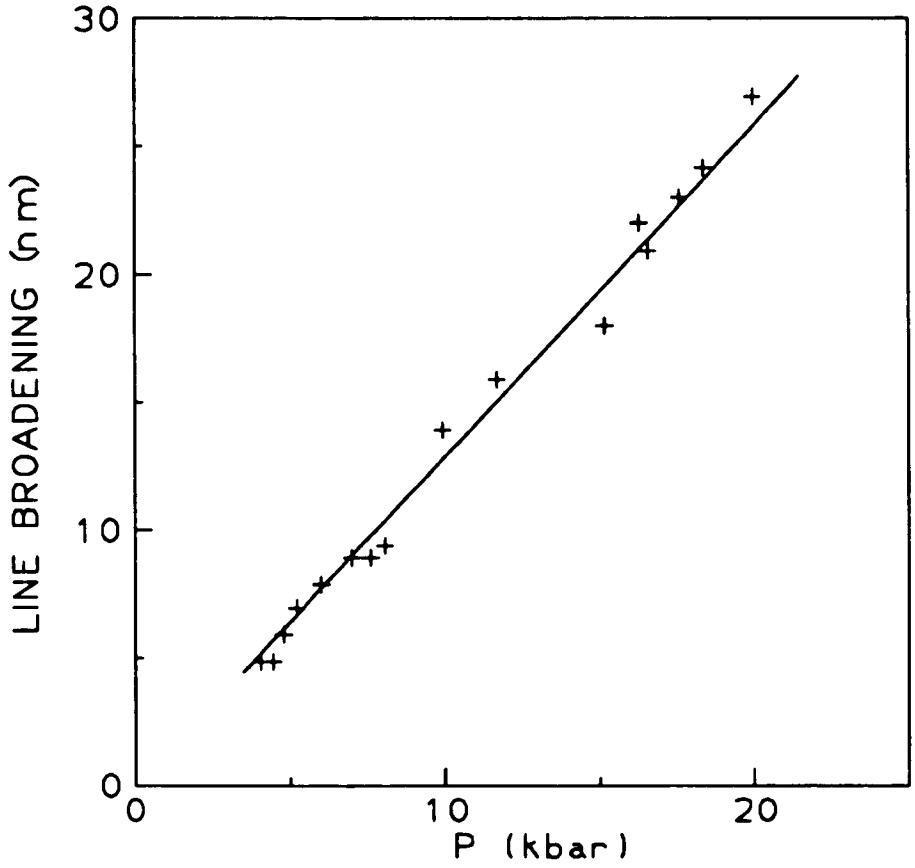

Figure 4.2.5. A plot of the observed broadening together with equation 4.2.15.

From $\sigma_{33} = 17kbar$, $\eta = 2$, and equation 4.2.5, $\frac{g_S}{g} - 1 \approx -0.86$. Using[96] $gl \sim 1$, yields $\frac{I_{st}^S}{I_{st}} \sim 0.4$ in agreement with the experimental data (see figure 4.2.4).

In summary, the spontaneous and stimulated PL from GaSe are due to an exciton exciton scattering mechanism. One of the effects of the shock compression is to change the band gap, which causes characteristic changes in the PL spectra within the framework of the exciton exciton scattering model. The shock induced line broadening is related uniquely to the transient nature of shock compression.

4.3 Cadmium Selenide

The second shock compression experiment is on Cadmium Selenide (CdSe).[97] In this experiment, the conditions needed for the determination of the stress components parallel (longitudinal component) and perpendicular (transverse components) to the direction of shock propagation will be specified.

In the next section, the unstressed band structure of CdSe will be described. Then, the usual strain Hamiltonian of CdSe is modified to describe shock compression. Finally, in section 4.3B, the results of the shock compression experiments on CdSe will be presented, and the conditions needed for the determination of the longitudinal and transverse stress components will be specified.

4.3A Theoretical Model

CdSe is a II-VI semiconductor which crystallizes in a wurtzite structure. The lowest conduction band has a s-type basis function and is characterized by Γ_7 symmetry at $k = 0$. The highest valence band has p-type basis functions. The usual six fold degeneracy at $k = 0$ is split into three spin degenerate valence subbands (denoted v_A, v_B, and v_C) by the crystal field and the spin orbit interactions (H_{so-cf}).

$$H_{so-cf} = \Delta_1 \left[\mathbf{L}\cdot\bar{\sigma} - \frac{1}{2} \right] + \Delta_2 \left[L_3^2 - 1 \right] + \Delta_{cs2} \left[L_3\cdot\bar{\sigma}_3 - \frac{1}{2} \right] , \qquad (4.3.1)$$

where $\mathbf{L}$ and $\bar{\sigma}$ are the orbital and spin angular momentum operators, respectively, $\Delta_1 \equiv \frac{2\Delta_{so}}{3} - \frac{\Delta_{cs2}}{3}$, $\Delta_2 \equiv \Delta_{cs1} + \frac{\Delta_{cs2}}{2}$, $\Delta_{so} = 439meV$, $\Delta_{cs1} = 81.5meV$, and

$\Delta_{cs2} = -25.4meV$ for CdSe[98] at $1.8K$.

The top most valence subband (v_A) which is characterized by Γ_9 symmetry[99] at $k = 0$, is separated from the conduction band by the band gap energy[98] $\bar{E}_g^w = 1.84eV$ at $1.8K$. The v_B and v_C valence subbands are both characterized by Γ_7 symmetry[99] at $k = 0$. The separation between v_A and v_B (v_B and v_C) is[98] $\Delta_{AB} = 25.5meV$ ($\Delta_{BC} = 432meV$) at $1.8K$.

From symmetry considerations,[100] the strain Hamiltonians for a semiconductor with wurtzite structure have been given by Pikus[101] as

$$H_c = -a_c^w \left(\varepsilon_{11} + \varepsilon_{22} + \varepsilon_{33} \right) \tag{4.3.2a}$$

and

$$\begin{aligned} H_{orb(\varepsilon)} = {} & a_1^w (\varepsilon_{11} + \varepsilon_{22}) + a_0^w \varepsilon_{33} \\ & + b_1^w (\varepsilon_{11} + \varepsilon_{22}) L_3^2 + b_0^w \varepsilon_{33} L_3^2 \\ & + c_1^w (\varepsilon_+ L_-^2 + \varepsilon_- L_+^2) \\ & + d_1^w \left[\varepsilon_{-c} \{ L_3, L_+ \} + \varepsilon_{+c} \{ L_3, L_- \} \right] , \end{aligned} \tag{4.3.2b}$$

where $L_\pm \equiv \frac{1}{\sqrt{2}} \left[L_1 \pm iL_2 \right]$, $\varepsilon_\pm \equiv \varepsilon_{11} - \varepsilon_{22} \pm 2i\varepsilon_{12}$, $\varepsilon_{\pm c} \equiv \varepsilon_{13} \pm i\varepsilon_{23}$, and ε_{ij} is the strain tensor. The deformation potentials for CdSe are[98] $a_c^w + a_0^w = 760.0meV$, $a_c^w + a_1^w = 3700.0meV$, $b_0^w = 4000.0meV$, $b_1^w = -2200.0meV$, $c_1^w = -1200.0meV$, and $d_1^w = -3000.0meV$.

To rewrite the strain Hamiltonians in terms of stress, the elastic compliance (**s**) relating the stress (**T**) to strain (**ε**) is needed. For hexagonal lattices, the elastic compliance is[102]

$$\mathbf{s} \equiv \begin{pmatrix} S_{11}^{w} & S_{12}^{w} & S_{13}^{w} & 0 & 0 & 0 \\ S_{12}^{w} & S_{11}^{w} & S_{13}^{w} & 0 & 0 & 0 \\ S_{13}^{w} & S_{13}^{w} & S_{33}^{w} & 0 & 0 & 0 \\ 0 & 0 & 0 & S_{44}^{w} & 0 & 0 \\ 0 & 0 & 0 & 0 & S_{44}^{w} & 0 \\ 0 & 0 & 0 & 0 & 0 & 2(S_{11}^{w} - S_{12}^{w}) \end{pmatrix} . \tag{4.3.3}$$

The constants for CdSe[103] are $S_{11}^{w} = 2.3\times10^{-3} kbar^{-1}$, $S_{12}^{w} = -1.1\times10^{-3} kbar^{-1}$, $S_{13}^{w} = -0.5\times10^{-5} kbar^{-1}$, $S_{33}^{w} = 1.7\times10^{-3} kbar^{-1}$, and $S_{44}^{w} = 7.6\times10^{-3} kbar^{-1}$.

To obtain the strain stress relationship, the stress vector is needed. Choosing a coordinate system where the x_3 axis is along the direction of propagation of the shock wave, the two stress components (σ_{11}, σ_{22}) which are transverse to the shock propagation direction are assumed equal and is denoted by P (i.e., $\sigma_{11} = \sigma_{22} \equiv -P$). The longitudinal stress component (which is along the direction of propagation of the shock wave) can be written as $\sigma_{33} \equiv -P - X$. Neglecting any shear terms (i.e., $\sigma_{23} \equiv \sigma_{31} \equiv \sigma_{12} \equiv 0$), the stress vector for shock compression along the x_3 axis is given by

$$\mathbf{T} \equiv \begin{pmatrix} -P \\ -P \\ -P - X \\ 0 \\ 0 \\ 0 \end{pmatrix} . \tag{4.3.4}$$

Note that for $X = 0kbar$, the longitudinal and transverse components are equal and equation 4.3.4 can be recognized as the stress vector for hydrostatic pressure (see equation 2.2.8). In this case, behind the shock front there exists only hydrostatic pressure. Conversely, for $P = 0kbar$, there is no transverse component and only the longitudinal component is nonzero, and equation 4.3.4 is identical to the stress vector for uniaxial stress along the x_3 axis (see equation 2.2.11).

Using equations 4.3.3, 2.2.7, and 4.3.4, the strain stress relationship for shock compression along the c axis (see appendix A1) becomes

$$\varepsilon_{11} = \varepsilon_{22} = -\left[S_{11}^{w} + S_{12}^{w} + S_{13}^{w}\right] P - S_{13}^{w} X \ , \tag{4.3.5a}$$

$$\varepsilon_{33} = -\left[2S_{13}^{w} + S_{33}^{w}\right] P - S_{33}^{w} X \ , \tag{4.3.5b}$$

and

$$2\varepsilon_{23} = 2\varepsilon_{31} = 2\varepsilon_{12} = 0 \ . \tag{4.3.5c}$$

From equations 4.3.1 and 4.3.2, the Hamiltonian matrix for shock compression along the c axis (see appendix A1) is

$$\mathbf{H}_\sigma \equiv \begin{array}{c} \begin{matrix} P_+\chi_\uparrow & P_-\chi_\uparrow & P_z\chi_\downarrow \end{matrix} \\ \begin{bmatrix} \Lambda_1^w & 0 & 0 \\ 0 & \Lambda_2^w & \Lambda_{23}^w \\ 0 & \Lambda_{23}^w & \Lambda_3^w \end{bmatrix} \end{array} , \tag{4.3.6}$$

where $P_\pm \equiv \frac{1}{\sqrt{2}}\left[P_x \pm iP_y \right]$, P_x, P_y, and P_z are the p-like basis functions, $\chi_\uparrow$ and $\chi_\downarrow$ are the spin basis functions,

$$\Lambda_1^w \equiv -\delta E_a^w - \delta E_b^w \ , \tag{4.3.7a}$$

$$\Lambda_2^w \equiv -\Delta_1 - \Delta_{cs2} - \delta E_a^w - \delta E_b^w \ , \tag{4.3.7b}$$

$$\Lambda_3^w \equiv -\Delta_2 - \frac{1}{2}\Delta_1 - \frac{1}{2}\Delta_{cs2} - \delta E_a^w \ , \tag{4.3.7c}$$

$$\Lambda_{23}^w \equiv -\frac{1}{\sqrt{2}}\Delta_1 \ , \tag{4.3.7d}$$

$$\delta E_a^w \equiv a_0^w \left[2S_{13}^w + S_{33}^w \right] P + 2a_1^w \left[S_{11}^w + S_{12}^w + S_{13}^w \right] P$$

$$+ \left[a_0^w S_{33}^w + 2a_1^w S_{13}^w \right] X \ ,$$

and

$$\delta E_b^w \equiv b_0^w \left[2S_{13}^w + S_{33}^w \right] P + 2b_1^w \left[S_{11}^w + S_{12}^w + S_{13}^w \right] P$$

$$+ \left[b_0^w S_{33}^w + 2b_1^w S_{13}^w \right] X \ . \tag{4.3.8}$$

The eigenvalues of the matrix 4.3.6 gives the transitional energies between the conduction band and the valence subbands (see appendix A1). They are

$$E_{c-vA}(P, X) \equiv \bar{E}_g^w + \Lambda_c^w - \lambda_{vA} = \bar{E}_g^w + \delta E_H^w + \delta E_b^w \quad , \tag{4.3.9a}$$

$$E_{c-vB}(P, X) \equiv \bar{E}_g^w + \Lambda_c^w - \lambda_{vB}$$

$$= \bar{E}_g^w + \frac{2\Delta_{cs1}}{3} + \Delta_{cs2} - \frac{2(\Delta_{cs1})^2}{9\Delta_{so}} + \delta E_H^w$$

$$+ \left[\frac{1}{3} + \frac{4\Delta_{cs1}}{9\Delta_{so}}\right]\delta E_b^w - \frac{2}{9\Delta_{so}}\left[\delta E_b^w\right]^2 + \ldots \quad , \tag{4.3.9b}$$

and

$$E_{c-vC}(P, X) \equiv \bar{E}_g^w + \Lambda_c^w - \lambda_{vC}$$

$$= \bar{E}_g^w + \Delta_{so} + \frac{\Delta_{cs1}}{3} + \frac{\Delta_{cs2}}{2} + \frac{2(\Delta_{cs1})^2}{9\Delta_{so}} + \delta E_H^w$$

$$+ \left[\frac{2}{3} - \frac{4\Delta_{cs1}}{9\Delta_{so}}\right]\delta E_b^w + \frac{2}{9\Delta_{so}}\left[\delta E_b^w\right]^2 + \ldots \quad , \tag{4.3.9c}$$

where

$$\delta E_H^w \equiv \left[\left[a_c^w + a_0^w\right]\left[2S_{13}^w + S_{33}^w\right] + 2\left[a_c^w + a_1^w\right]\left[S_{11}^w + S_{12}^w + S_{13}^w\right]\right]P$$

$$+ \left[\left[a_c^w + a_0^w\right]S_{33}^w + 2\left[a_c^w + a_1^w\right]S_{13}^w\right]X \quad . \tag{4.3.10}$$

From equation 4.3.9, the shifts of the transitional energies as a function of P and X are

$$\Delta E_{c-vA}(P, X) \equiv E_{c-vA}(P, X) - E_{c-vA}(P = 0kbar, X = 0kbar)$$

$$= \delta E_H^w + \delta E_b^w \quad , \tag{4.3.11a}$$

$$\Delta E_{c-vB}(P, X) \equiv E_{c-vB}(P, X) - E_{c-vB}(P = 0kbar, X = 0kbar)$$

$$= \delta E_{H}^{w} + \left[\frac{1}{3} + \frac{4\Delta_{cs1}}{9\Delta_{so}} \right] \delta E_{b}^{w}$$

$$- \left[\frac{2}{9\Delta_{so}} \right] \left[\delta E_{b}^{w} \right]^2 + \ldots , \qquad (4.3.11b)$$

and

$$\Delta E_{c-vC}(P, X) \equiv E_{c-vC}(P, X) - E_{c-vC}(P = 0kbar, X = 0kbar)$$

$$= \delta E_{H}^{w} + \left[\frac{2}{3} - \frac{4\Delta_{cs1}}{9\Delta_{so}} \right] \delta E_{b}^{w}$$

$$+ \left[\frac{2}{9\Delta_{so}} \right] \left[\delta E_{b}^{w} \right]^2 + \ldots . \qquad (4.3.11c)$$

The shifts of the transitional energies as a function of P (equation 4.3.11 with $X = 0kbar$) are plotted in figure 4.3.1. With $X = 0kbar$, the stress vector 4.3.4 is identical to the stress vector for hydrostatic pressure P. Consequently, the shifts of the three transitional energies are expected to have the same P dependence. This can be seen in figure 4.3.1, where all three lines (corresponding to the transitions from the conduction band to the valence subbands vA, vB, and vC) have the same slope ($\frac{\partial(\Delta E)}{\partial P} \approx 5.5meV/kbar$).

The shifts of the transitional energies as a function of X (equation 4.3.11 with $P = 0kbar$) are plotted in figure 4.3.2. The key salient feature of this figure is that the X dependence of the three conduction to valence subband transitional energies

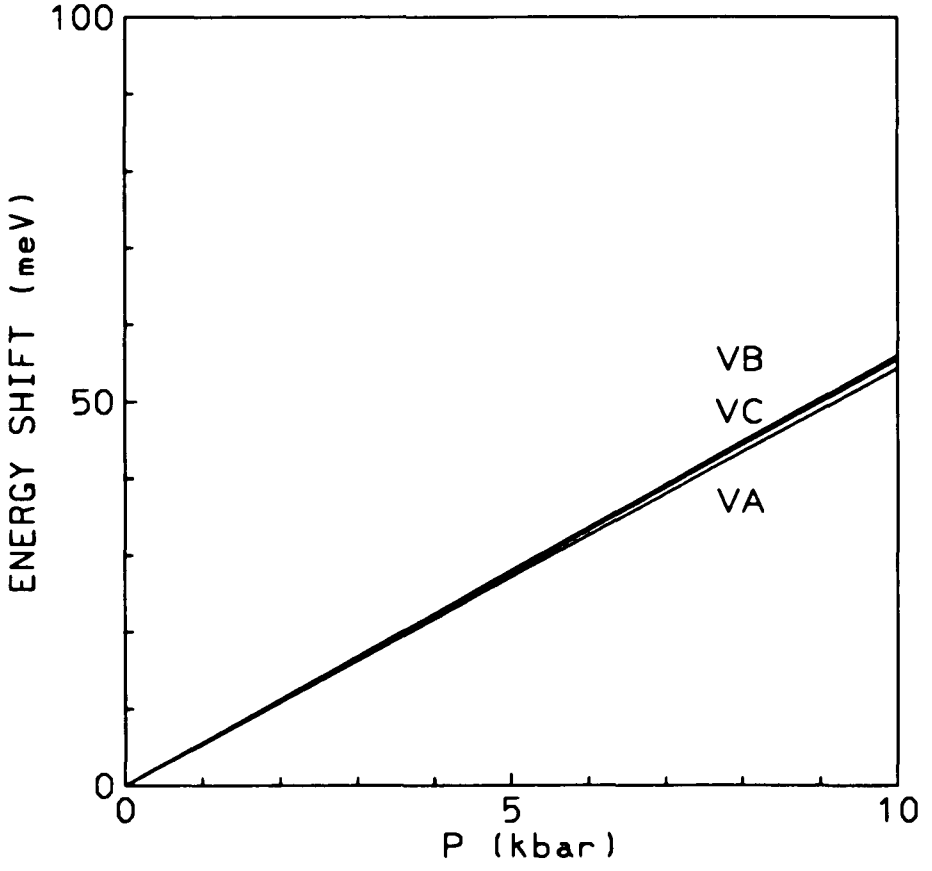

Figure 4.3.1. A plot of the shift in energy of the transition from the conduction to the valence subband v_A (VA), v_B (VB), v_C (VC) in CdSe as a function of P (equation 4.3.11 with $X = 0kbar$).

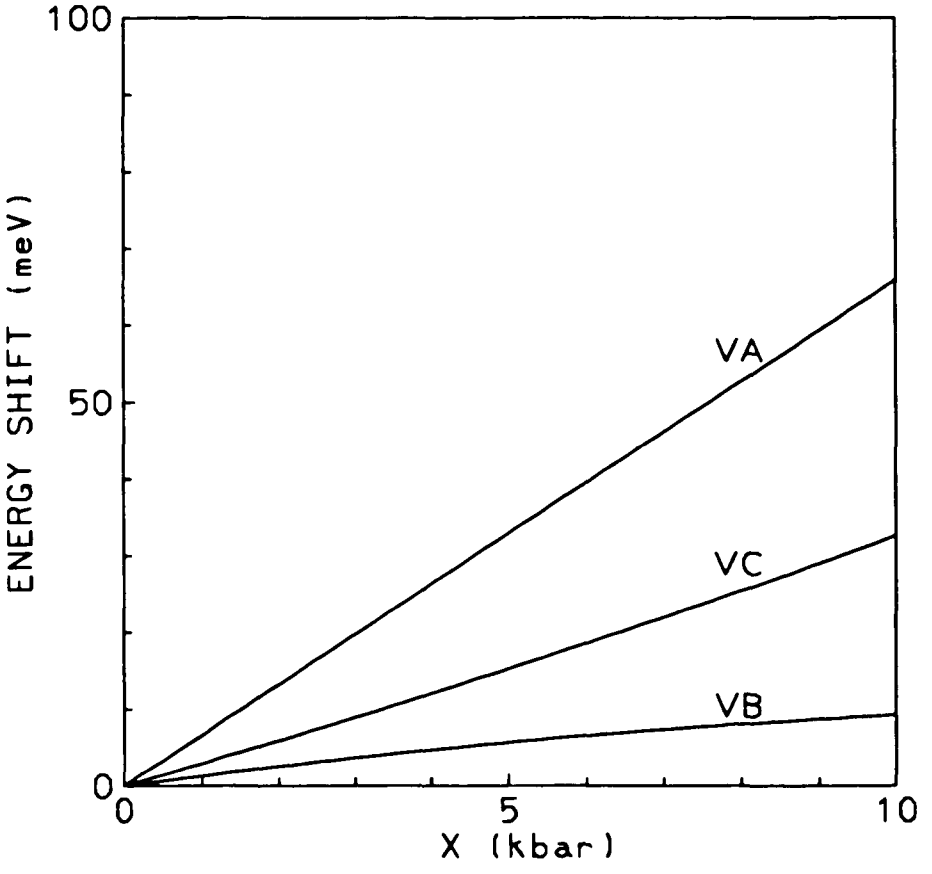

Figure 4.3.2. A plot of the shift in energy of the transition from the conduction to the valence subband v_A (VA), v_B (VB), v_C (VC) in CdSe as a function of X (equation 4.3.11 with $P = 0kbar$).

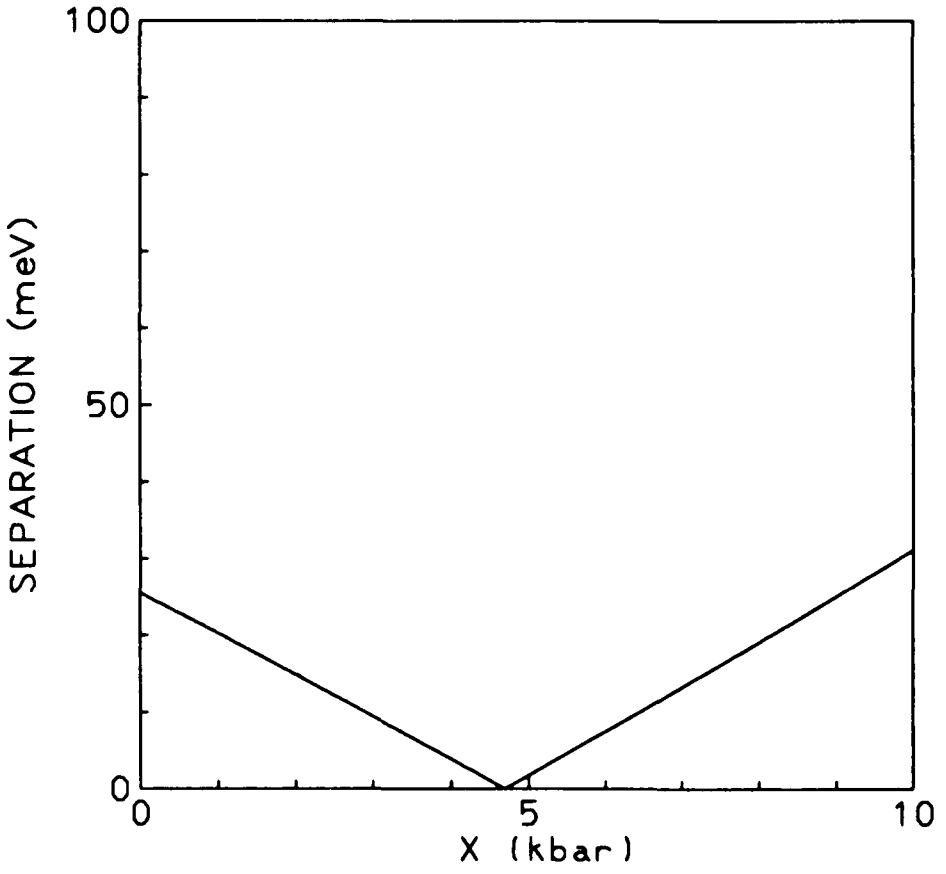

Figure 4.3.3. A plot of the separation between the valence subbands v_A and v_B (the absolute value of Δ_{AB} from equation 4.3.12a) as a function of X.

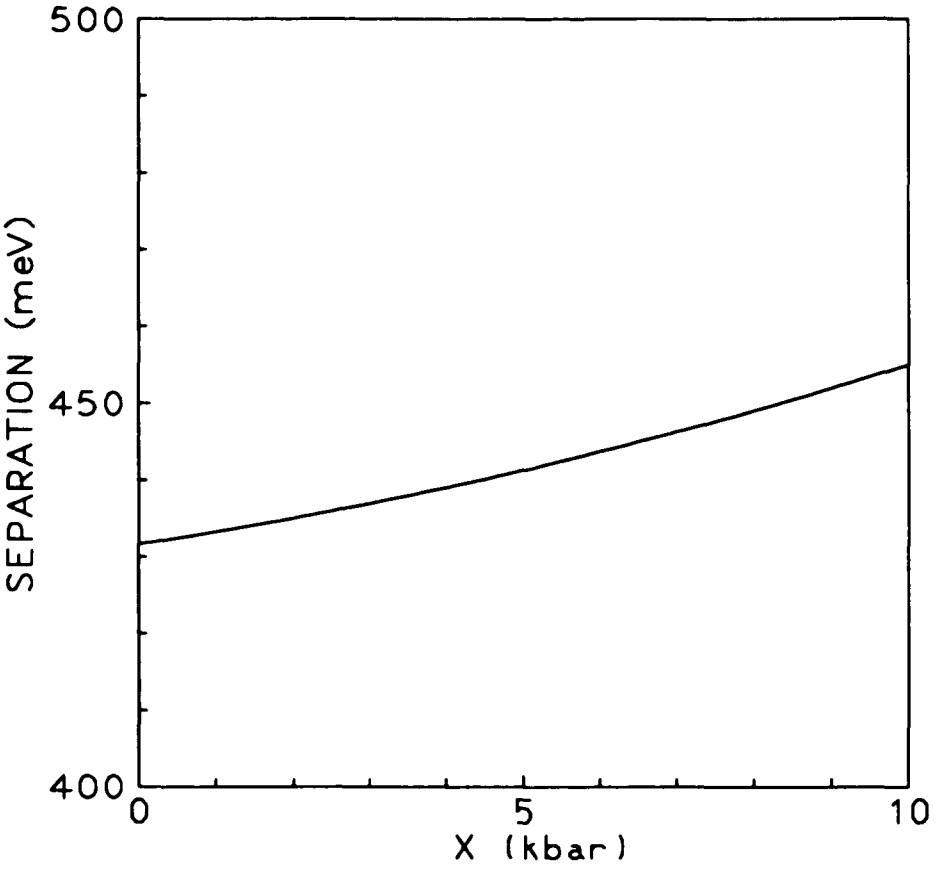

Figure 4.3.4. A plot of the separation between the valence subbands v_B and v_C (the absolute value of Δ_{BC} from equation 4.3.12b) as a function of X.

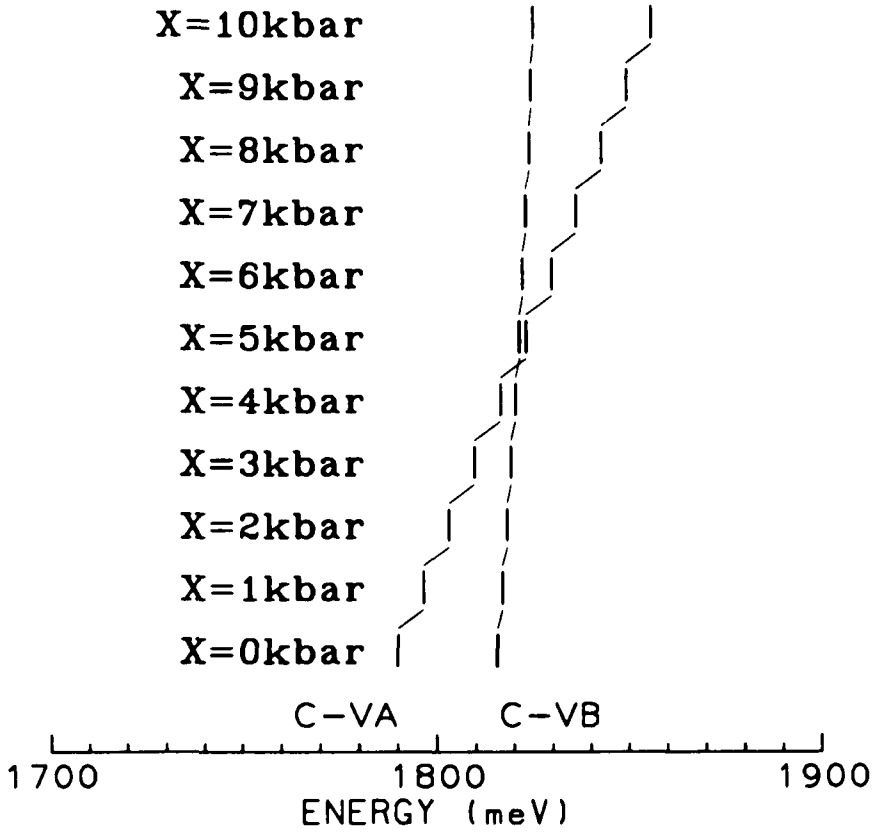

Figure 4.3.5. The energy positions of the PL emission lines corresponding to the $c-v_A$ and the $c-v_B$ transitions for various X (with $P = 0kbar$).

are all different. This implies that the gaps between the three valence subbands change with X and is independent of P (see figure 4.3.1). Defining

$$\Delta_{AB}(P, X) \equiv E_{c-vB}(P, X) - E_{c-vA}(P, X) \qquad (4.3.12a)$$

and

$$\Delta_{BC}(P, X) \equiv E_{c-vC}(P, X) - E_{c-vB}(P, X) \ , \qquad (4.3.12b)$$

the separations between the valence subbands are given by the absolute value of $\Delta_{AB}(P, X)$ and $\Delta_{BC}(P, X)$. The separations between the valence subbands are plotted as a function of X in figures 4.3.3 and 4.3.4, respectively. From figure 4.3.3, it can been seen that there is only $\sim 25meV$ change in the separation between the valence subbands v_A and v_B as a function of X (for $X = 0kbar$ to $10kbar$). The separation between the valence subbands v_A and v_B is seen to go to zero at $X \approx 5kbar$. This is due to larger shift of the valence subband vA relative to the valence subband vB as a function of X (see figure 4.3.2). For $X < \sim 5kbar$, the valence subband v_A is higher in energy then the valence subband v_B (while for $X > \sim 5kbar$, the valence subband v_B is higher in energy then the valence subband v_A). This can be seen in figure 4.3.5, where the energy positions of the PL emission lines corresponding to the $c-v_A$ and the $c-v_B$ transitions are plotted for $X = 0kbar$ to $X = 10kbar$ (with $P = 0kbar$). For $P \neq 0kbar$, both PL emission lines corresponding to v_A ($c-v_A$) and v_B ($c-v_B$) transitions (shown in figure 4.3.5) will be blue shifted by the same amount.

From these figures, it is expected that if the luminescence due to the $c-v_A$ and

$c-v_B$ transitions can be resolved in the PL spectra, the longitudinal and transverse stress components of the shock wave can be determined from the splitting and blue shifts of the PL spectra. The PL spectra from shock compressed CdSe will be discussed in the next section.

4.3B Shock Compressed CdSe

For the shock compression experiment, the shock wave facility described in section 3.3 is used. A $25mJ$ pump pulse from the Nd^{+3}:YAG laser is focused to a $500\mu m$ diameter spot on the aluminum foil to generate the shock wave. The $20\mu m$ aluminum foil is glued to the back surface of the $40\mu m$ CdSe Sulfur-free single crystal sample with Apiezon N-grease. This is sandwiched between two $3.175mm$ quartz discs, and then suspended in a liquid nitrogen optical dewar. The $300nJ$ probe pulse which is collinear and counter-propagating relative to the pump pulse is focused to a $400\mu m$ diameter spot on the front surface of the sample ($10^{15} photons/cm^2$). The PL is dispersed by the spectrograph and detected by the photodiode array. Data are recorded with the sample at $T = 85K$.

A representative spectra of the PL from the unshocked and shocked CdSe is shown in figure 4.3.6. The PL from the unshocked CdSe peaks at $\sim 1790meV$ (with a FWHM of $\sim 27meV$). Under shock compression, the PL blue shifts to $\sim 1840meV$ (with a FWHM of $\sim 46meV$). Comparing figure 4.3.6 to figure 4.3.5, the $c-v_A$ transition is easily observable whereas the $c-v_B$ transition is not readily observable. Since the $c-v_B$ transition is not observable, the energy separation between the $c-v_A$ transition and the $c-v_B$ transition can not be determined experimentally. Consequently, X can not be determined. If the assumption that $X = 0kbar$ is made, the shock pressure P can be determined from the blue shift in the PL spectra. Using $\frac{\partial E}{\partial P} \approx 6meV/kbar$, the shock pressure P can be obtain by dividing the energy of

the blue shift by $\frac{\partial E}{\partial P}$. By varying the delay between the pump and the probe, the time evolution of the shock pressure can be determined from the shift in the PL spectra. The shock profile determined in this manner is shown in figure 4.3.7.

Another interesting feature seen in figure 4.3.6 is the increase in the observed PL intensity from the shock compressed CdSe as compared to the unshocked CdSe. This will be discussed further in chapter 5 (p. 136).

In summary, from the shift of the PL from CdSe under shock compression, the time evolution of the shock pressure P has been determined. The difference between the longitudinal and transverse stress components of the shock wave ($[P + X] - [P] = X$) can not be determined in these shock compression experiments. There are two main problems encountered in this experiment. First, the PL lines corresponding to the $c-v_B$ transition and the $c-v_A$ transition can not be resolved. Second, within the range of shock pressure of interest, the transition with the lowest energy can be either $c-v_A$ or $c-v_B$ (see figure 4.3.5). This makes the analysis of the shock compression experiment very difficult. Therefore, two criteria that must be met in order to determine the transverse and longitudinal stress components of the shock wave are: 1) the PL emission lines corresponding to two transition which separate as a function of X must be clearly resolved; and 2) the ordering of the energy of the two transitions should not change within the pressure range of interest. In the next section, it will be shown that the valence bands of GaAs have the appropriate X behavior needed for a unique determination of the transverse

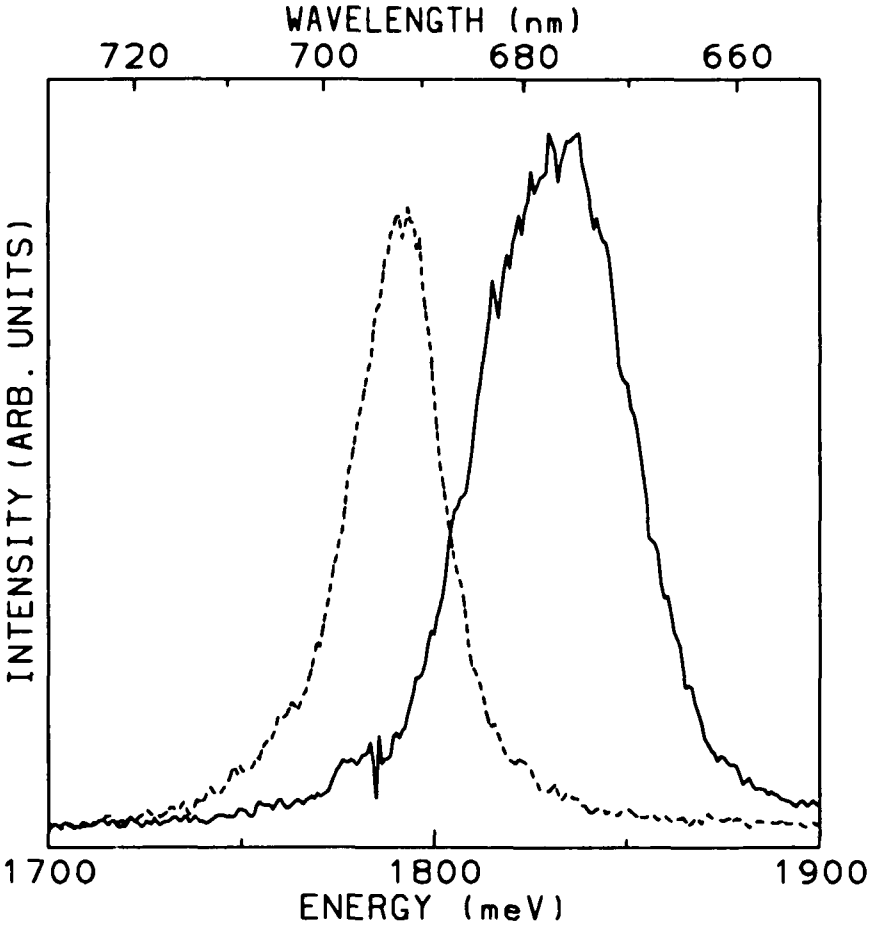

Figure 4.3.6. A plot of the unshocked (---) and shocked (—) spontaneous emission spectra from CdSe at low probe intensity ($300nJ$).

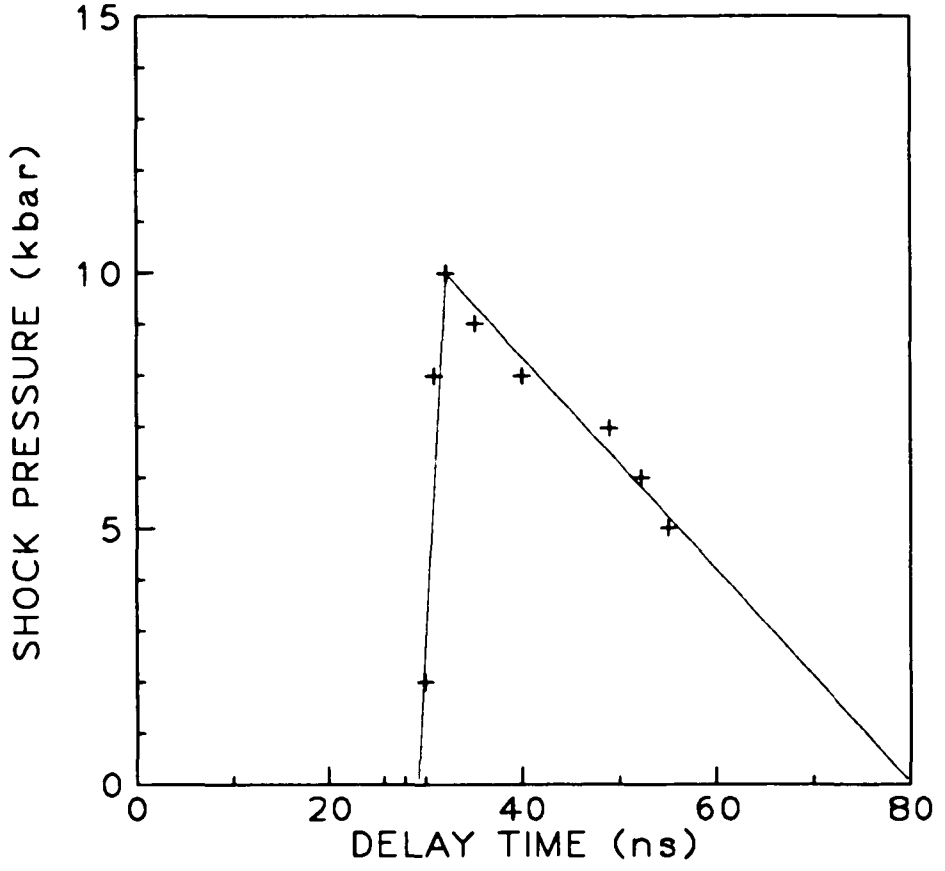

Figure 4.3.7. A plot of the time evolution of the shock pressure in CdSe.

and longitudinal stress components of the shock wave.

4.4 Gallium Arsenide Under Dynamic Stress

The third shock compression experiment is on GaAs.[104] In this experiment, it will be shown that GaAs meets the conditions necessary for the determination of both the transverse and longitudinal stress components of the shock wave.

In the next section, the unstressed band structure of GaAs will be described. Then, the usual strain Hamiltonian of GaAs is modified to describe shock compression. Finally, in section 4.4B, the results of the shock compression experiments on GaAs will be presented.

4.4A Theoretical Model

Gallium Arsenide (GaAs) is a III-V semiconductor with a zinc blende structure. The band structure is shown in figure 4.4.1. The lowest conduction band (c) has a s-type basis function and is characterized by Γ_7 symmetry at $k = 0$. The highest valence band has p-type basis functions. The usual six fold degeneracy at $k = 0$ is split into a four-fold degenerate subband (denoted $v1$ and $v2$) and a two-fold spin degenerate subband known as the split off (v_3) band by the spin orbit interaction,[105]

$$H_{so} = \frac{2\Delta_o}{3}\left[\mathbf{L}\cdot\bar{\boldsymbol{\sigma}} - \frac{1}{2}\right] , \tag{4.4.1}$$

where $\Delta_o = 341meV$ at $80K$, and $\mathbf{L}$ and $\bar{\boldsymbol{\sigma}}$ are the orbital and spin angular momentum operators, respectively.

From symmetry considerations,[100,106] the strain Hamiltonians for the valence band of a semiconductor with cubic symmetry (e.g., GaAs) have been given by Pollak[107] as

$$H_{orb(\varepsilon)} = a_1^z \left(\varepsilon_{11} + \varepsilon_{22} + \varepsilon_{33} \right)$$

$$+ 3b_1^z \left[\varepsilon_{11} (L_1^2 - \frac{1}{3} L^2) + c.p. \right]$$

$$+ 2\sqrt{3} d_1^z \left[\varepsilon_{12} \{ L_1, L_2 \} + c.p. \right] , \qquad (4.4.2a)$$

$$H_{spin(\varepsilon)} = 2a_2^z \left(\varepsilon_{11} + \varepsilon_{22} + \varepsilon_{33} \right) \mathbf{L} \cdot \bar{\boldsymbol{\sigma}}$$

$$+ 6b_2^z \left[\varepsilon_{11} (L_1 \bar{\sigma}_1 - \frac{1}{3} \mathbf{L} \cdot \bar{\boldsymbol{\sigma}}) + c.p. \right]$$

$$+ 2\sqrt{3} d_2^z \left[\varepsilon_{12} (L_1 \bar{\sigma}_2 + L_2 \bar{\sigma}_1) + c.p. \right] , \qquad (4.4.2b)$$

where ε_{ij} is the strain tensor, and a_1^z, a_2^z, b_1^z, b_2^z, d_1^z, and d_2^z are the deformation potentials. Similarly, for the conduction band,

$$H_{c(\varepsilon)} = -a_c^z \left(\varepsilon_{11} + \varepsilon_{22} + \varepsilon_{33} \right) , \qquad (4.4.3)$$

where a_c^z is the deformation potential for the conduction band.

To rewrite the strain Hamiltonians in terms of stress, the elastic compliance is needed. For cubic lattices (e.g., GaAs), the elastic compliance is

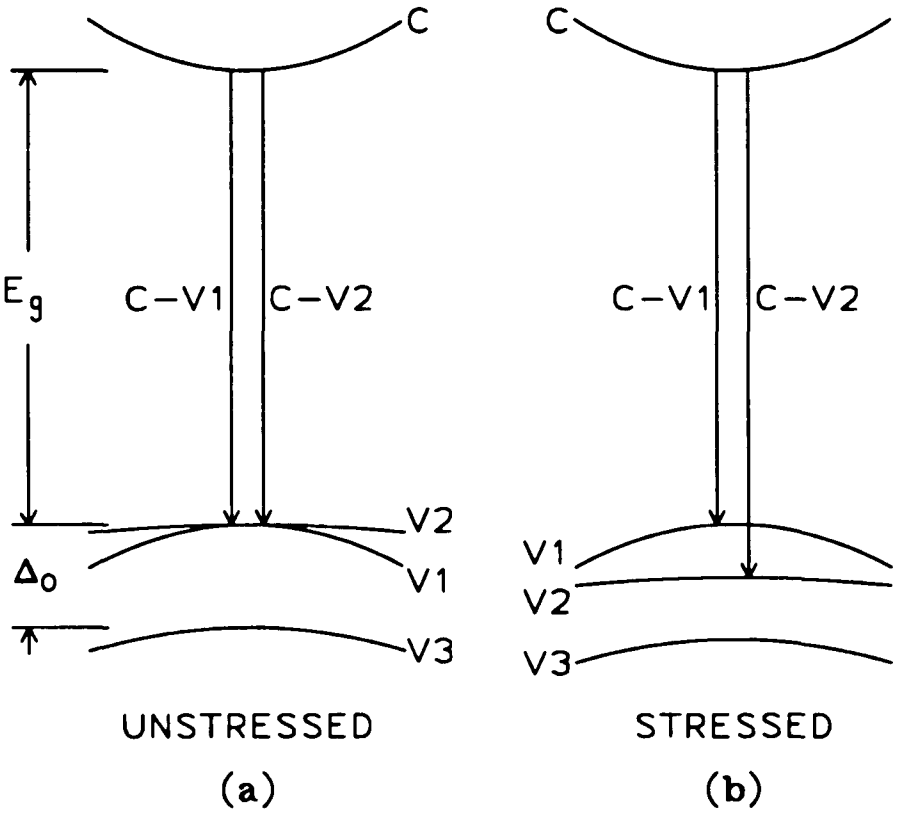

Figure 4.4.1. Schematic diagram of the a) unstressed and b) stressed GaAs band structure. The conduction band is denoted by C and the three valence subbands are labeled $V1$, $V2$, and $V3$.

$$\mathbf{s} \equiv \begin{pmatrix} S_{11}^z & S_{12}^z & S_{12}^z & 0 & 0 & 0 \\ S_{12}^z & S_{11}^z & S_{12}^z & 0 & 0 & 0 \\ S_{12}^z & S_{12}^z & S_{11}^z & 0 & 0 & 0 \\ 0 & 0 & 0 & S_{44}^z & 0 & 0 \\ 0 & 0 & 0 & 0 & S_{44}^z & 0 \\ 0 & 0 & 0 & 0 & 0 & S_{44}^z \end{pmatrix} . \tag{4.4.4}$$

The constants for GaAs[108] are $S_{11}^z = 1.2\times10^{-3} kbar^{-1}$, $S_{12}^z = -0.4\times10^{-3} kbar^{-1}$, and $S_{44}^z = 1.7\times10^{-3} kbar^{-1}$.

Using equations 2.2.7, 4.4.4, and 4.3.4 the strain stress relationship for shock compression along the [001] axis in cubic semiconductors becomes

$$\varepsilon_{11} = \varepsilon_{22} = -\left(S_{11}^z + 2S_{12}^z\right)P - S_{12}^z X \ , \tag{4.4.5a}$$

$$\varepsilon_{33} = -\left(S_{11}^z + 2S_{12}^z\right)P - S_{11}^z X \ , \tag{4.4.5b}$$

and

$$2\varepsilon_{23} = 2\varepsilon_{31} = 2\varepsilon_{12} = 0 \ . \tag{4.4.5c}$$

Note that for $P = 0 kbar$, the usual strain stress relationships for static uniaxial stress along the [001] axis are obtained from equation 4.4.5. Using the wave functions $\Phi_i \equiv \left[J, J_{[001]}\right]$, with

$$\Phi_{v2} \equiv \left[\frac{3}{2}, \frac{3}{2}\right] = P_+ \chi_\uparrow \ , \tag{4.4.6a}$$

$$\Phi_{v1} \equiv \left[\frac{3}{2}, \frac{1}{2}\right] = \frac{1}{\sqrt{3}} P_+ \chi_\downarrow - \frac{\sqrt{2}}{\sqrt{3}} P_z \chi_\uparrow \ , \tag{4.4.6b}$$

and

$$\Phi_{v3} \equiv \left[\frac{1}{2}, \frac{1}{2}\right] = \frac{\sqrt{2}}{\sqrt{3}} P_{+}\chi_{\downarrow} + \frac{1}{\sqrt{3}} P_{z}\chi_{\uparrow} \quad , \tag{4.4.6c}$$

where $P_{+} \equiv \frac{1}{\sqrt{2}}\left[P_x + iP_y\right]$, P_x, P_y, and P_z, are the p-like basis functions, and $\chi_{\uparrow}$ and $\chi_{\downarrow}$ are the spin basis functions; the Hamiltonian matrix[109] for shock compression along the [001] axis of GaAs can be formed from equations 4.4.1, 4.4.2, and 4.4.5 (see Appendix A2),

$$\mathbf{H}_{\sigma} \equiv \begin{array}{c} \begin{matrix} \Phi_{v2} & \Phi_{v1} & \Phi_{v3} \end{matrix} \\ \begin{bmatrix} \Lambda_2^z & 0 & 0 \\ 0 & \Lambda_1^z & \Lambda_{13}^z \\ 0 & \Lambda_{13}^z & \Lambda_3^z \end{bmatrix} \end{array} . \tag{4.4.7}$$

The components are

$$\Lambda_2^z = -\delta E_{II}^{v} - \frac{\delta E_{001}}{2} \quad , \tag{4.4.8a}$$

$$\Lambda_1^z = -\delta E_{II}^{v} + \frac{\delta E_{001}}{2} \quad , \tag{4.4.8b}$$

$$\Lambda_3^z = -\Delta_o - \delta E_{II}^{v} \quad , \tag{4.4.8c}$$

and

$$\Lambda_{13}^z = \frac{\sqrt{2}\delta E_{\overline{001}}}{2} \quad ; \tag{4.4.8d}$$

with

$$\delta E_{II}^{v} \equiv (a_1^z + a_2^z)(S_{11}^z + 2S_{12}^z)(3P + X) \quad , \tag{4.4.9a}$$

$$\delta E_{II}^{v} \equiv (a_1^z - 2a_2^z)(S_{11}^z + 2S_{12}^z)(3P + X) \quad , \tag{4.4.9b}$$

$$\delta E_{001} \equiv 2(b_1^z + 2b_2^z)(S_{11}^z - S_{12}^z)X \quad , \tag{4.4.9c}$$

and

$$\delta E_{\overline{001}} \equiv 2(b_1^z - b_2^z)(S_{11}^z - S_{12}^z)X \quad . \tag{4.4.9d}$$

The constants a_2^z, b_2^z, and d_2^z have been founded to be smaller then the measurement errors.[110] Consequently,[111] the $H_{spin(\varepsilon)}$ can be neglected compared to $H_{orbit(\varepsilon)}$. This implies that $\delta E_{H}^{\varepsilon} = \delta E_{H}^{s}$ and $\delta E_{\overline{001}} = \delta E_{001}$. The constants for GaAs are $a_c^z + a_1^z = 8720meV$, $b_1^z = 2000meV$, and $d_1^z = 4430meV$. The conduction band deformation potential for GaAs is[112] $a_c^z = 9300(\pm 1000)meV$ which yields $a_1^z = -580(\pm 1000)meV$.

The eigenvalues of equation 4.4.7 give the energy shifts (with respect to the conduction band) of the GaAs valence subband v_1, v_2, and v_3 (see Appendix A2). The shifts of the transitional energies with P and X are

$$\Delta E_{c-v1}(P, X) \equiv E_{c-v1}(P, X) - E_{c-v1}(P = 0kbar, X = 0kbar)$$

$$= \delta E_{H}^{s} - \frac{\delta E_{001}}{2} - \frac{\delta E_{001}^2}{2\Delta_o} + \ldots \quad , \tag{4.4.10a}$$

$$\Delta E_{c-v2}(P, X) \equiv E_{c-v2}(P, X) - E_{c-v2}(P = 0kbar, X = 0kbar)$$

$$= \delta E_{H}^{s} + \frac{\delta E_{001}}{2} \quad , \tag{4.4.10b}$$

and

$$\Delta E_{c-v3}(P, X) \equiv E_{c-v3}(P, X) - E_{c-v3}(P = 0kbar, X = 0kbar)$$

$$= \delta E_H^s + \frac{\delta E_{001}^2}{2\Delta_o} + \ldots , \qquad (4.4.10c)$$

where $\delta E_H^s \equiv (a_c^z + a_1^z)(S_{11}^z + 2S_{12}^z)(3P + X)$. From equations 4.4.10a and 4.4.10b, the four-fold degenerate valence subband of GaAs is split into two spin degenerate subbands (v_1 and v_2) under uniaxial stress. From equation 4.4.10b (for a given P), the valence subband $v2$ shifts linearly with X. The shifts of the $v1$ and $v3$ valence subbands have a nonlinear dependence on X due to the coupling between the $v1$ and $v3$ wave functions (i.e., the stress Hamiltonian is nondiagonal). In the $v1$ ($v3$) bands, δE_H^s and δE_{001} subtract (add). Therefore, since the difference of δE_H^s and δE_{001} almost cancels the X dependence, the $v1$ shift depends mainly on P, while $v3$ increases monotonically with both P and X.

It can be seen from equations 4.4.10 that the energy shifts of the v_1, v_2, and v_3 valence subbands as a function of X relative to the energy shift at $X = 0kbar$ are independent of P. Rewriting equations 4.4.10 as

$$\Delta \bar{E}_{c-v1}(X) \equiv \Delta E_{c-v1}(P, X) - \Delta E_{c-v1}(P, X = 0kbar)$$

$$= \delta E_H - \frac{\delta E_{001}}{2} - \frac{\delta E_{001}^2}{2\Delta_o} + \ldots , \qquad (4.4.11a)$$

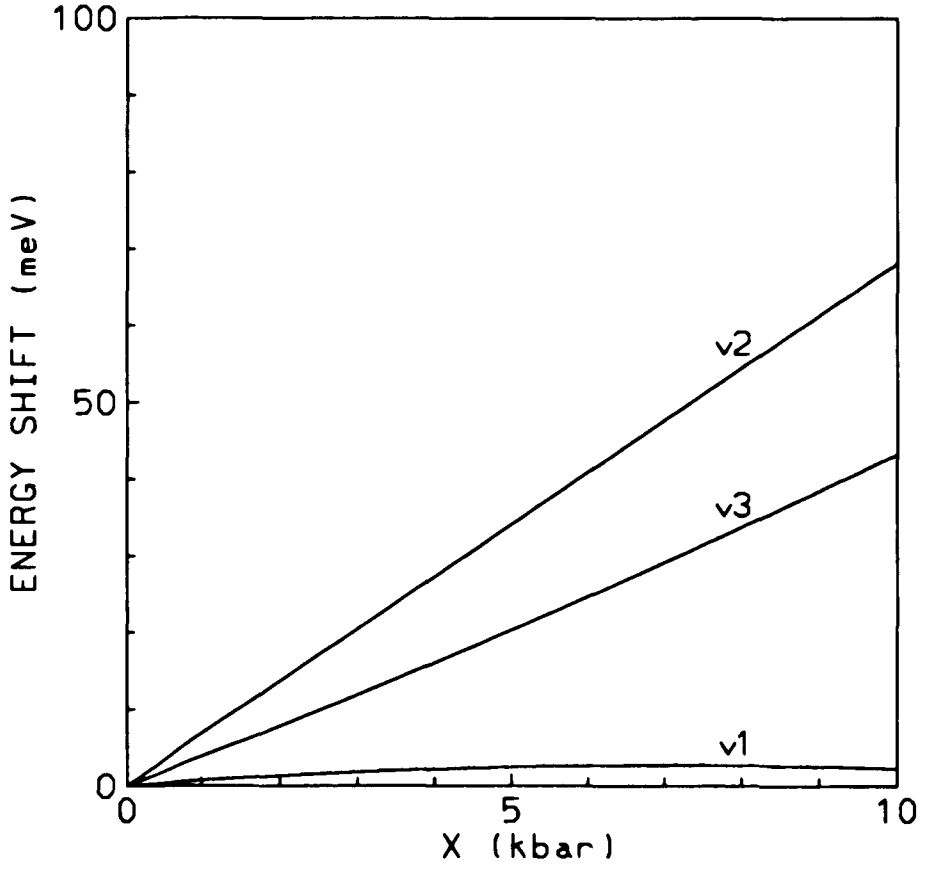

Figure 4.4.2. A plot of the energy shift of the v_1, v_2, and v_3 valence subbands (equation 4.4.11) as a function of X.

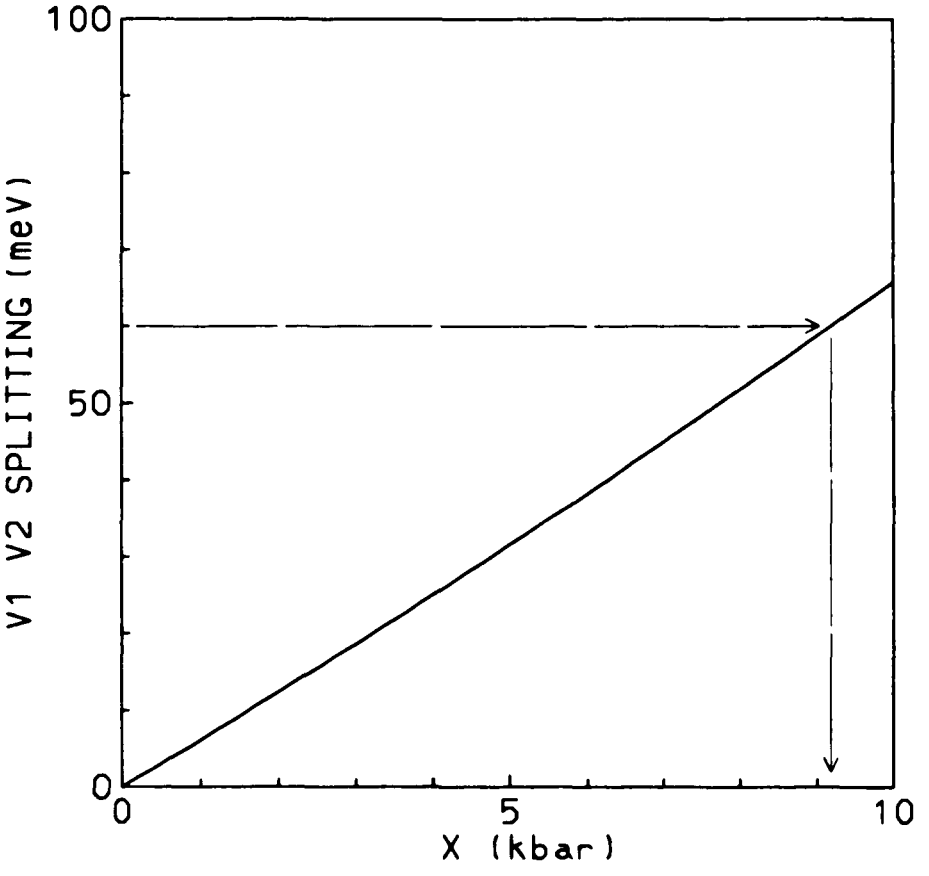

Figure 4.4.3. A plot of the separation between the GaAs valence subbands v_1 and v_2 (Δ_{12}) as a function of X (equation 4.4.12).

$$\Delta\bar{E}_{c-v2}(X) \equiv \Delta E_{c-v2}(P, X) - \Delta E_{c-v2}(P, X = 0kbar)$$

$$= \delta E_H + \frac{\delta E_{001}}{2} \quad , \tag{4.4.11b}$$

and

$$\Delta\bar{E}_{c-v3}(X) \equiv \Delta E_{c-v3}(P, X) - \Delta E_{c-v3}(P, X = 0kbar)$$

$$= \delta E_H + \frac{\delta E_{001}^2}{2\Delta_o} + \ldots \quad , \tag{4.4.11c}$$

where $\delta E_H \equiv (a_c^z + a_1^z)(S_{11}^z + 2S_{12}^z)X$. The energy shifts $\Delta\bar{E}_\alpha$ for the three valence subbands are plotted in figure 4.4.2. The essential features this figure are: 1) the conduction to $v2$ and $v3$ valence subband transitional energies increase monotonically with X ($< 10kbar$); 2) the conduction to $v1$ valence subband transitional energy has less than $3meV$ shift with X ($< 10kbar$); and 3) all three conduction to valence subband transitional energies have different X dependence. Therefore, the gap between the valence subband v_1 and v_2 should change as a function of X. The gap between the valence subband v_1 and v_2 is given by

$$\Delta_{12}(X) \equiv \Delta E_{c-v2}(P, X) - \Delta E_{c-v1}(P, X) = \delta E_{001} + \frac{\delta E_{001}^2}{2\Delta_o}$$

$$= 2b_1(S_{11} - S_{12})X + \frac{2b_1^2(S_{11} - S_{12})^2X^2}{\Delta_o} \quad . \tag{4.4.12}$$

This is plotted in figure 4.4.3. It can be seen that Δ_{12} is a function only of X. Therefore, the uniaxial component X of shock compression can be monitored by observing Δ_{12} via the PL spectra. As Δ_{12} increases, the observed PL line width will

broaden because the lines are overlapping until finally two blue shifted PL bands are resolved (when Δ_{12} is greater than the line widths of either the ν_1 or the ν_2 PL bands). This effect has been observed in the shock compression experiment on n-GaAs. The results of this shock compression experiment are described in the next section.

4.4B Shock Compressed GaAs

In this shock compression experiment, a $40\mu m$ n-GaAs sample is glued to a quartz disc with optical glue. An aluminum foil is then glued to the back surface of the sample with Apiezon N-grease. The final layer is another quartz disc. This is then suspended in a liquid nitrogen optical dewar. For this experiment, the $25mJ$ pump pulse is focused to a $500\mu m$ diameter spot on the aluminum foil. The $500nJ$ probe pulse which is collinear and counter-propagating relative to the pump pulse is focused to a $400\mu m$ diameter spot on the front surface of the sample ($10^{15} photons/cm^2$). Data are recorded with the sample at $T = 80K$. Plotted in figure 4.4.4, are the PL spectra from the shocked and unshocked bulk n-GaAs at various delay times between the pump and the probe pulses. The relevant transitions in stressed and unstressed GaAs are shown schematically in figure 4.4.1. As the delay time between pump and probe is increased, the shocked PL spectra is observed to be blue shifted (see figure 4.4.4a) and eventually splits into two blue shifted PL lines (see figure 4.4.4b). These two blue shifted PL lines correspond to the transitions from the Γ_6 conduction to the $v1$ valence subbands ($c-v1$) and the $v2$ valence subbands ($c-v2$) (see figure 4.4.1b). At further increases of the delay time, the splitting of the two blue shifted PL lines decreases and merges into a broaden line (see figure 4.4.4c).

From the bulk n-GaAs shock compression data, the spontaneous PL is observed to split into two blue shifted lines, corresponding to the transitions from

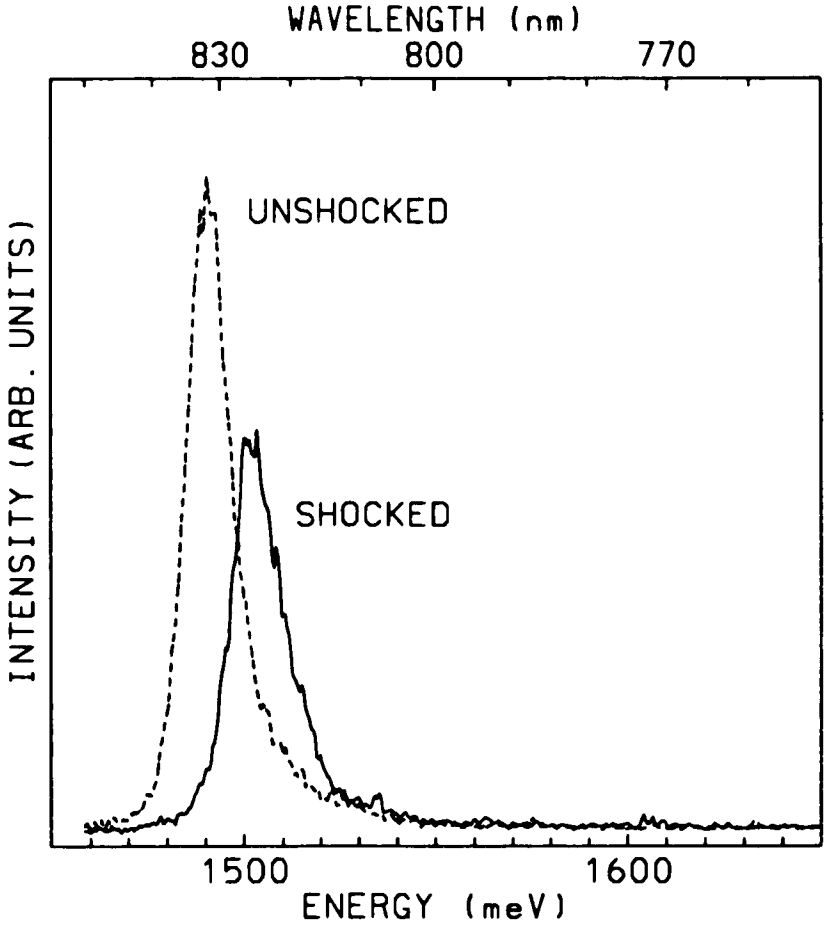

Figure 4.4.4a. A plot of the unshocked (---) and shocked (—) spontaneous emission spectra from n-GaAs at low probe intensity ($500nJ$) for a delay time of $33ns$.

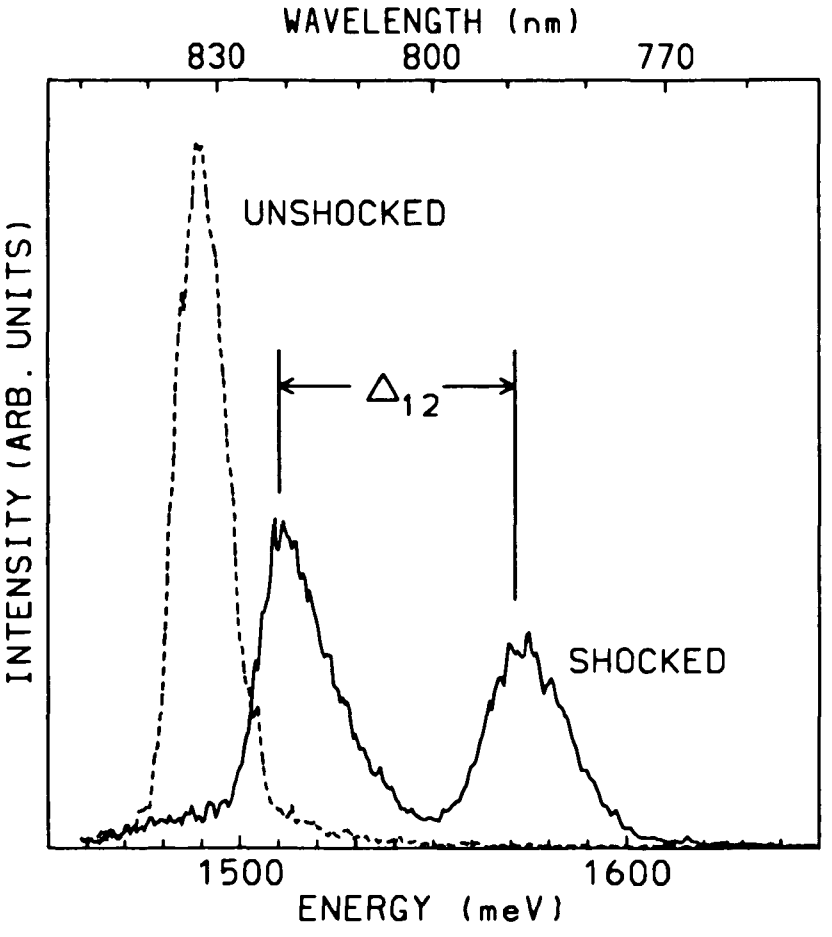

Figure 4.4.4b. A plot of the unshocked (---) and shocked (—) spontaneous emission spectra from n-GaAs at low probe intensity ($500nJ$) for a delay time of $46ns$.

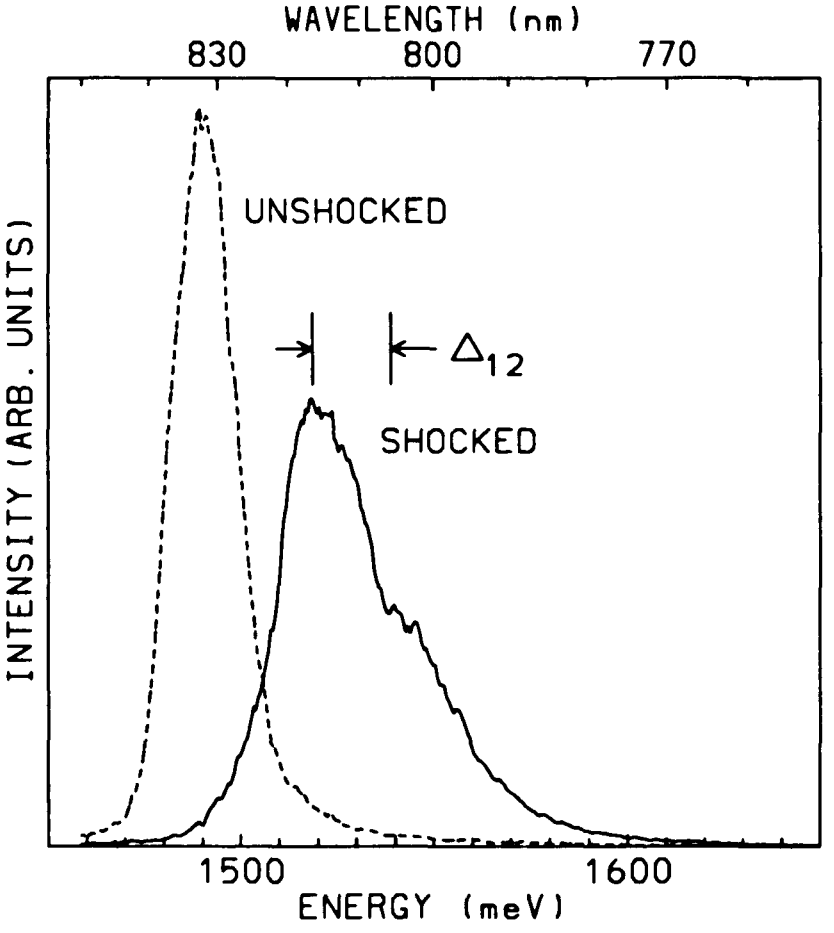

Figure 4.4.4c. A plot of the unshocked (---) and shocked (—) spontaneous emission spectra from n-GaAs at low probe intensity ($500nJ$) for a delay time of $73ns$.

the Γ_6 conduction (c) to the $v1$ valence and the $v2$ valence subbands due to symmetry breaking by the transient uniaxial component of the shock compression along the [001] direction. From the experimentally observed separation of the two PL bands (see Δ_{12} in figure 4.4.4b), the stress X can be obtain from equation 4.4.12 or from figure 4.4.3. For example, from figure 4.4.4b, $\Delta_{12} \approx 60meV$, then in figure 4.4.3, a horizontal line corresponding to a $60meV$ splitting intersects the curve at $X \approx 9kbar$. Then, the hydrostatic pressure P can be determined from equation 4.4.10a, since both X and ΔE_{c-v1} are known. Considering the same example (figure 4.4.4b), a blue shift of $\Delta E_{c-v1} \approx 20meV$, together with $X \approx 9kbar$ in equation 4.4.10a, yields $P \approx 2kbar$. The longitudinal $(P + X)$ and transverse (P) components of the shock wave are plotted in figure 4.4.5 as a function of the delay time between pump and probe. These stress components are not equal over $\sim 50ns$. These experimentally determined stress components are average values since there exists some shock pressure inhomogeneity in the probe region. From the line shape broadening,[113] the shock pressure inhomogeneity over the probe region is estimated to be $\pm 0.3kbar/10kbar = \pm 3\%$.

From figure 4.4.5 it is quite clear that the uniaxial component (X) is non-zero for shock propagation along the [001] axis in GaAs. Therefore, any analysis of shock compression must consider the time interval needed for the longitudinal and transverse stress components to equilibrate. After this time interval, the usual hydrostatic pressure analysis may be used.

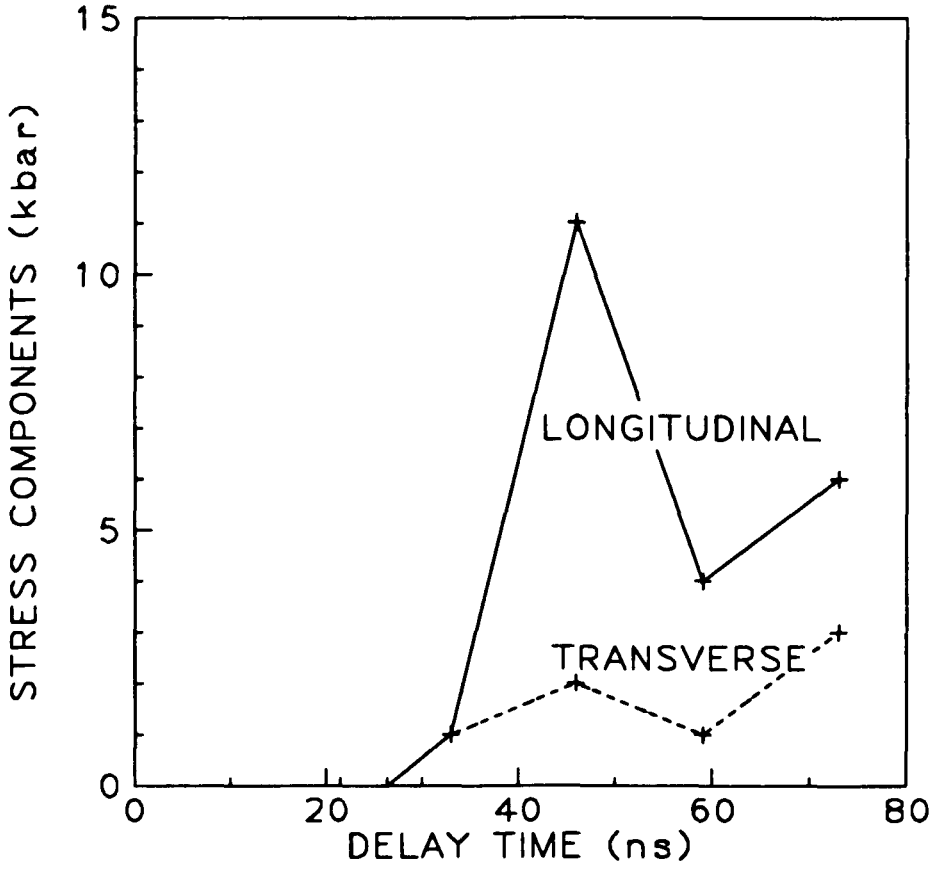

Figure 4.4.5. A plot of the longitudinal and transverse stress components of a shock wave propagating along the [001] axis of n-GaAs.

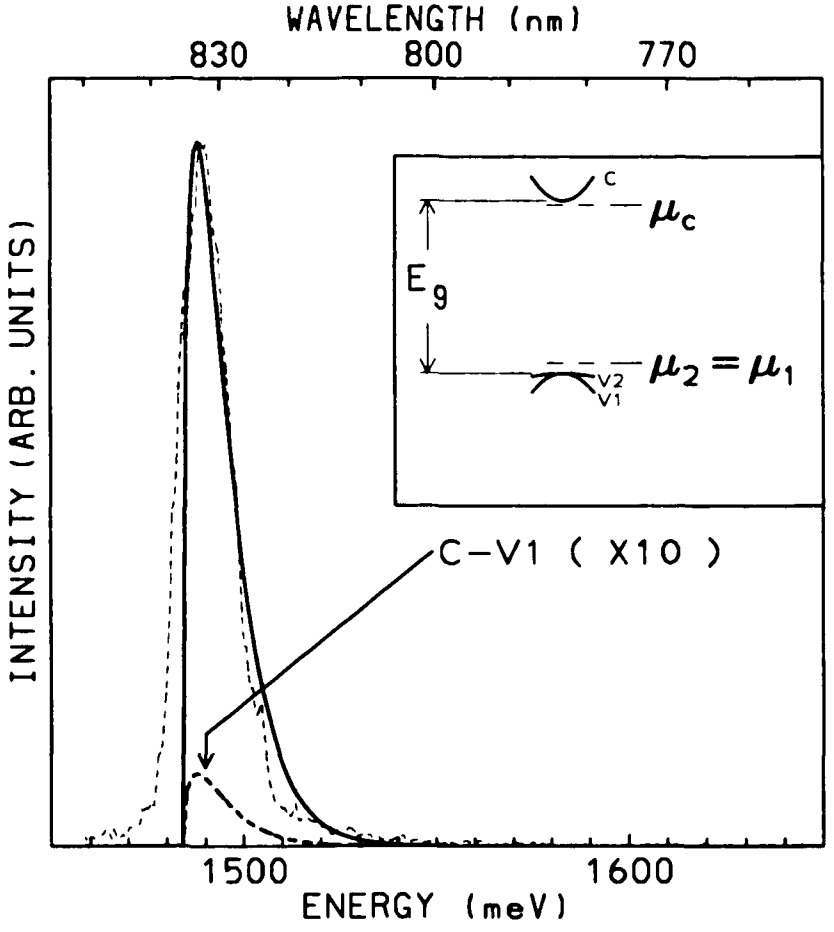

Figure 4.4.6. A plot of the unshocked spectra (---) from figure 4.4.4b together with the EHP line shape (—) using the parameters $T_c = T_1 = T_2 = 80K$, $E_g = 1484meV$, $\mu_c = -11meV$, $\Delta_1 = \Delta_2 = 0meV$, and $\mu_1 = \mu_2 = -1451meV$ in equation 4.4.13. The positions of the quasi-Fermi levels relative to the band edges are shown in the insert.

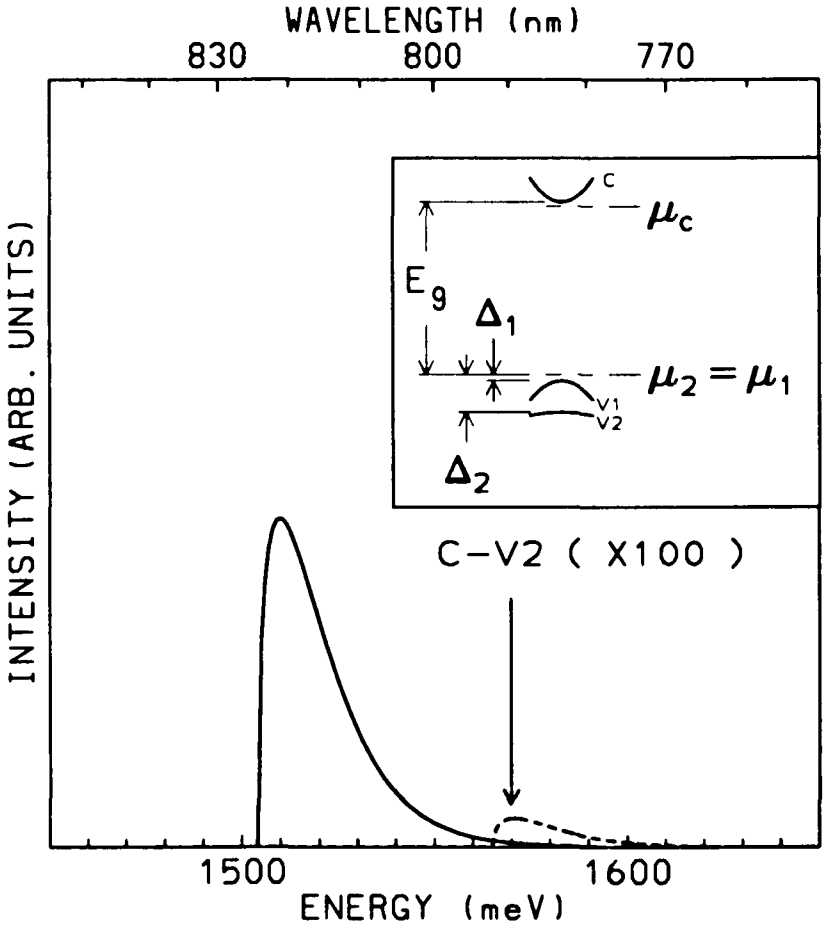

Figure 4.4.7. A plot of the EHP line shape using the parameters $T_c = T_1 = T_2 = 120K$, $E_g = 1484meV$, $\mu_c = -16meV$, $\Delta_1 = 20meV$, $\Delta_2 = 81meV$, and $\mu_1 = \mu_2 = -1484meV$ in equation 4.4.13. The positions of the quasi-Fermi levels relative to the band edges are shown in the insert.

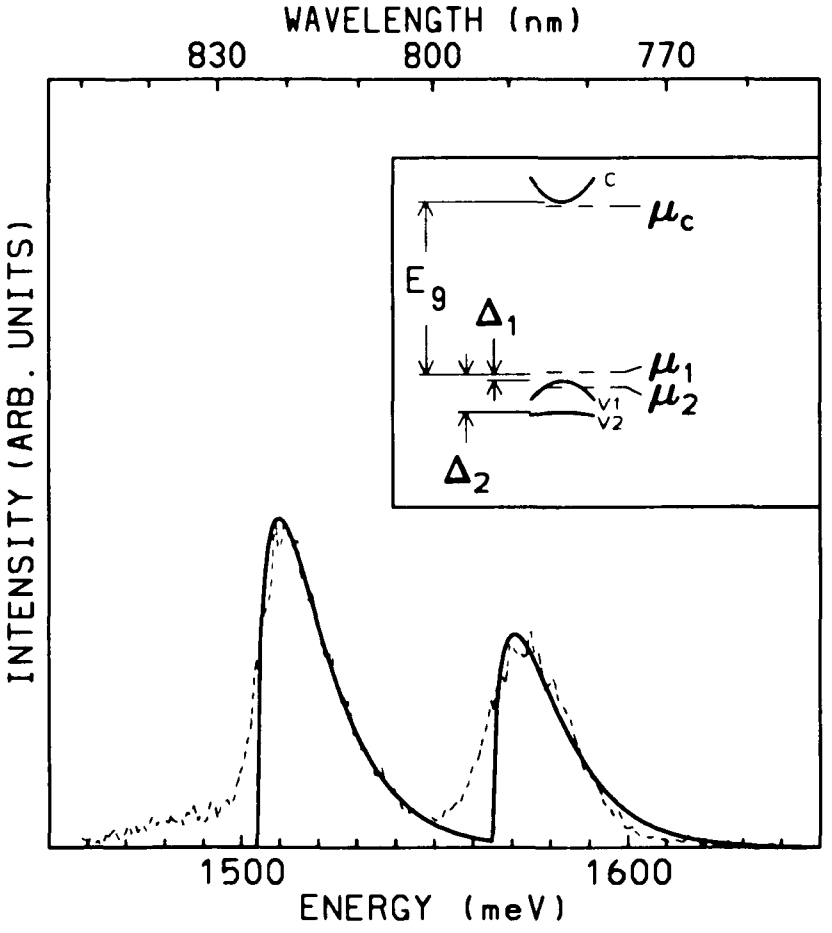

Figure 4.4.8. A plot of the shocked spectra (---) from figure 4.4.4b together with the EHP line shape (—) using the parameters $T_c = T_1 = T_2 = 120K$, $E_g = 1484meV$, $\mu_c = -16meV$, $\Delta_1 = 20meV$, $\Delta_2 = 81meV$, $\mu_1 = -1476meV$, and $\mu_2 = -1510meV$ in 4.4.13. The positions of the quasi-Fermi levels relative to the band edges are shown in the insert.

It is also interesting to note that the $c-v2$ PL line in figure 4.4.4b is strong. The PL line shape due to band to band transitions (see Appendix A4) is given as

$$I(h\nu) = I_o \sum_j \xi_j \left[\frac{m_{rcj}}{m_c} \right]^{3/2} \left[\frac{h\nu}{E_g} \right] \left[\frac{h\nu}{E_g} - \frac{\Delta_g}{E_j} - 1 \right]^{1/2}$$

$$\times \eta_j \, f_j^c(h\nu) \, f_j^{ch}(h\nu) \quad , \tag{4.4.13}$$

where I_o is a constant, $\eta_j = \dfrac{n_j}{\sum_i n_i}$, n_j is the density of holes in the $j^{\underline{th}}$ valence subband, ξ_j is the matrix element constant for transitions from the conduction band c to the $j^{\underline{th}}$ valence subband, $m_{rcj} \equiv \dfrac{m_c m_j}{m_c + m_j}$ is the reduced mass, m_c and m_j are the effective mass of the electrons and holes, E_g is the band gap, Δ_j are the energy shifts due to stress,

$$f_j^c(h\nu) = \left[1 + e^{\beta_c \left(\frac{m_{rcj}}{m_c} (h\nu - E_g - \Delta_j) - \mu_c \right)} \right]^{-1} \quad , \tag{4.4.14a}$$

$$f_j^{ch}(h\nu) = \left[e^{\beta_j \left(\frac{m_{rcj}}{m_j} (h\nu - E_g - \Delta_j) + E_g + \Delta_j + \mu_j \right)} + 1 \right]^{-1} \quad , \tag{4.4.14b}$$

$\beta_{c(j)} = (k_b T_{c(j)})^{-1}$, k_b is the Boltzmann constant, $T_{c(j)}$ are the characteristic temperatures of the electrons (holes), and $\mu_{c(j)}$ are the quasi-Fermi levels of the electrons (holes). The are two key features in equation 4.4.13: $I(h\nu) \equiv 0$ for $h\nu < E_g + \Delta_j$, since only transitions from a parabolic conduction band to two parabolic valence subbands are considered; and the PL line shape is dominated by the

density of carriers via the factors η_j, $f_j^c(h\nu)$, and $f_j^{ch}(h\nu)$. The $\xi_j \left[\frac{m_{rcj}}{m_c} \right]^{3/2}$ factor takes into account that some transitions are more probable than others. However, it has only a minor role in the PL line shape (unless $\xi_j = 0$). Therefore, the relative strengths of the PL lines associated with different valence subbands are mainly dependent on the distribution of holes among the valence subbands. As an example, consider the situation where the summation in equation 4.4.13 is over the transitions from the conduction band c to the $v1$ valence subband ($j = 1$) and the $v2$ valence subband ($j = 2$) in n-GaAs. When $\Delta_2 = \Delta_1 = 0$ and $\mu_2 = \mu_1$, n_2 is ~10 times n_1 and the line associated with $c-v2$ transitions is ~100 times stronger than the $c-v1$ line (see figure 4.4.6). In contrast, when $\Delta_2 - \Delta_1 = 61meV$ and $\mu_2 = \mu_1$, the reverse is true, n_1 is ~10 times n_2 and the $c-v1$ line is ~1000 times stronger than the $c-v2$ line (see figure 4.4.7). If $\Delta_2 - \Delta_1 = 61meV$ and the quasi-Fermi levels for the $v1$ and $v2$ valence subbands are unequal ($\mu_2 \neq \mu_1$), there is good agreement between the line shape given by equation 4.4.13 and the experimental data (see figure 4.4.8). Note that the carrier temperature of the shocked PL spectra (figure 4.4.8) is 40° greater than the carrier temperature of the unshocked PL spectra (figure 4.4.6). However, this is not significant since the error due to fitting is $\pm 40K$.

The nonequal quasi-Fermi levels shown in figure 4.4.6 is very interesting. If the redistribution of the holes among the valence subbands can be characterized by a time constant τ_v and the decay of the holes by a time constant τ_{eff} (see for exam-

ple equation 4.5.10), it is expected that for $\tau_v \ll \tau_{eff}$, $\mu_2 = \mu_1$ (and conversely, for $\tau_v \gg \tau_{eff}$, $\mu_2 \neq \mu_1$). There has been experiments[114] which show that the holes thermalized within $11ps$. Other experiments (see figure 4.5.12) indicate that $\tau_{eff} \sim 200ps$ ($\gg \tau_v$). Consequently, it is expected that $\mu_2 = \mu_1$ (and that line shape shown in figure 4.4.7 will be observed). However, the line shape shown in figure 4.4.8 is observed. This suggest that τ_v is different for dynamic compression (as compare to static compression) of GaAs.

Another interesting feature seen in figure 4.4.4 is the increase in the observed PL intensity from the shock compressed GaAs as compared to the unshocked GaAs. This has also been observed in the shock compression experiments on CdSe. This will be discussed further in chapter 5 (p. 136).

In summary, the longitudinal stress component and the transverse stress component are unequal for shock propagation along the [001] direction of bulk n-GaAs. From the shifts and splittings in the PL from GaAs, the longitudinal and transverse components can be determined. The longitudinal stress component can be written as the sum of hydrostatic pressure plus a uniaxial stress. The uniaxial stress increases to a maximum of ~$9kbar$ then decreases.

4.5 Gallium Arsenide Under Static Stress

The next experiment on n-GaAs study the hole dynamics under static uniaxial stress. The hole lifetimes are expected to change with stress (see section 2.1). By observing the time resolved PL from static uniaxially compressed n-GaAs, the stress dependence of the hole lifetimes can be measured. The same theoretical formulation described in section 4.4 for the shock compressed GaAs can be used for the static uniaxial compressed GaAs by setting $P = 0kbar$. A new experimental setup is needed for the static uniaxial compression experiment and is described in the next section.

4.5A Experimental Method for Static Uniaxial Compression

In a ring cavity dye laser, a $120mm$ thick Ethylene Glycol jet containing $1.6\times10^{-3}M$ of Rhodamine 590 is pumped by the $514.5nm$ line of a CW Argon ion laser. By utilizing $6.6\times10^{-5}M$ DODCI in a $60mm$ thick Ethylene Glycol jet as a saturable absorber, this ring cavity dye laser can be mode-locked. Mode-locking occurs when two counter-propagating pulses coincide inside the DODCI dye jet. This type of laser is called a colliding-pulse mode-locked (CPM) dye laser.

In a CPM laser, the temporal width of the pulse is influenced by the group velocity dispersion, the self phase modulation (SPM), the available bandwidth of the oscillator cavity, and the dyes' ability to shape the amplitude of the pulse. There is amplitude shaping of the leading (trailing) edge of the laser pulse by the saturable

absorber (gain) jet. This cause a narrowing of the temporal width with a corresponding broadening of the spectral width of the pulse. The spectral width of the pulse can also be increased (up to the available cavity bandwidth) by focusing the laser pulse in the saturable absorber jet for SPM. However, even with a broad spectral width, group velocity dispersion in the optics and dye jets tends to broaden the temporal width. This group velocity dispersion can be controlled by the incorporation of two pairs of prisms inside the laser cavity. By optimizing the above pulse shaping mechanisms, the pulse can be as short as $27ps$.

In this experiment, $100fs$ $620nm$ pulses from the CPM laser are used to generate the electron hole plasma (EHP) in a n-GaAs sample. The recombination of the photogenerated carriers results in luminescence. The n-type Si doped GaAs sample (with $N_D = 10^{18}cm^{-3}$) is cut into a parallelepiped after alignment by x-ray diffraction and cemented into a pair of brass cups. The brass cups are contained in a stress frame where the upper cup is fixed and the lower cup is movable (see figure 4.5.1). A upward force on the lower cup applies an uniaxial compression to the sample. The needed force is exerted by an elongated spring which is magnified by a lever and transmitted by a pull frame to a pin which exert an upward force onto the brass cup.[115] The stress frame with the pull frame and sample is placed into an optical liquid nitrogen dewar for low temperature experiments. By varying the applied pressure, the pressure dependence of the PL is observed.

The PL from the sample is analyzed with a polarizer and dispersed in energy

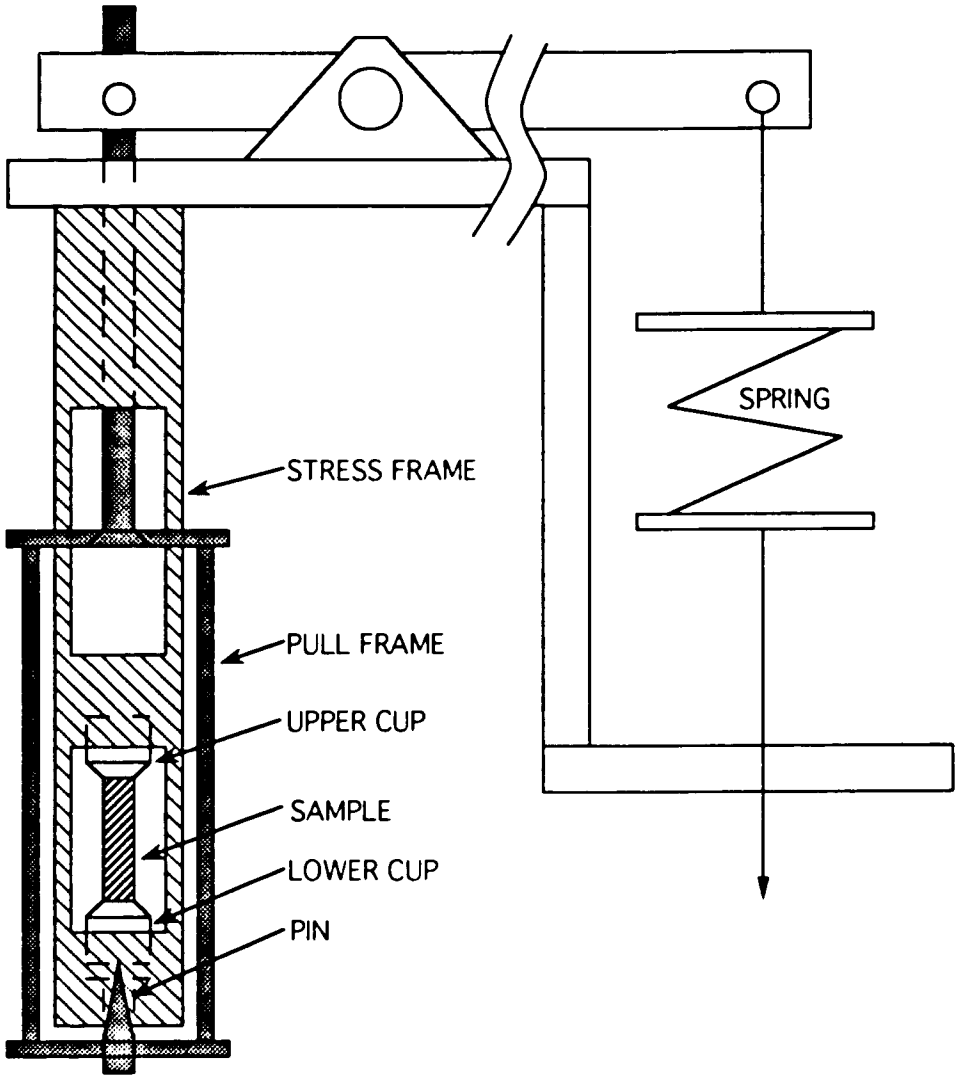

Figure 4.5.1. Schematic diagram of the static uniaxial stress apparatus.

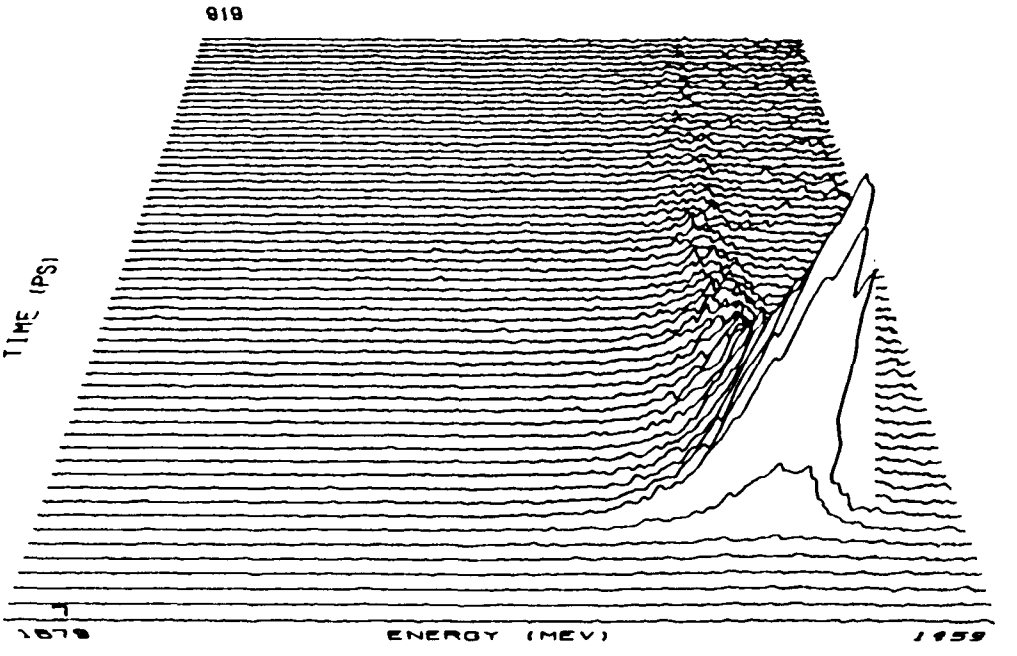

Figure 4.5.2. Energy and time resolved image of the photoluminescence from GaAs.

using a 275*mm* Czerny-Turner spectrograph with a 150 *grooves/mm* grating (Jarrell-Ash). This frequency dispersed spectra is subsequently detected by a streak camera and video camera. In the synchroscan streak camera (Hamamatsu Photonics), the light is converted into photoelectrons by a multi-alkali photocathode and dispersed in time by a pair of deflection plates and reconverted back into photons by a phosphor screen. The output of the streak camera is detected by a SIT camera (Hamamatsu Photonics) which is controlled by a multichannel analyzer (Hamamatsu Photonics). A typical image from the multichannel analyzer is shown in figure 4.5.2. The data is then transferred to a *VAX* 11/780 (Digital Equipment) or Sparc Station 2 (Sun Microsystems) for analysis.

4.5B Unstressed GaAs

A typical time integrated spectra of the unstressed n-GaAs at a sample temperature of 104K is shown in figure 4.5.3. The PL peaks at ~825nm with a FWHM of ~55meV. This wide PL width is due to the $10^{18}cm^{-3}$ doping. The time resolved PL spectra of the unstressed n-GaAs is shown in figure 4.5.4. There are several interesting features displayed in figure 4.5.4. First, the cooling of the hot EHP can be seen in the sharp peak in the 10meV slice centered at 1580meV of the unstressed GaAs PL spectra. Looking at the first 500ps for the 1500meV band in more detail (see figure 4.5.5), it can be seen that the holes cool within the resolution of the experiment (12ps). This is in agreement with previous results.[114]

Another interesting feature displayed in figure 4.5.4 is the nonexponential decay of the PL for different energies. The PL is related to the recombination of the photogenerated electron hole pairs (i.e., $n(t)$ electrons, $p(t)$ holes, with $n(t) = p(t)$). From the detail balance requirement,[116] the relaxation of the carrier densities to the equilibrium carrier distribution (n_i electrons and p_i holes) is given by

$$\frac{dn(t)}{dt} = \frac{dp(t)}{dt} \propto \Big[n_i + n(t) \Big] \Big[p_i + p(t) \Big] - n_i p_i \quad . \tag{4.5.1}$$

Ignoring reabsorption and including Auger type transitions, the decay of the generated excess carriers can be described by[117]

$$\frac{dp(t)}{dt} = - Ap(t) - Bp(t)^2 - Cp(t)^3 \quad , \tag{4.5.2}$$

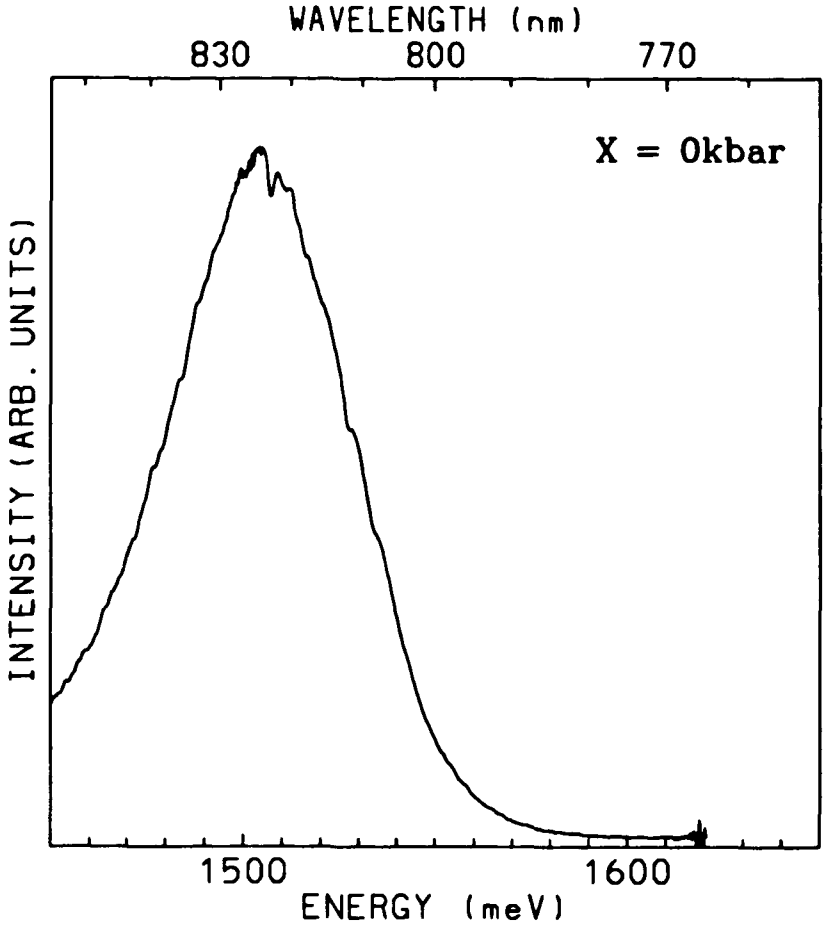

Figure 4.5.3. A plot of the time integrated spontaneous emission spectra from unstressed n-GaAs at $T = 104K$.

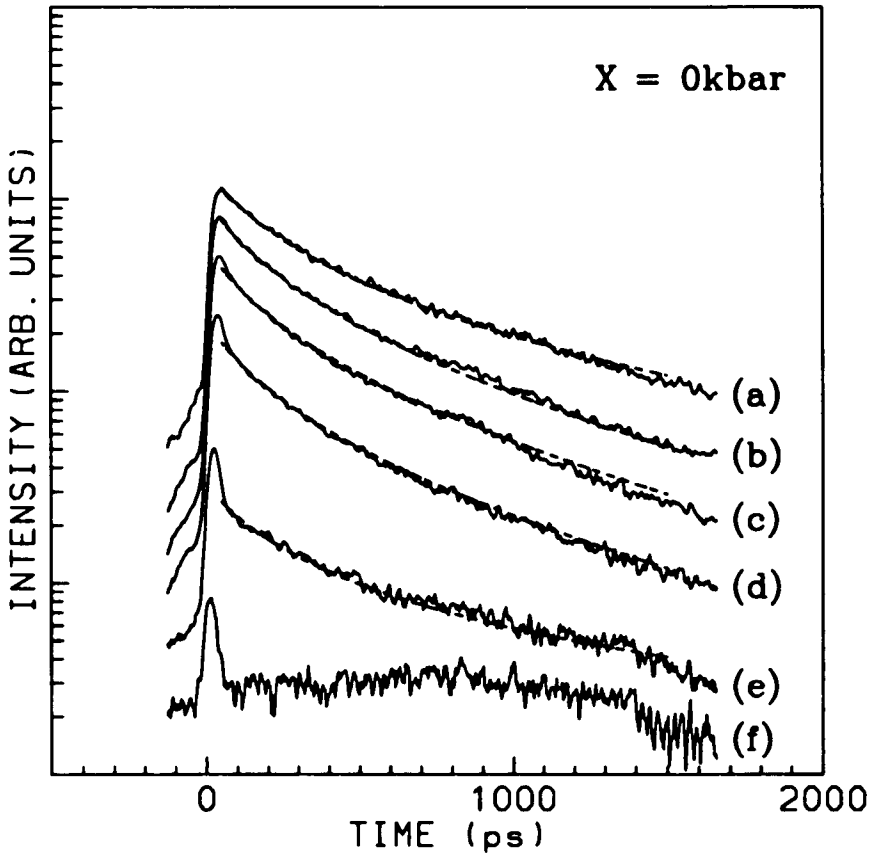

Figure 4.5.4. Plots of the time resolved spectra of unstressed n-GaAs (—) for 10*meV* slices at a) 1480*meV*, b) 1500*meV*, c) 1520*meV*, d) 1540*meV*, e) 1560*meV*, and f) 1580*meV*. The dash lines are the fit to the data using equation 4.5.3 (see text for details).

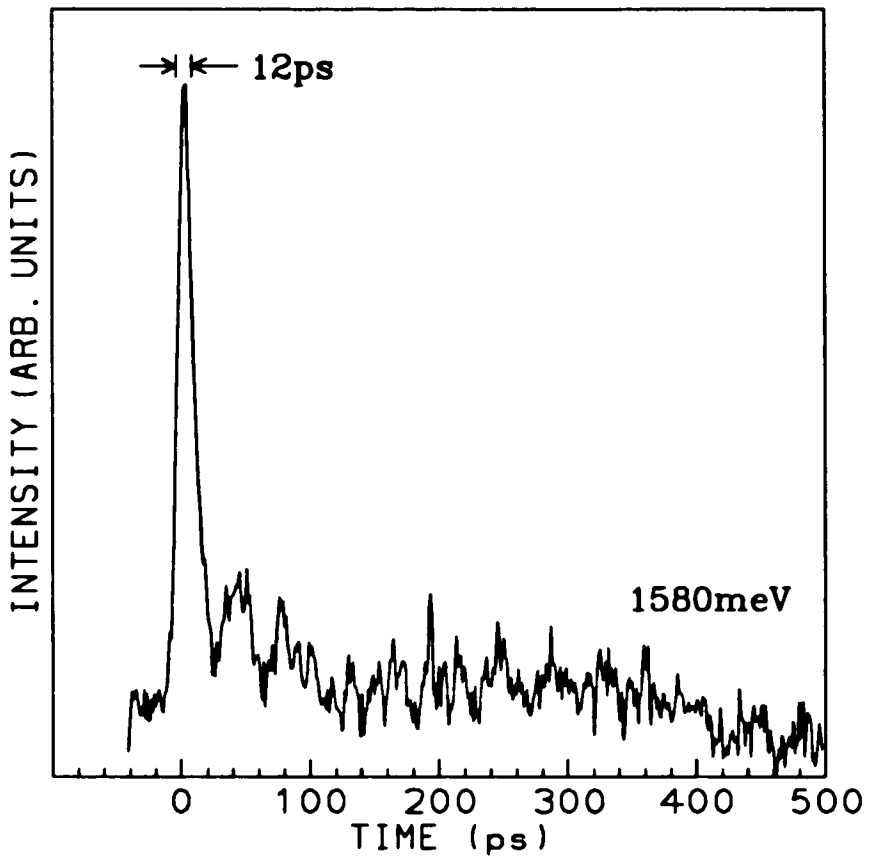

Figure 4.5.5. A plot of the time resolved spectra for a $10meV$ slices at $1580meV$ for the first $500ps$.

where $A \equiv A_r + A_{nr}$, A_r is the radiative recombination coefficient, A_{nr} is the nonradiative recombination coefficient, B is the bimolecular recombination coefficient,[116,118] and C is the recombination coefficient for collisional and phonon assisted Auger transitions.[119] Equation 4.5.2 can be rewritten as

$$\frac{d\bar{p}}{dt} = -A\left[\bar{p} + b_A\bar{p}^2 + c_A\bar{p}^3\right] \quad , \tag{4.5.3}$$

where $b_A \equiv b/A$, $b \equiv BP_o$, $c_A \equiv CP_o^2/A$, and $\bar{p}$ is defined by $p(t) \equiv P_o\bar{p}(t)$. Since,[119] $C \approx 10^{-29}cm^6s^{-1}$ and the photogenerated EHP density is $10^{15}cm^{-3}$, the third term on the right hand side of equation 4.5.3 is negligible compared to the two other terms.

With $C = 0$, the analytic solution to equation 4.5.3 is

$$\bar{p}(t) = \left[(1 + b_A)\,e^{At} - b_A\right]^{-1} \quad . \tag{4.5.4}$$

The constants A and b for various $10meV$ time slices between $1470meV$ to $1540meV$ are determined by least square fitting of the data to equation 4.5.4 (see figure 4.5.4). From the fitting, it is found that $b = 4.6\times10^{-3}ps^{-1}$ is approximately constant over this energy range. The decay constant A is found to vary with energy (see figure 4.5.6). The decay constant A is seen to decrease for energies below $1500meV$, while above $1500meV$ it is almost constant. The energy dependence of the recombination constant A in figure 4.5.6 has the following form,

$$A = A_1 + A_2\left[\frac{h\nu}{\tilde{E}} - 1\right]^{1/2} \quad . \tag{4.5.5}$$

It is interesting to note that energy dependence of the recombination constant A is identical to the energy dependence of the allowed direct transitions.[120] A least square fit using equation 4.5.5 to the data shown in figure 4.5.6 yields values of $A_1 = 2.5\times10^{-4}ps^{-1}$, $A_2 = 4.2\times10^{-3}ps^{-1}$, and $\tilde{E} = 1471meV$.

The temperature dependent direct intrinsic gap of GaAs is given by[121]

$$\varepsilon_i(T) = 1519meV - \frac{(0.5408meV\,K^{-1})\,T^2}{T + 204K} \quad . \tag{4.5.6}$$

The band gap is $\varepsilon_i(T = 104K) = 1500meV$. Of course, since the experimental sample is 10^{18} Si doped n-GaAs, the band gap is expected to be slightly smaller[122] than given by equation 4.5.6. It can be seen that the fitted value for the effective band gap is quite reasonable.

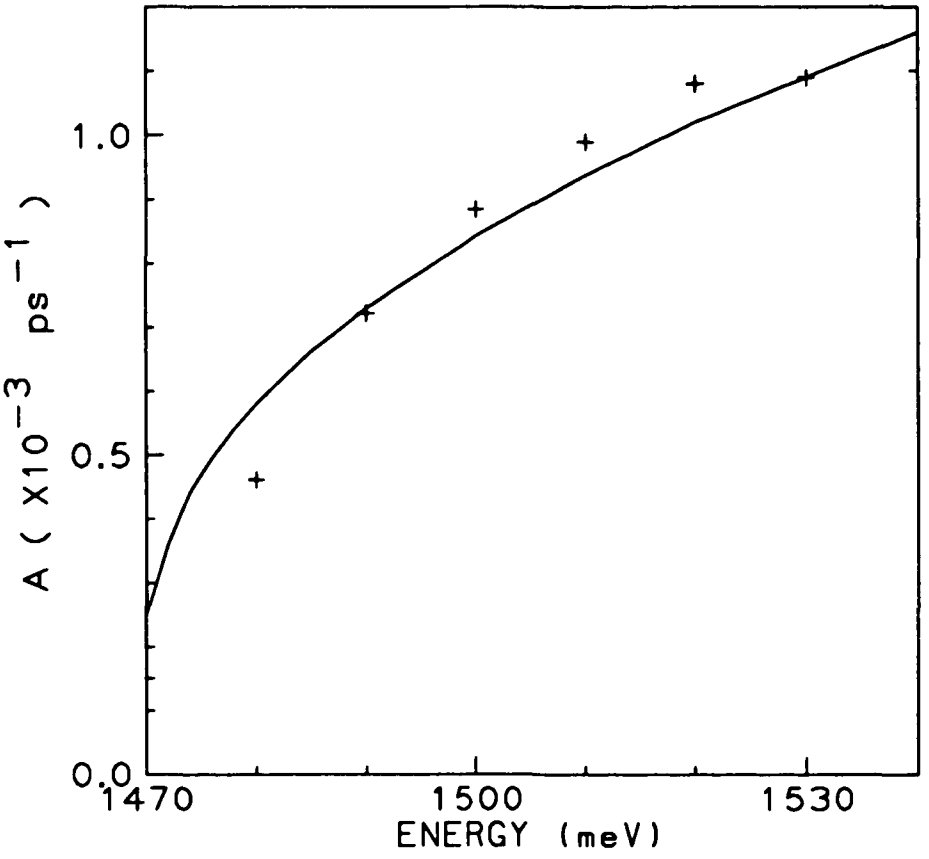

Figure 4.5.6. A plot of the decay constant A (+) as a function of the transition energy. The solid line is the fit from equation 4.5.5.

4.5C Stressed GaAs (Energy Domain)

Under uniaxial stress, the four-fold degenerate valence subband of GaAs is split into two spin degenerate bands (v_1 and v_2 bands) as shown in figure 4.4.1b. The shifts of the GaAs band edges under uniaxial stress have been well established by modulation spectroscopy.[123] The shifts of the valence band edges relative to the conduction band edge under static uniaxial stress (see for example Appendix A2) are[110]

$$\Delta E_{c-v1}(X) = \delta E_{II} - \frac{\delta E_{001}}{2} - \frac{\delta E_{001}^2}{2\Delta_o} + \ldots , \tag{4.5.7a}$$

$$\Delta E_{c-v2}(X) = \delta E_{II} + \frac{\delta E_{001}}{2} , \tag{4.5.7b}$$

and

$$\Delta E_{c-v3}(X) = \delta E_{II} + \frac{\delta E_{001}^2}{2\Delta_o} + \ldots , \tag{4.5.7c}$$

where[111] $\delta E_{II} \equiv (a_c^z + a_1^z)(S_{11}^z + 2S_{12}^z)X$, $\delta E_{001} \equiv 2b_1^z(S_{11}^z - S_{12}^z)X$, $a_c^z + a_1^z = 8720meV$, $b_1^z = 2000meV$, $S_{11}^z = 1.2\times10^{-3}kbar^{-1}$ and $S_{12}^z = -0.4\times10^{-3}kbar^{-1}$ are the GaAs elastic constants,[108] and X is the compressive uniaxial stress. The energy shifts according to equation 4.5.7, are plotted in figure 4.5.7. Note that this is identical to equation 4.4.11. This is to be expected since for $P = 0kbar$, the stress vector for shock compression (4.3.4) is identical to the stress vector for uniaxial stress (2.2.11). The shift of the $c-v_1$ transitional energy is only a few meV up to a stress of $10kbar$, whereas the shifts of both the $c-v_2$ and $c-v_3$ transitional energies increase monotonically with compressive stress.

The matrix elements for [001] uniaxially stressed GaAs have also been calculated.[115,123] With stress, the matrix elements $| < c | \hat{\mathbf{e}} \cdot \mathbf{p} | v > |^2$ (see Appendix A3) for different polarization relative to the [001] stress axis (to first order in $\frac{\delta E_{001}}{\Delta_o}$) are proportional to

$$\begin{array}{lcc} & \parallel & \perp \\ v_1 & 4\left[1 + \frac{\delta E_{001}}{\Delta_o}\right] & \left[1 - \frac{2\delta E_{001}}{\Delta_o}\right] \\ v_2 & 0 & 3 \\ v_3 & 2\left[1 - \frac{2\delta E_{001}}{\Delta_o}\right] & 2\left[1 + \frac{\delta E_{001}}{\Delta_o}\right] \end{array} \quad . \tag{4.5.8}$$

Neglecting the c-v3 transitions, this implies that the luminescence polarized parallel to the stress axis is composed of only c-v1 transitions. The luminescence polarized perpendicular to the stress axis is a mixture composed of both c-v1 and c-v2 transitions. Therefore, a comparison of the parallel and perpendicular polarized PL will give information about the c-v2 transition.

By applying stress to the n-GaAs sample, the c-v1 and c-v2 transitional energies will vary according to equations 4.5.7a and 4.5.7b, respectively. The time integrated spectra for PL polarized parallel and perpendicular to the [001] stress axis are plotted in figure 4.5.8a to 4.5.8e (for stress $X = 1kbar$ to $5kbar$, respectively). From figure 4.5.8, it can be seen that the c-v1 transition (i.e., the PL polarized parallel to the stress axis) shifts according to equation 4.5.7a. The c-v2

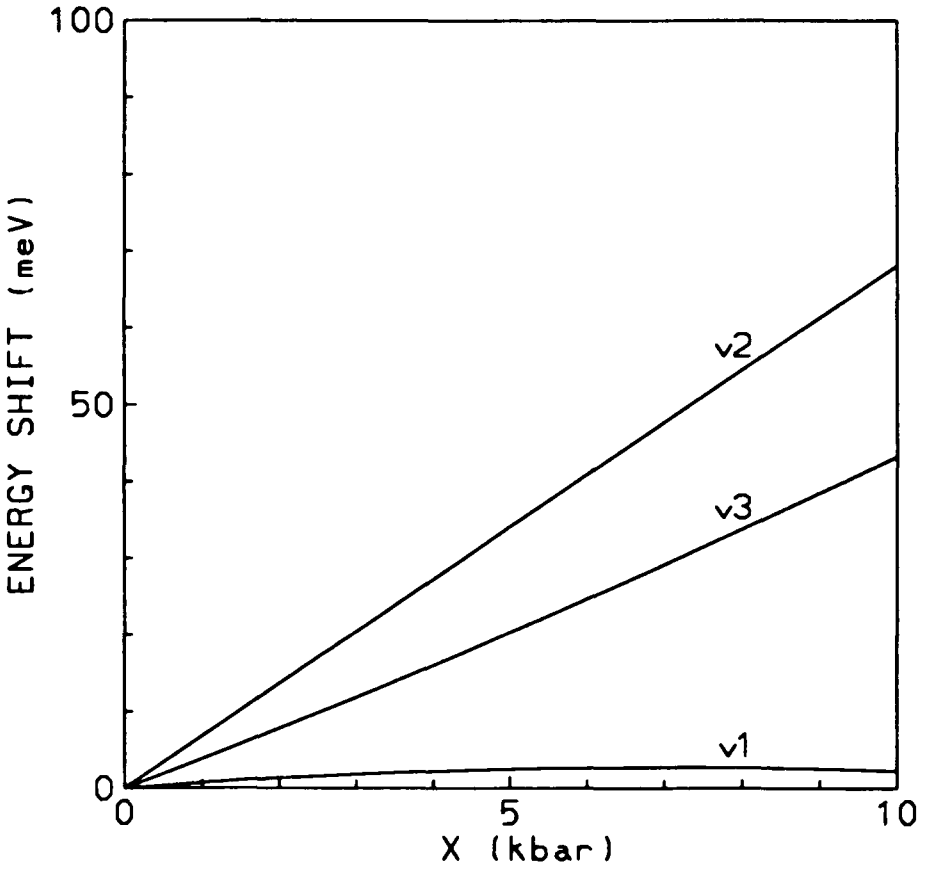

Figure 4.5.7. The shifts of the $v1$, $v2$, and $v3$ valence subband edges relative to the conduction band edge as a function of [001] uniaxial stress.

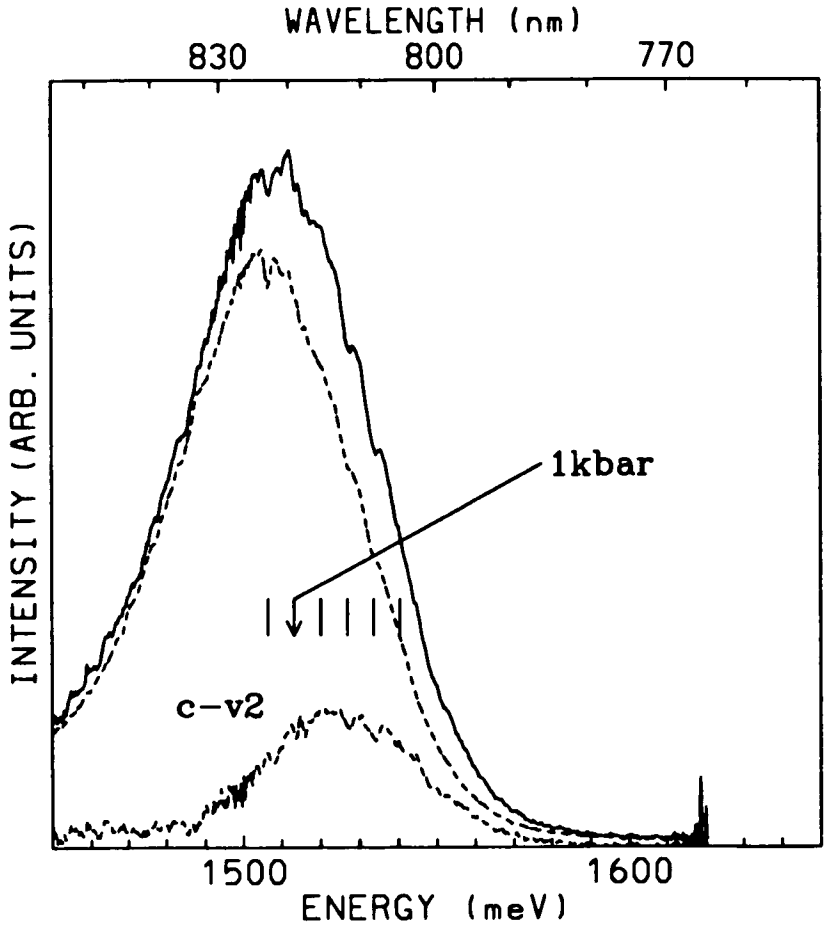

Figure 4.5.8a. A plot of the time integrated spontaneous emission spectra polarized $\parallel$ (---) and $\perp$ (—) to the [001] stress axis from n-GaAs at $T = 104K$ for $X = 1kbar$. The difference between the PL polarized parallel and perpendicular to the stress axis gives the contribution to the PL from the c-v2 transitions (see text). As a guide, the expected shifts of the c-v2 PL as a function of stress are plotted as tics.

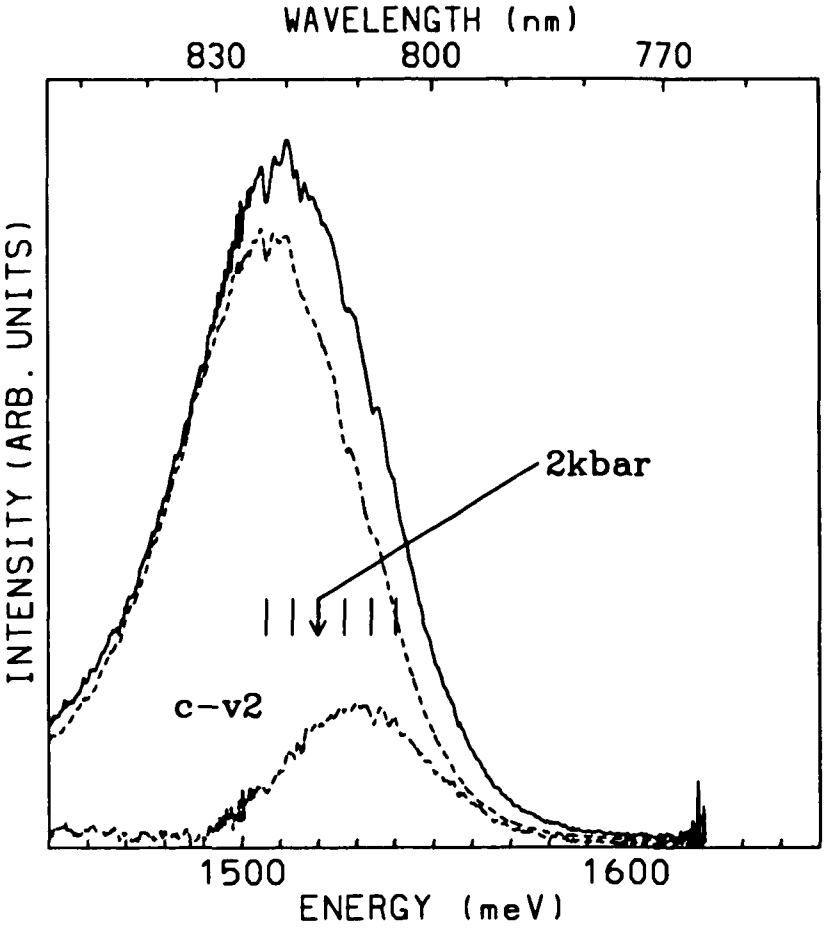

Figure 4.5.8b. A plot of the time integrated spontaneous emission spectra polarized $\parallel$ (---) and $\perp$ (—) to the [001] stress axis from n-GaAs at $T = 104K$ for $X = 2kbar$. The difference between the PL polarized parallel and perpendicular to the stress axis gives the contribution to the PL from the c-v2 transitions (see text). As a guide, the expected shifts of the c-v2 PL as a function of stress are plotted as tics.

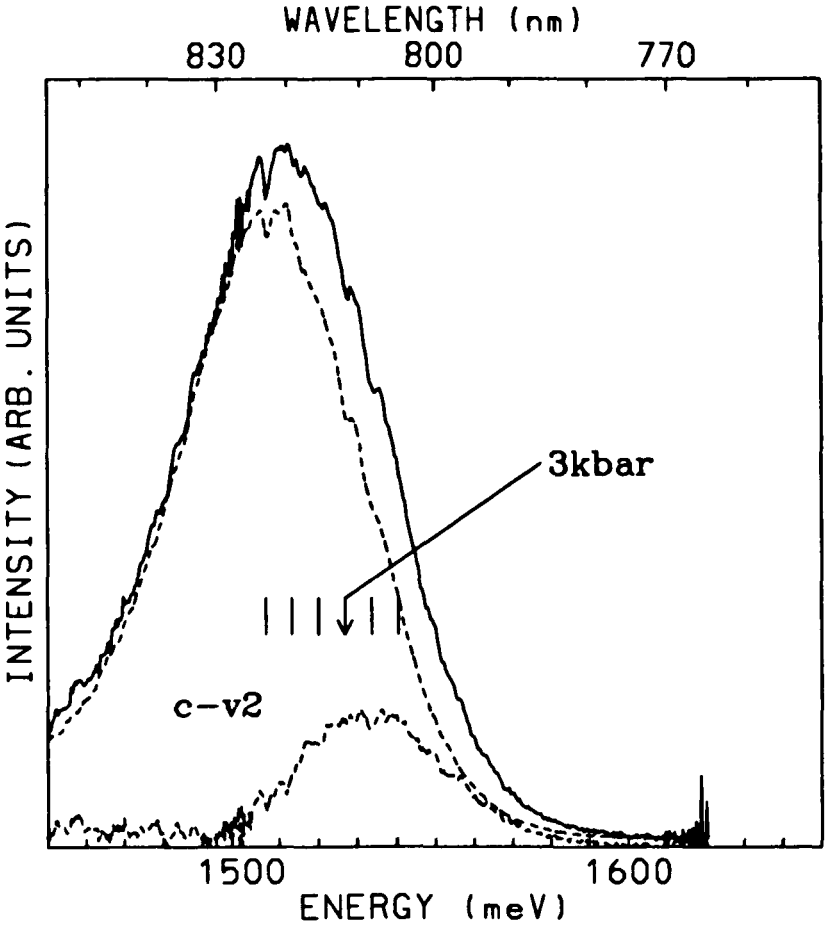

Figure 4.5.8c. A plot of the time integrated spontaneous emission spectra polarized $\parallel$ (---) and $\perp$ (—) to the [001] stress axis from n-GaAs at $T = 104K$ for $X = 3kbar$. The difference between the PL polarized parallel and perpendicular to the stress axis gives the contribution to the PL from the c-v2 transitions (see text). As a guide, the expected shifts of the c-v2 PL as a function of stress are plotted as tics.

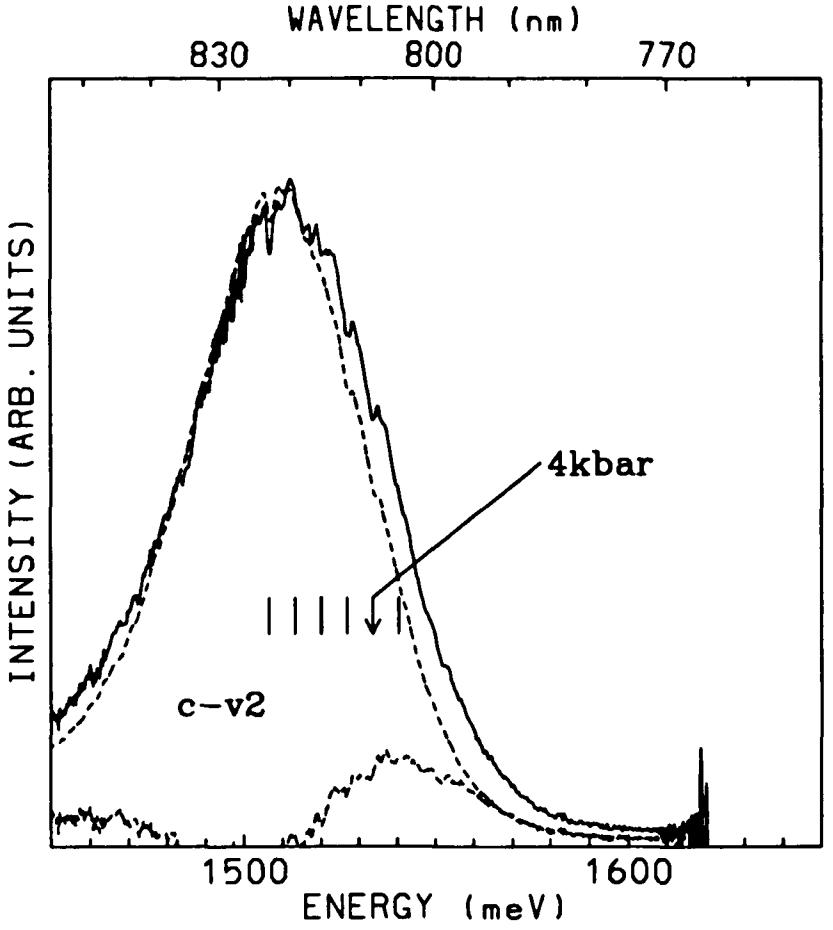

Figure 4.5.8d. A plot of the time integrated spontaneous emission spectra polarized $\parallel$ (---) and $\perp$ (—) to the [001] stress axis from n-GaAs at $T = 104K$ for $X = 4kbar$. The difference between the PL polarized parallel and perpendicular to the stress axis gives the contribution to the PL from the c-v2 transitions (see text). As a guide, the expected shifts of the c-v2 PL as a function of stress are plotted as tics.

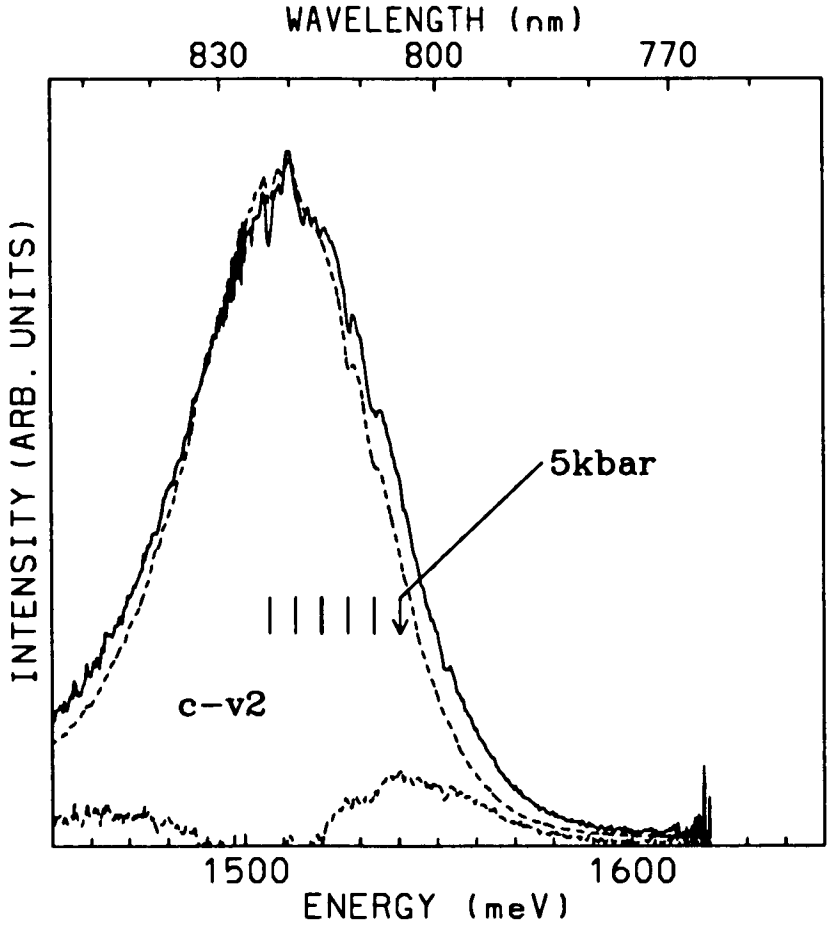

Figure 4.5.8e. A plot of the time integrated spontaneous emission spectra polarized $\parallel$ (---) and $\perp$ (—) to the [001] stress axis from n-GaAs at $T = 104K$ for $X = 5kbar$. The difference between the PL polarized parallel and perpendicular to the stress axis gives the contribution to the PL from the c-v2 transitions (see text). As a guide, the expected shifts of the c-v2 PL as a function of stress are plotted as tics.

transitions can be extracted, as noted above, by subtracting the parallel PL spectrum from the perpendicular PL spectrum. As a check, the sum of the parallel and perpendicular PL spectra agree quite well with the unpolarized spectra. The c-v2 PL for various compressive stress are plotted in figure 4.5.8. The width of the c-v2 PL ($\sim 40meV$) is found to be slightly narrower then the c-v1 PL. From equation 4.5.7b, the blue shifts for $X = 1kbar$ to $5kbar$ relative to $X = 0kbar$ are also plotted as tics above the c-v2 profiles in figure 4.5.8. Note, these ticks have been shifted to point to the peak positions and not the band gaps. From figure 4.5.8, the c-v2 PL can be seen to blue shift in agreement with equation 4.5.7b.

4.5D Stressed GaAs (Time Domain)

The stress dependence of the changes in the gain of semiconductor lasers has been studied in relation to changes in the effective mass of the holes.[124] The stress dependence of the absorption coefficient has been calculated[125] using an effective mass that is linearly dependent on the stress ($m_{\alpha\,\beta} = m_\alpha + m_\alpha[\delta_\alpha^\beta]X$, for $\alpha = v1$ or c and $\beta = \parallel$ or $\perp$). The absorption coefficient as a function of stress (see Appendix A5) is given by

$$\Delta\alpha(h\nu, X) = \left[\frac{\Delta_1(X)}{\Delta^o}\right]^{1/2} \left[\frac{\mu_\perp(X)}{\mu_o}\right]^{3/2} \frac{u}{2} \int_0^1 dz \frac{1 + (4u - 1)\, z^2}{1 + (u - 1)\, z^2} \quad , \quad (4.5.9)$$

where $\Delta_1(X) \equiv \Delta^o - \Delta E_{c-v1}(X)$, $\Delta^o \equiv h\nu - E_g$, $\mu_o^{-1} \equiv m_c^{-1} + m_1^{-1}$, $u = \dfrac{\mu_\parallel(X)}{\mu_\perp(X)}$, $\mu_\parallel(X)^{-1} \equiv m_{c\,\parallel}(X)^{-1} + m_{1\,\parallel}(X)^{-1}$, $\mu_\perp(X)^{-1} \equiv m_{c\,\perp}(X)^{-1} + m_{1\,\perp}(X)^{-1}$, m_c is the conduction band effective mass, and m_1 is the v1 valence band effective mass. It can be seen that for $\delta_\alpha^\parallel > 0$ and $\delta_\alpha^\perp < 0$, the absorption increases monotonically with stress. The increase in the absorption coefficient causes the penetration depth of the incident laser pulse to decrease. Therefore, assuming all other factors are constant, the same number of carriers is generated but in a smaller volume. This implies an increase in the photogenerated carrier density as a function of stress. Since the PL photon flux at initial time[116] is proportional to P_o^2, by taking the square root of the number of photons detected at initial time, P_o can be determined. The ratios $\Delta P_o(X) \equiv P_o(X)/P_o(X = 0kbar)$ are plotted as crosses in figure 4.5.10. This increase of ~50% for P_o for a stress of $X = 5kbar$ can be attributed to the change

in the absorption coefficient as a function of stress. To compare the experimental data with equation 4.5.9, a few constants are needed. For GaAs, the effective masses are[126] $m_c = 0.066$ and $m_1 = 0.082$. For an applied stress of $X = 0kbar$ to $5kbar$, $\frac{\Delta_1(X)}{\Delta^o} \approx 1$. Since δ_c^β and δ_{v1}^β (for $\beta = \parallel$ and $\perp$) have the same order of magnitude and sign, by using $\delta_c^{\parallel} = \delta_{v1}^{\parallel} = \delta_{\parallel} = 0.11 kbar^{-1}$ and $\delta_c^{\perp} = \delta_{v1}^{\perp} = \delta_{\perp} = -0.09 kbar^{-1}$, there is good agreement with the experimental data (see figure 4.5.10).

The time resolved spectra of stressed n-GaAs is qualitatively similar to the unstressed n-GaAs (see figures 4.5.9 and 4.5.4). By fitting a $40meV$ slice of the c-v1 PL (i.e., the PL polarized parallel to the stress axis) to equation 4.5.4, the change of the decay constants b and A as a function of stress can be determined (see figures 4.5.10 and 4.5.11). Also plotted as a solid line in figure 4.5.11, is the change in the matrix element as a function of stress (equation 4.5.8). It can be seen that the variation of A with stress can be attributed mostly to the stress dependence of the matrix elements. The decay constant b which is plotted in figure 4.5.10 also shows a strong stress dependence. It appears that the stress dependence of b is the same as the stress dependence of P_o. From this one may conclude that the stress dependence of $b = BP_o$ is due entirely to the stress dependence of P_o and that the bimolecular recombination coefficient B is essentially independent of stress. From the experimentally determined value of the recombination constant b at $X = 0kbar$ ($b_o = 5\times10^{-3} ps^{-1}$) and a carrier density of $10^{15} cm^{-3}$, the bimolecular recombination

coefficient for this experiment is $B = b/P_o = 5\times10^{-6}cm^3s^{-1}$. This is different than the reported[127] values of $B = 5\times10^{-8}cm^3s^{-1}$ to $B = 5\times10^{-10}cm^3s^{-1}$. This difference can be attributed to surface recombination and a nonuniform photogenerated carrier density which have a strong influence on the bimolecular recombination coefficient.[128]

Since the decay of the PL is nonexponential, the lifetime of the hole is time dependent.[116] However, an effective lifetime can be defined as the time for the photogenerated carriers to decrease to e^{-1} of its initial value. The effective lifetime[117] can be obtained from equation 4.5.4, by solving $e^{-1} = \bar{p}(\tau_{eff})$ for τ_{eff} (see Appendix A6). This yields

$$\tau_{eff} = \frac{1}{A} \ln\left[\frac{Ae + b}{A + b}\right] , \qquad (4.5.10a)$$

where $e = 2.71828$. Since $A(X) \equiv A_o\Delta A(X)$ and $b(X) \equiv b_o\Delta b(X)$, this expression can be rewritten as

$$\tau_{eff} = \frac{1}{A_o\Delta A(X)} \ln\left[\frac{A_o\Delta A(X)\, e + b_o\Delta b(X)}{A_o\Delta A(X) + b_o\Delta b(X)}\right] . \qquad (4.5.10b)$$

Using the experimental values of $A_o = 9\times10^{-4}ps^{-1}$, $b_o = 5\times10^{-3}ps^{-1}$, and the $\Delta A(X)$ and $\Delta b(X)$ shown in figures 4.5.11 and 4.5.10, respectively, the effective lifetime of the v1 holes as a function of stress is plotted in figure 4.5.12. It can be seen that there is a $70ps$ decrease of the v1 hole effective lifetimes as the stress on the n-GaAs is increased from $X = 0kbar$ to $X = 5kbar$.

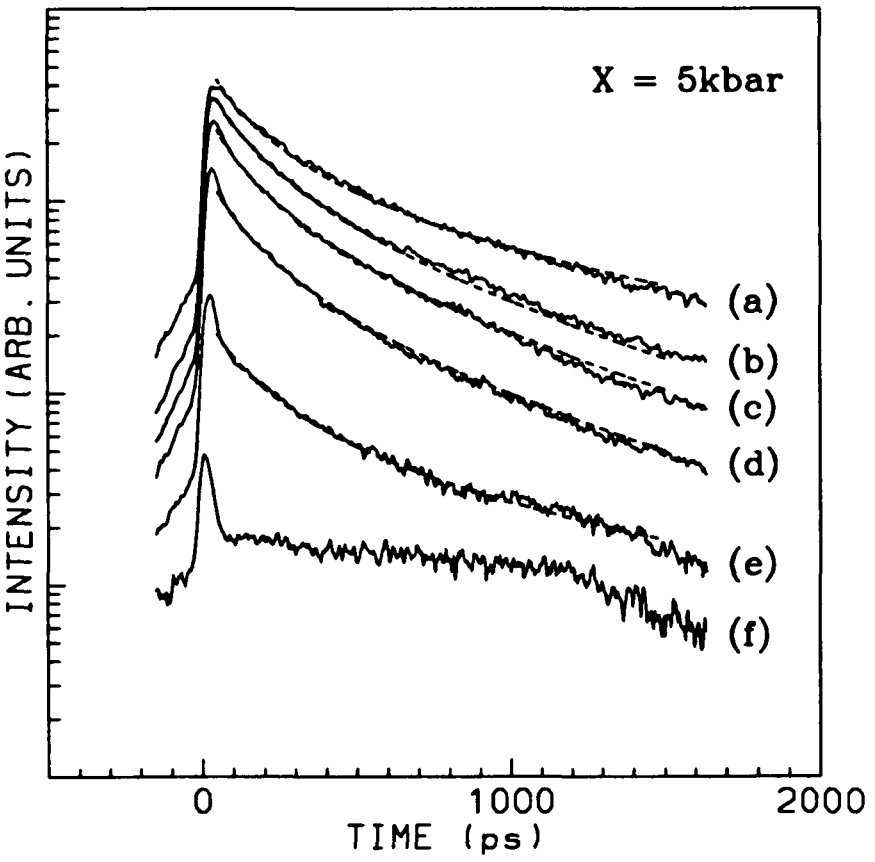

Figure 4.5.9. Plots of the time resolved spectra of stressed (X = 5*kbar*) n-GaAs (—) for 10*meV* slices at a) 1480*meV*, b) 1500*meV*, c) 1520*meV*, d) 1540*meV*, e) 1560*meV*, and f) 1580*meV*. The dash lines are the fit to the data using equation 4.5.3 (see text for details).

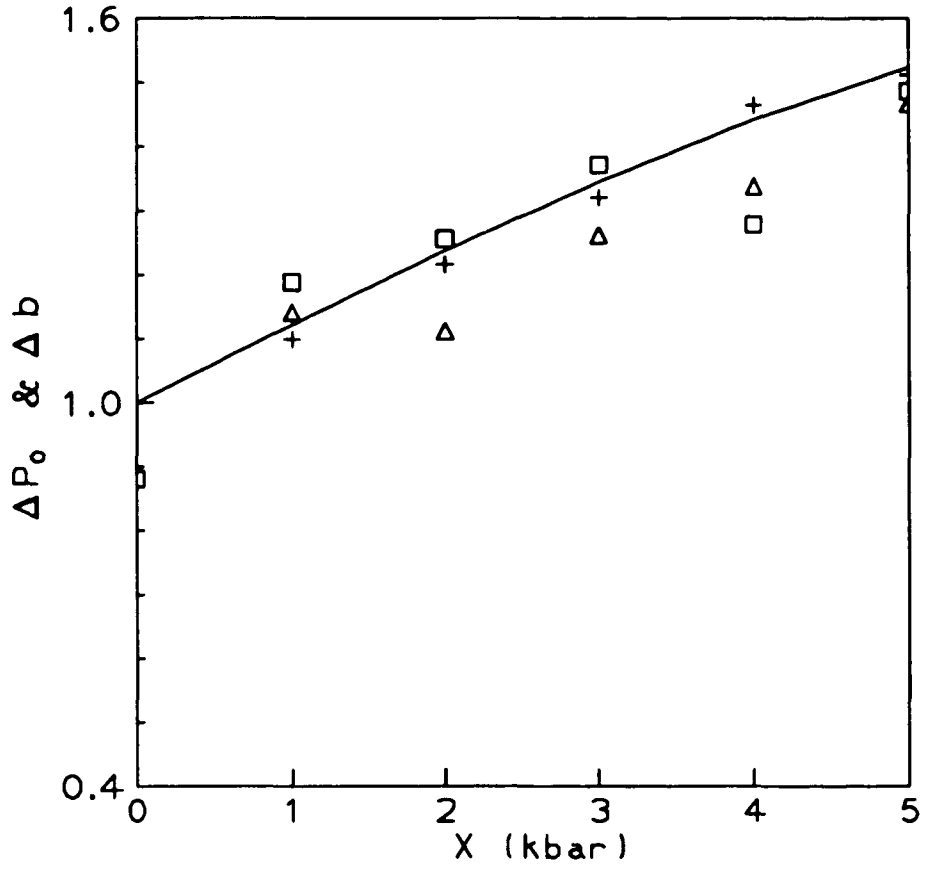

Figure 4.5.10. A plot of the change in P_o (+) together with the change in decay constant b (□ and Δ) as a function of stress X. The solid line plotted is the theoretical prediction from equation 4.5.9 (see text).

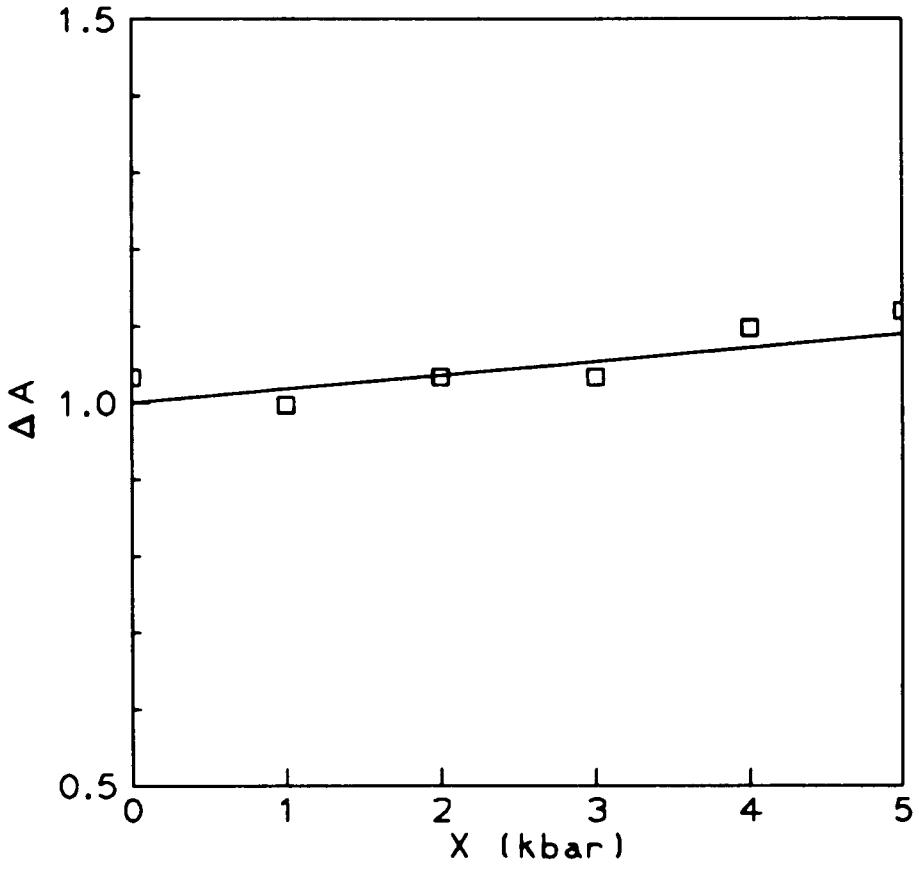

Figure 4.5.11. A plot of the change in the decay constant A (□) as a function of stress X. The solid line is the change in the matrix element as given by equation 4.5.8.

Turning our attention to the c-v2 transitions, from figure 4.5.8 it can be seen that the c-v2 PL is not clearly separated from the c-v1 PL and is also much weaker than the c-v1 transition. The c-v2 time resolved PL can be obtained from the difference of the parallel and perpendicular PL (as described in section 4.5c). The stress dependence of the lifetimes of the v2 holes can be extracted using this approach. However, this means that the accuracy is not as good as for the c-v1 transitions. Looking just at the time resolved spectra of the c-v2 transitions for $X = 5kbar$ (extracted from the data shown in figure 4.5.8e), the PL from the c-v2 transitions has the same qualitative features as the PL from the c-v1 transitions (see figure 4.5.13). Using equation 4.5.4, the bimolecular recombination coefficient ($B = 5\times10^{-6}cm^3s^{-1}$) for the c-v2 PL (see figure 4.5.13) is the same as for the c-v1 transition at $X = 5kbar$. The c-v2 decay constant is $A \approx 8.4\times10^{-4}ps^{-1}$, in contrast with the observed $A \approx 10.\times10^{-4}ps^{-1}$ for the c-v1 transition at $X = 5kbar$. From equation 4.5.10a, this yields only a difference of $8ps$ between the effective lifetimes (τ_{eff}) of the c-v1 holes and the c-v2 holes. Therefore within the experimental accuracy, the decay times of the c-v2 transitions and the c-v1 transitions are almost the same. This is to be expected, since the holes are thermalized among the v1 and v2 valence bands within $11ps$.[114]

In summary, three major strain effects have been observed in the hole dynamics of n-GaAs. The transitions involving the v1 and v2 valence bands have been seen to blue shift. The stress dependence of the effective mass causes an enhancement of the absorption coefficient, which shows as an increase in the density of the

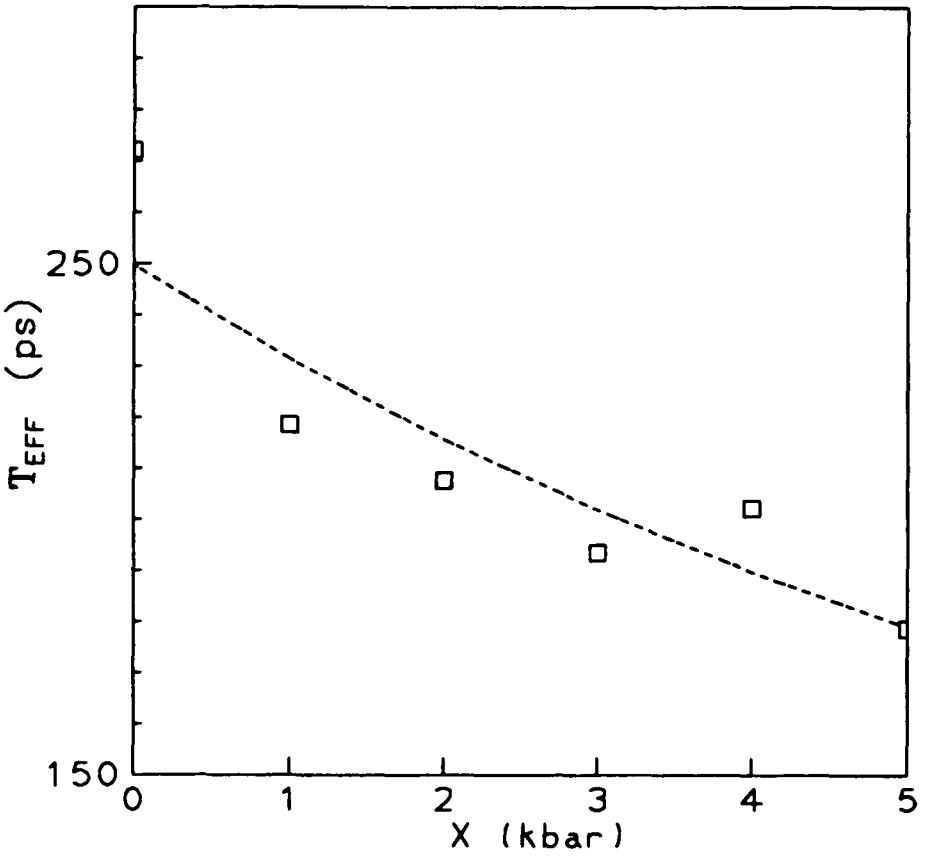

Figure 4.5.12. A plot of the effective lifetimes of the v1 holes (□) as function of stress X. The dash line is plotted as a guide.

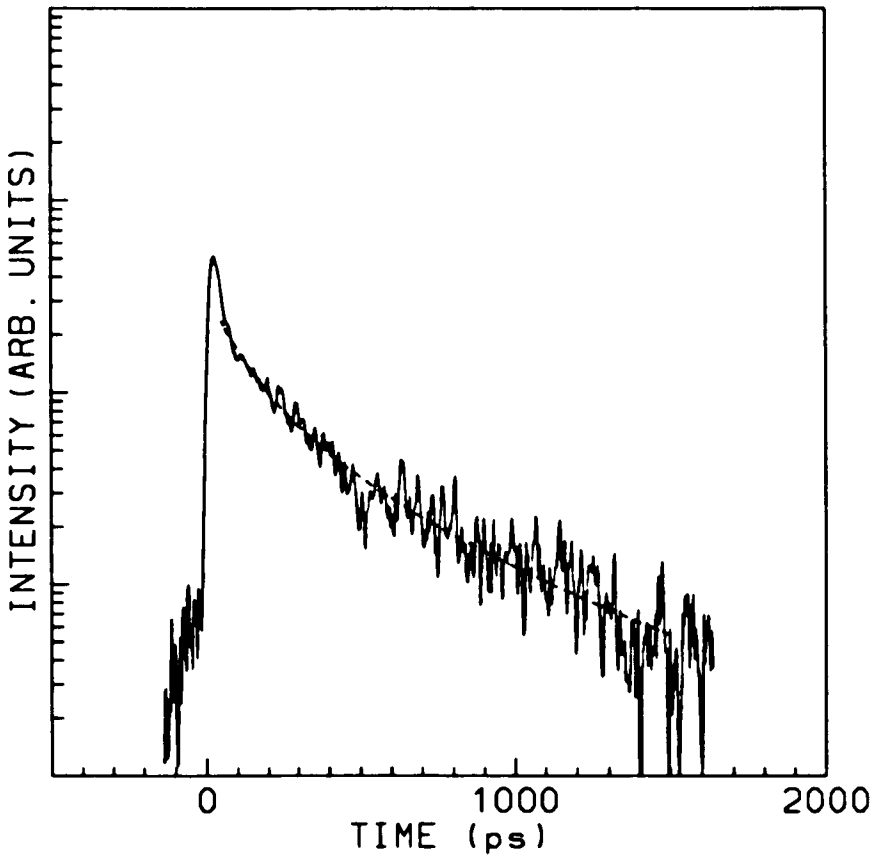

Figure 4.5.13. A plot of the time resolved spectra (—) for a 40*meV* slice at 1555*meV* of the c-v2 PL from X = 5*kbar* uniaxially stressed n-GaAs together with the fit (---).

photogenerated carriers. The time resolved PL spectra from n-GaAs is found to be nonexponential. The decay constant B is independent of stress, while the stress dependence of the decay constant A is in agreement with the stress dependence of the matrix elements. It is found that the effective lifetimes of the v1 holes decrease as a function of stress.

4.6 Gallium Arsenide Quantum Well

The fourth shock compression experiment is on a $5nm$ GaAs quantum well. For the GaAs quantum well, the $30mJ$ pump pulse is focused to a $1250\mu m$ diameter spot on the aluminum foil. The $400nJ$ probe pulse which is collinear and counter-propagating relative to the pump pulse is focused to a $750\mu m$ diameter spot on the front surface of the sample. Data are recorded with the sample held at $T = 80K$. A representative spectra of the PL from the unshocked and the shocked GaAs quantum well is shown in figure 4.6.2. In this figure, there are two emission lines in both the unshocked and shocked PL spectra. In the unshocked spectra, there is a strong line centered at $\sim 1645meV$ with a FWHM of $\sim 35meV$ and a very weak line at $\sim 1695meV$. In the same figure, the shocked spectra shows the same strong line blue shifted to $\sim 1660meV$ with a FWHM of $\sim 40meV$ and the very weak line is blue shifted to $\sim 1703meV$.

For an unstressed $5nm$ GaAs quantum well, the valence (and conduction) bands are quantized by the confining well potential (see figure 4.6.1). The lowest transition band is at $1647meV$ and is denoted the c-hh1 transition.[129] The next higher transition is at $1703meV$ and is denoted the c-lh1 transition. Examining the unshock spectrum displayed in figure 4.6.2, the c-hh1 transition is readily observable, whereas, the c-lh1 transition is bearly observable in the noise of the spectrum. The unshock spectrum has a blue shift of $\Delta_{c-hh1} \approx 15meV$ for the c-hh1 transition. It is difficult to observe the c-lh1 transition, but there appears to be a blue shift of

$\Delta_{c-lh1} \approx 8meV$ under shock compression.

The same type of analysis as described in section 4.4 can be used for the shocked GaAs quantum well (see figure 4.6.2). It has also been shown[130,131] that the stress dependence of the energy shift of the c-hh1 transition is identical to c-v2 transitions in bulk GaAs for $X < 5kbar$ along the growth direction. For the c-lh1 transition, the stress dependence of the energy shifts is qualitatively the same but is approximately 10% greater than the bulk situation. Neglecting this 10% difference between the bulk and the $5nm$ quantum well, the energy separation between the c-hh1 and the c-lh1 transitions (Δ_{h1l1}) is plotted in figure 4.6.3. Note that Δ_{h1l1} decreases as a function of X. The lowest transition c-hh1 has a larger blue shift (as a function of X) as compared with the blue shift of the next higher transition c-lh1. Consequently, as X increases, the energy separation between the c-hh1 and the c-lh1 transitions decreases. Looking at the shock compression data for the GaAs quantum well (see figure 4.6.2), there is a blue shift of $\Delta_{c-hh1} \approx 15meV$ and $\Delta_{c-lh1} \approx 8meV$ for the c-hh1 and c-lh1 transitions, respectively. The difference between the blue shift of the c-hh1 and c-lh1 transitions gives the change in the separation between the c-hh1 and c-lh1 transitions (i.e., $\Delta_{c-lh1} - \Delta_{c-hh1} = 8meV - 15meV = -7meV$). Therefore, the separation between the c-hh1 and c-lh1 transitions under shock compression becomes $\Delta_{h1l1}(X) = \Delta_{h1l1}(X = 0kbar) + (-7meV) = 56meV - 7meV = 49meV$. From figure 4.6.3, $\Delta_{h1l1}(X) = 49meV$ corresponds to $X \approx 1kbar$. This implies that there is $\sim 1kbar$ difference between the longitudinal and transverse components of the shock wave.

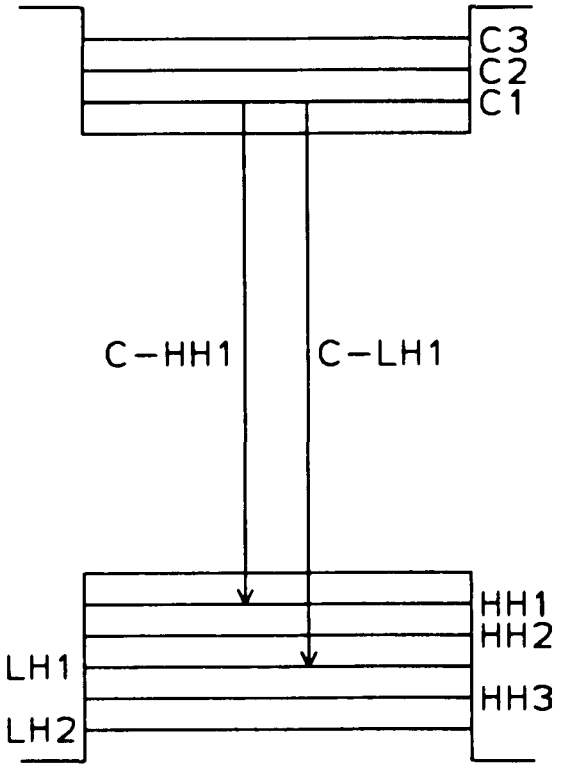

Figure 4.6.1. Schematic diagram of the energy levels in a *5nm* GaAs quantum well.

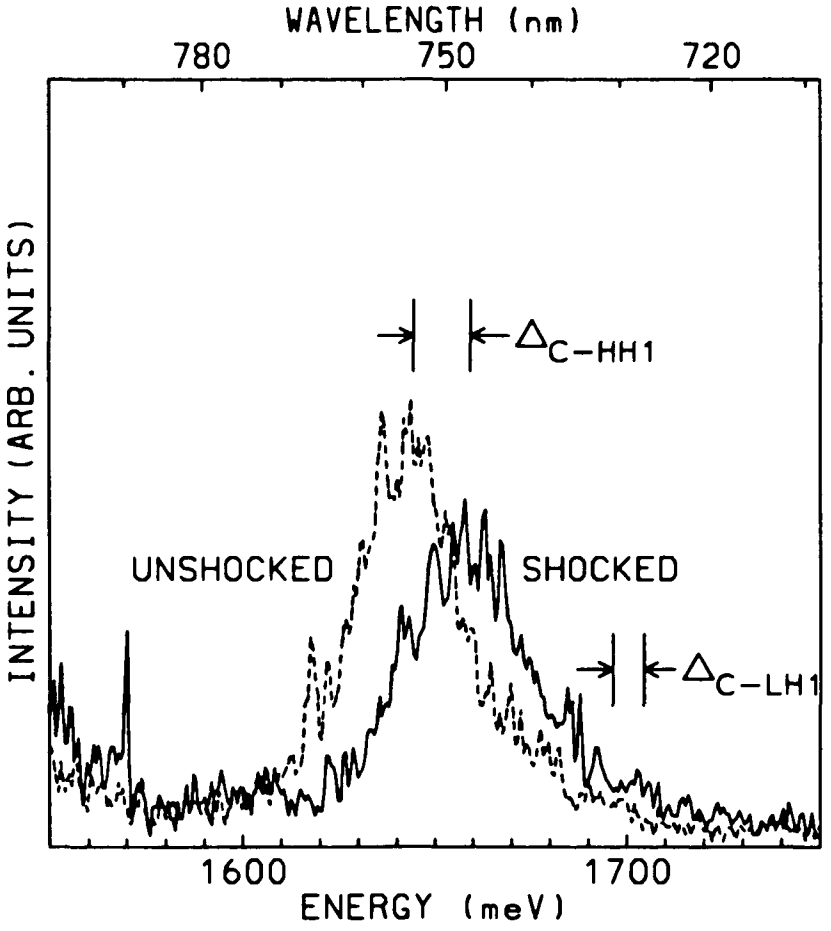

Figure 4.6.2. A plot of the unshocked (---) and shocked (—) spontaneous emission spectra from a *5nm* GaAs quantum well at low probe intensity (*400nJ*).

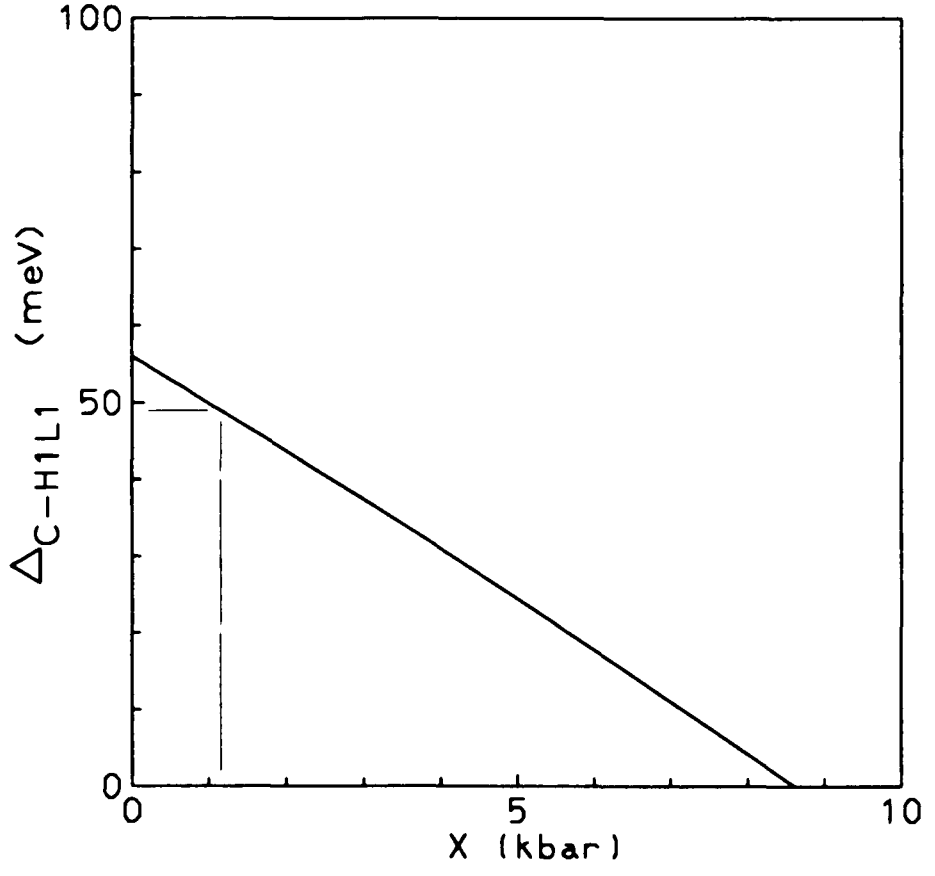

Figure 4.6.3. A plot of the stress dependence of the separation between the GaAs quantum well transitions c-hh1 and c-lh1 (Δ_{h1l1}).

In summary, shock compression of a GaAs quantum well along its growth direction has been observed. The determination of the stress components of the shock wave is identical to the analysis for bulk GaAs. It is found that there is $\sim 1 kbar$ difference between the longitudinal and transverse components of the shock wave.

V. Conclusion

In this thesis, the following has been learned about laser generated shock waves. First, the generation of reproducible shock waves using picosecond laser pulses requires all surfaces to be plane and parallel to each other so that there is good mechanical contact between the sample, the aluminum foil, and the quartz overlay. Second, confinement of the plasma by a quartz overlay allows the generation of high pressures. Finally, to increase the generated pressures, the energy of the laser pulses can be increased while keeping the spot size constant.

From the shock compression experiments on GaSe, the spontaneous and stimulated PL is attributed to an exciton exciton scattering mechanism. One of the effects of the shock compression is to change the band gap, which causes characteristic changes in the PL spectra within the framework of the exciton exciton scattering model. The shock induced line broadening is related uniquely to the transient nature of shock compression.

From the shock compression experiments on CdSe, an increase in the PL from shocked CdSe as compared with the unshocked CdSe has been observed. One possible explanation for this increase in the observed PL intensity under shock compression is the increase of the absorption coefficient due to the increase in the effective mass (similar to the effect seen in the GaAs static compression experiments). The time evolution of the shock pressure P in CdSe has also been determined from the blue shift of the PL under shock compression. The difference

between the longitudinal and transverse stress components of the shock wave ($[P + X] - [P] = X$) can not be determined in these shock compression experiments. There are two main problems encountered in this experiment. First, the PL lines corresponding to the $c-v_B$ transition and the $c-v_A$ transition can not be resolved. Second, within the range of shock pressure of interest, the transition with the lowest energy can be either $c-v_A$ or $c-v_B$ (see figure 4.3.5). This makes the analysis of the shock compression experiment very difficult. Therefore, two criteria that must be met in order to determine the transverse and longitudinal stress components of the shock wave is: 1) the PL emission lines corresponding to two transition which separate as a function of X must be clearly resolved; and 2) the ordering of the energy of the two transitions should not be changed within the range of shock pressure of interest.

It turns out that the valence bands of GaAs have the appropriate X behavior needed for a unique determination of the transverse and longitudinal stress components of the shock wave. From the shock compression experiments on GaAs, the transverse and longitudinal stress components of the shock wave can be determined from the shifts and splittings of the PL. The longitudinal stress component can be written as the sum of hydrostatic pressure plus a uniaxial stress. The uniaxial stress increases to a maximum of *~9kbar* then decreases. Therefore, the longitudinal stress component and the transverse stress component are unequal for shock propagation along the [001] direction of bulk n-GaAs.

In the shock compression experiments on GaAs, an increase in the PL intensity under shock compression has also been observed. In this case, the increase can be qualitatively explained by the enhancement of the absorption coefficient due to the stress difference between the longitudinal and transverse stress components of the shock wave.

In the static uniaxial compression experiments on GaAs, three major strain effects have been observed in the hole dynamics. The band edges involving the v1 and v2 valence bands have been seen to blue shift. The stress dependence of the effective mass causes an enhancement of the absorption coefficient, which shows as an increase in the density of the photogenerated carriers as a function of stress. As discussed above, this is also the most likely explanation for the increase in the PL from GaAs under shock compression. The time resolved PL spectra from n-GaAs is found to be nonexponential. The bimolecular recombination coefficient B is independent of stress, while the stress dependence of the decay constant A is in agreement with the stress dependence of the matrix elements. It is found that the effective lifetimes of the v1 holes decrease as a function of stress.

Also in this thesis, the first observation of shock compression of a GaAs quantum well along its growth direction has been observed. The determination of the stress components of the shock wave is identical to the analysis for bulk GaAs. It is found that there is $\sim 1 kbar$ difference between the longitudinal and transverse components of the shock wave.

VI. Future Direction

6.1 Shock Propagation In Semiconductor Heterostructures

From the shock compression experiments on bulk GaAs and quantum well, it has been shown that the stress components of the shock wave can be measured as a function of the propagation time. This suggests two new series of experiments involving shock propagation. First, it is interesting to simultaneously measure the shock velocity U_S and the time evolution of the longitudinal and transverse stress components of the shock wave. This can be accomplished by looking at the PL from two different quantum well (see figure 6.1.1). By varying the pump-probe delay time, the shock profile can be determined from the PL from quantum well #1 (see section 4.6). If the width of quantum well #2 is chosen such that the PL occurs at a spectral region separated from the PL from quantum well #1, the shock profile in quantum well #2 can be simultaneously determined. This also provides the time τ_Q needed for the shock front to move from quantum well #1 to quantum well #2. The shock velocity can then be determined from a time of flight calculation, since the spatial separation of the two quantum wells (l_Q) is known (i.e., $U_S = \frac{l_Q}{\tau_Q}$). For this experiment, the experimental setup described in section 3.3 need to be modified for liquid Helium temperatures, since this would give a better signal to noise ratio. At liquid Helium temperatures, it may also be possible to resolve the luminescence due to transitions involving defects from the luminescence

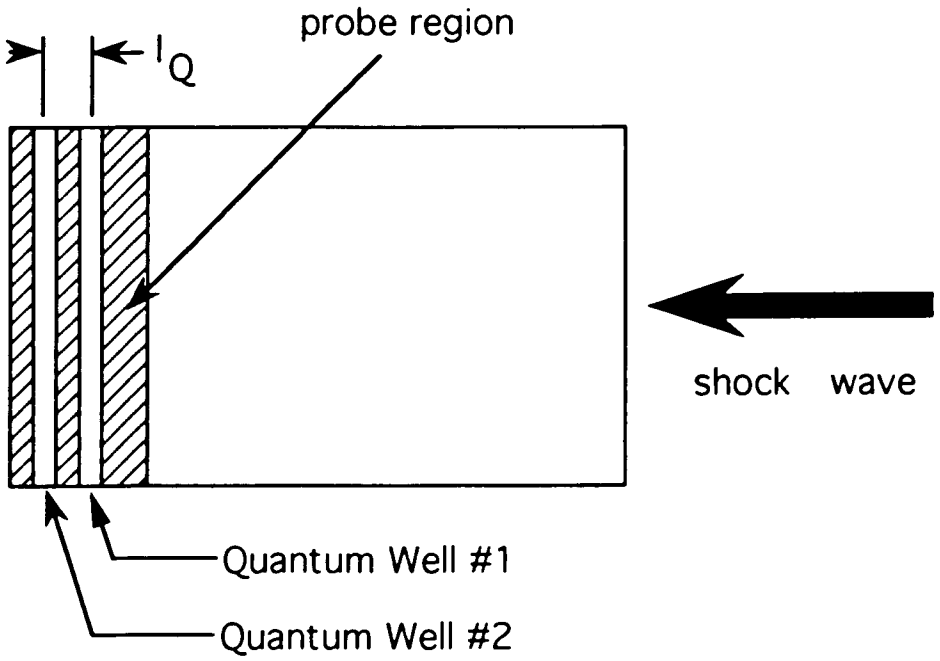

Figure 6.1.1. Schematic diagram of shock propagation in structures.

due to band to band transitions.

Another experiment concerns the influence of the peak pressure generated on the time needed for the equilibration of the longitudinal and transverse stress components of the shock wave. For this experiment, an experimental setup similar to the one described in section 3.3 can be used with a more powerful laser, so that the generated pressure can be increased.

6.2. Intervalence Transitions

One of the questions raised by the results of the stressed GaAs is what is the net transition time between the $v1$ and $v2$ valence subbands as a function of stress. The current experimental setup used for the static uniaxial compression experiment cannot be used to obtain this time. However, by substituting a tunable laser (such as a Ti:sapphire laser) for the CPM laser in the experimental setup described in section 4.5, the transition time may be determined. The basic idea is to observe the rise time of the photoluminescence at the Γ point. By comparing the rise time when the probe beam energy is tuned to generate holes in both the $v1$ and $v2$ valence subband (see figure 6.2.1b) with the control situation where the probe beam energy is tuned to just above the $v2$ so that it can only generate holes in the $v1$ valence subband (see figure 6.2.1a), the transition time between the $v1$ and $v2$ valence subband can be determined. Note that this transition time can only be determined if it is greater then the resolution of the experimental setup (otherwise, only a upper limit can be determined). From the typical pulse width of a Ti:sapphire laser of $2ps$, the resolution of the experiment is determined by the resolution of the synchroscan streak camera which is $10ps$.

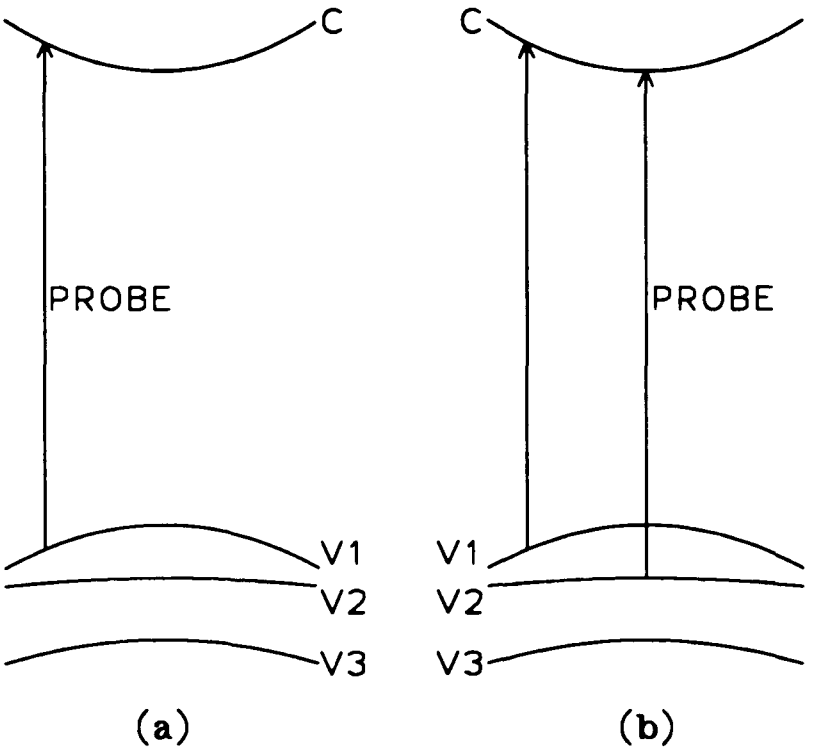

Figure 6.2.1. Schematic diagram of generation of carriers in a) control situation and b) test situation, using a tunable laser.

Appendix

A1. CdSe Transitional Energy Shifts Under Shock Compression

Using the elastic compliance for hexagonal lattices (4.3.3) and the shock compression stress vector (4.3.4), the strain stress relationship (2.2.7) is

$$\begin{pmatrix} \varepsilon_{11} \\ \varepsilon_{22} \\ \varepsilon_{33} \\ 2\varepsilon_{23} \\ 2\varepsilon_{31} \\ 2\varepsilon_{12} \end{pmatrix} = \begin{pmatrix} S_{11}^w & S_{12}^w & S_{13}^w & 0 & 0 & 0 \\ S_{12}^w & S_{11}^w & S_{13}^w & 0 & 0 & 0 \\ S_{13}^w & S_{13}^w & S_{33}^w & 0 & 0 & 0 \\ 0 & 0 & 0 & S_{44}^w & 0 & 0 \\ 0 & 0 & 0 & 0 & S_{44}^w & 0 \\ 0 & 0 & 0 & 0 & 0 & 2(S_{11}^w - S_{12}^w) \end{pmatrix} \begin{pmatrix} -P \\ -P \\ -P - X \\ 0 \\ 0 \\ 0 \end{pmatrix} .$$

This yields the strain stress relationship for shock compression along the c axis in hexagonal semiconductors:

$$\varepsilon_{11} = \varepsilon_{22} = -(S_{11}^w + S_{12}^w + S_{13}^w)P - S_{13}^w X \quad ; \tag{4.3.5a}$$

$$\varepsilon_{33} = -(2S_{13}^w + S_{33}^w)\, P - S_{33}^w X \quad ; \tag{4.3.5b}$$

and

$$2\varepsilon_{23} = 2\varepsilon_{31} = 2\varepsilon_{12} = 0 \quad . \tag{4.3.5c}$$

From equation 4.3.5, note that

$$\varepsilon_{\pm} \equiv \varepsilon_{11} - \varepsilon_{22} \pm 2i\varepsilon_{12} = 0 \tag{A1.1a}$$

and

$$\varepsilon_{\pm c} \equiv \varepsilon_{31} \pm i\varepsilon_{23} = 0 \quad . \tag{A1.1b}$$

Using equations A1.1 and 4.3.5, the strain Hamiltonian 4.3.2b becomes

$$H_{orb} = a_1^w(\varepsilon_{11} + \varepsilon_{22}) + a_0^w\varepsilon_{33} + b_1^w(\varepsilon_{11} + \varepsilon_{22})L_3^2 + b_0^w\varepsilon_{33}L_3^2$$

$$+ c_1^w(\varepsilon_+L_-^2 + \varepsilon_-L_+^2) + d_1^w\left[\varepsilon_{-c}\{L_3, L_+\} + \varepsilon_{+c}\{L_3, L_-\}\right]$$

$$= -\delta E_a^w - \left[\delta E_b^w\right]L_3^2 \quad , \tag{A1.2}$$

where

$$\delta E_a^w \equiv a_0^w\left[2S_{13}^w + S_{33}^w\right]P + 2a_1^w\left[S_{11}^w + S_{12}^w + S_{13}^w\right]P$$

$$+ \left[a_0^wS_{33}^w + 2a_1^wS_{13}^w\right]X$$

and

$$\delta E_b^w \equiv b_0^w\left[2S_{13}^w + S_{33}^w\right]P + 2b_1^w\left[S_{11}^w + S_{12}^w + S_{13}^w\right]P$$

$$+ \left[b_0^wS_{33}^w + 2b_1^wS_{13}^w\right]X \quad . \tag{4.3.8}$$

The crystal field and spin orbit Hamiltonian is

$$H_{so-cf} = \Delta_1\left[\mathbf{L}\cdot\bar{\sigma} - \frac{1}{2}\right] + \Delta_2\left[L_3^2 - 1\right] + \Delta_{cs2}\left[L_3\cdot\bar{\sigma}_3 - \frac{1}{2}\right] \quad , \tag{4.3.1}$$

where $\Delta_1 \equiv \dfrac{2\Delta_{so}}{3} - \dfrac{\Delta_{cs2}}{3}$ and $\Delta_2 \equiv \Delta_{cs1} + \dfrac{\Delta_{cs2}}{2}$.

From the stress Hamiltonian A1.2 and the crystal field and spin orbit Hamiltonian 4.3.1, the Hamiltonian for the valence band is

$$H_v \equiv H_{so-cf} + H_{orb} = C_0^w + C_1^wO_1 + C_2^wO_2^w + C_3^wO_3^w \quad , \tag{A1.3}$$

where

$$C_0^w \equiv -\frac{\Delta_1}{2} - \Delta_2 - \frac{\Delta_{cs2}}{2} - \delta E_a^w \quad , \tag{A1.4a}$$

$$C_1^w \equiv \Delta_1 \quad , \tag{A1.4b}$$

$$C_2^w \equiv \Delta_2 - \delta E_b^w \quad , \tag{A1.4c}$$

and

$$C_3^w \equiv \Delta_{cs2} \quad . \tag{A1.4d}$$

The relevant operators are

$$O_1 \equiv \mathbf{L}\cdot\bar{\boldsymbol{\sigma}} \quad , \tag{A1.5a}$$

$$O_2^w \equiv L_3^2 \quad , \tag{A1.5b}$$

and

$$O_3^w \equiv L_3\bar{\sigma}_3 \quad . \tag{A1.5c}$$

Using the operators A1.5 on the wave function $\Phi_{vA} \equiv P_+\chi_\uparrow$ yield

$$O_1\,\Phi_{vA} = \frac{1}{2}\Phi_{vA} \quad , \tag{A1.6a}$$

$$O_2^w\,\Phi_{vA} = \Phi_{vA} \quad , \tag{A1.6b}$$

and

$$O_3^w\,\Phi_{vA} = \frac{1}{2}\Phi_{vA} \quad . \tag{A1.6c}$$

Using the operators A1.5 on the wave function $\Phi_{vB} \equiv P_-\chi_\uparrow$ yield

$$O_1\,\Phi_{vB} = -\frac{1}{2}\Phi_{vB} - \frac{1}{\sqrt{2}}\Phi_{vC} \quad , \tag{A1.7a}$$

$$O_2^w \, \Phi_{vB} = \Phi_{vB} \quad , \tag{A1.7b}$$

and

$$O_3^w \, \Phi_{vB} = -\frac{1}{2} \Phi_{vB} \quad . \tag{A1.7c}$$

Using the operators A1.5 on the wave function $\Phi_{vC} \equiv P_z \chi_\downarrow$ yield

$$O_1 \, \Phi_{vC} = -\frac{1}{\sqrt{2}} \Phi_{vB} \quad , \tag{A1.8a}$$

$$O_2^w \, \Phi_{vC} = 0 \quad , \tag{A1.8b}$$

and

$$O_3^w \, \Phi_{vC} = 0 \quad . \tag{A1.8c}$$

Since the wave functions are orthonormal (i.e., $< \Phi_i \mid \Phi_j >$ is nonzero only for $i = j$), the matrix elements $< \Phi_i \mid O_k \mid \Phi_j >$ can be obtained from equations A1.6, A1.7, and A1.8. The only nonzero matrix elements $< \Phi_i \mid H_v \mid \Phi_j >$ are

$$< \Phi_{vA} \mid H_v \mid \Phi_{vA} > \equiv \Lambda_1^w = C_0^w + \frac{1}{2} C_1^w + C_2^w + \frac{1}{2} C_3^w \quad , \tag{A1.9a}$$

$$< \Phi_{vB} \mid H_v \mid \Phi_{vB} > \equiv \Lambda_2^w = C_0^w - \frac{1}{2} C_1^w + C_2^w - \frac{1}{2} C_3^w \quad , \tag{A1.9b}$$

$$< \Phi_{vC} \mid H_v \mid \Phi_{vC} > \equiv \Lambda_3^w = C_0^w \quad , \tag{A1.9c}$$

$$< \Phi_{vB} \mid H_v \mid \Phi_{vC} > \equiv \Lambda_{23}^w = -\frac{1}{\sqrt{2}} C_1^w \quad , \tag{A1.9d}$$

and

$$< \Phi_{vC} \mid H_v \mid \Phi_{vB} > \equiv \Lambda_{32}^w = -\frac{1}{\sqrt{2}} C_1^w = \Lambda_{23}^w \quad . \tag{A1.9e}$$

This yields the matrix

$$\mathbf{H}_\sigma \equiv \begin{array}{c} \begin{matrix} P_+\chi_\uparrow & P_-\chi_\uparrow & P_z\chi_\downarrow \end{matrix} \\ \begin{bmatrix} \Lambda_1^w & 0 & 0 \\ 0 & \Lambda_2^w & \Lambda_{23}^w \\ 0 & \Lambda_{23}^w & \Lambda_3^w \end{bmatrix} \end{array} , \tag{4.3.6}$$

where the components (from equation A1.9) are

$$\Lambda_1^w = -\delta E_{\bar{a}}^w - \delta E_b^w \ , \tag{4.3.7a}$$

$$\Lambda_2^w = -\Delta_1 - \Delta_{cs2} - \delta E_{\bar{a}}^w - \delta E_b^w \ , \tag{4.3.7b}$$

$$\Lambda_3^w = -\Delta_2 - \frac{1}{2}\Delta_1 - \frac{1}{2}\Delta_{cs2} - \delta E_{\bar{a}}^w \ , \tag{4.3.7c}$$

and

$$\Lambda_{23}^w = -\frac{1}{\sqrt{2}}\Delta_1 \ . \tag{4.3.7d}$$

The eigenvalues of equation 4.4.7 are

$$\lambda_{vA} = \Lambda_1^w \ , \tag{A1.10a}$$

$$\lambda_{vB} = \frac{1}{2}\left[\Lambda_2^w + \Lambda_3^w\right] + \frac{1}{2}\left[\left[\Lambda_2^w - \Lambda_3^w\right]^2 + \left[2\Lambda_{23}^w\right]^2\right]^{1/2} \ , \tag{A1.10b}$$

and

$$\lambda_{vC} = \frac{1}{2}\left[\Lambda_2^w + \Lambda_3^w\right] - \frac{1}{2}\left[\left[\Lambda_2^w - \Lambda_3^w\right]^2 + \left[2\Lambda_{23}^w\right]^2\right]^{1/2} \ . \tag{A1.10c}$$

Equation A1.10 give the energy of the band edges of the CdSe valence subbands v_A, v_B, and v_C. Note that

$$\frac{1}{2}\left[\Lambda_2^w + \Lambda_3^w\right] = -\frac{\Delta_{so}}{2} - \frac{\Delta_{cs1}}{2} - \frac{3\Delta_{cs2}}{4}$$

$$- \delta E_{\bar{a}}^w - \frac{1}{2}\delta E_b^w \qquad \text{(A1.11a)}$$

and

$$\frac{1}{2}\left[\left[\Lambda_2^w - \Lambda_3^w\right]^2 + \left[2\Lambda_{23}^w\right]^2\right]^{1/2} = \frac{\Delta_{so}}{2} - \frac{\Delta_{cs1}}{6} - \frac{\Delta_{cs2}}{4} + \frac{2(\Delta_{cs1})^2}{9\Delta_{so}}$$

$$+ \left[\frac{1}{6} - \frac{4\Delta_{cs1}}{9\Delta_{so}}\right]\delta E_b^w$$

$$+ \frac{2}{9\Delta_{so}}\left[\delta E_b^w\right]^2 + \ldots . \qquad \text{(A1.11b)}$$

Using A1.11, equation A1.10 become

$$\lambda_{vA} = -\delta E_{\bar{a}}^w - \delta E_b^w \ , \qquad \text{(A1.12a)}$$

$$\lambda_{vB} = -\frac{2\Delta_{cs1}}{3} - \Delta_{cs2} + \frac{2(\Delta_{cs1})^2}{9\Delta_{so}}$$

$$- \delta E_{\bar{a}}^w - \left[\frac{1}{3} + \frac{4\Delta_{cs1}}{9\Delta_{so}}\right]\delta E_b^w + \frac{2}{9\Delta_{so}}\left[\delta E_b^w\right]^2 + \ldots , \qquad \text{(A1.12b)}$$

and

$$\lambda_{vC} = -\Delta_{so} - \frac{\Delta_{cs1}}{3} - \frac{\Delta_{cs2}}{2} - \frac{2(\Delta_{cs1})^2}{9\Delta_{so}}$$

$$- \delta E_{\bar{a}}^w - \left[\frac{2}{3} - \frac{4\Delta_{cs1}}{9\Delta_{so}}\right]\delta E_b^w - \frac{2}{9\Delta_{so}}\left[\delta E_b^w\right]^2 + \ldots . \qquad \text{(A1.12c)}$$

To obtain the transitional energy shifts, the shift of the conduction band with stress is also needed. Using equation 4.3.5, the strain Hamiltonian 4.3.2a becomes

$$H_c = -a_c^w \left(\varepsilon_{11} + \varepsilon_{22} + \varepsilon_{33} \right)$$

$$= a_c^w \left(2S_{13}^w + S_{33}^w \right) P + 2a_c^w \left(S_{11}^w + S_{12}^w + S_{13}^w \right) P$$

$$+ \left(a_c^w S_{33}^w + 2a_c^w S_{13}^w \right) X \quad .$$

Therefore,

$$\Lambda_c^w \equiv \Phi_c H_c \Phi_c =$$

$$= a_c^w \left(2S_{13}^w + S_{33}^w \right) P + 2a_c^w \left(S_{11}^w + S_{12}^w + S_{13}^w \right) P$$

$$+ \left(a_c^w S_{33}^w + 2a_c^w S_{13}^w \right) X \quad . \qquad \text{(A1.13)}$$

Using equations A1.12 and A1.13, the transitional energies are

$$E_{c-vA}(P, X) \equiv \bar{E}_g^w + \Lambda_c^w - \lambda_{vA} = \bar{E}_g^w + \delta E_H^w + \delta E_b^w \quad , \qquad \text{(4.3.9a)}$$

$$E_{c-vB}(P, X) \equiv \bar{E}_g^w + \Lambda_c^w - \lambda_{vB}$$

$$= \bar{E}_g^w + \frac{2\Delta_{cs1}}{3} + \Delta_{cs2} - \frac{2(\Delta_{cs1})^2}{9\Delta_{so}} + \delta E_H^w$$

$$+ \left(\frac{1}{3} + \frac{4\Delta_{cs1}}{9\Delta_{so}} \right) \delta E_b^w - \frac{2}{9\Delta_{so}} \left[\delta E_b^w \right]^2 + \ldots \quad , \qquad \text{(4.3.9b)}$$

and

$$E_{c-vC}(P, X) \equiv \bar{E}_g^w + \Lambda_c^w - \lambda_{vC}$$

$$= \bar{E}_g^w + \Delta_{so} + \frac{\Delta_{cs1}}{3} + \frac{\Delta_{cs2}}{2} + \frac{2(\Delta_{cs1})^2}{9\Delta_{so}} + \delta E_H^w$$

$$+ \left[\frac{2}{3} - \frac{4\Delta_{cs1}}{9\Delta_{so}}\right]\delta E_b^w + \frac{2}{9\Delta_{so}}\left[\delta E_b^w\right]^2 + \ldots , \qquad (4.3.9c)$$

where

$$\delta E_H^w \equiv \left[\left[a_c^w + a_0^w\right]\left[2S_{13}^w + S_{33}^w\right] + 2\left[a_c^w + a_1^w\right]\left[S_{11}^w + S_{12}^w + S_{13}^w\right]\right]P$$

$$+ \left[\left[a_c^w + a_0^w\right]S_{33}^w + 2\left[a_c^w + a_1^w\right]S_{13}^w\right]X \quad . \qquad (4.3.10)$$

Then, the shifts of the transitional energies with P and X are

$$\Delta E_{c-vA}(P, X) \equiv E_{c-vA}(P, X) - E_{c-vA}(P = 0kbar, X = 0kbar)$$

$$= \delta E_H^w + \delta E_b^w \quad , \qquad (4.3.11a)$$

$$\Delta E_{c-vB}(P, X) \equiv E_{c-vB}(P, X) - E_{c-vB}(P = 0kbar, X = 0kbar)$$

$$= \delta E_H^w + \left[\frac{1}{3} + \frac{4\Delta_{cs1}}{9\Delta_{so}}\right]\delta E_b^w$$

$$- \left[\frac{2}{9\Delta_{so}}\right]\left[\delta E_b^w\right]^2 + \ldots , \qquad (4.3.11b)$$

and

$$\Delta E_{c-vC}(P, X) \equiv E_{c-vC}(P, X) - E_{c-vC}(P = 0kbar, X = 0kbar)$$

$$= \delta E_H^w + \left[\frac{2}{3} - \frac{4\Delta_{cs1}}{9\Delta_{so}}\right]\delta E_b^w$$

$$+ \left[\frac{2}{9\Delta_{so}}\right]\left[\delta E_b^w\right]^2 + \ldots . \qquad (4.3.11c)$$

A2. GaAs Transitional Energy Shifts Under Shock Compression

Using the elastic compliance for cubic lattices (4.4.4) and the shock compression stress vector (4.3.4), the strain stress relationship (2.2.7) is

$$\begin{bmatrix} \varepsilon_{11} \\ \varepsilon_{22} \\ \varepsilon_{33} \\ 2\varepsilon_{23} \\ 2\varepsilon_{31} \\ 2\varepsilon_{12} \end{bmatrix} = \begin{bmatrix} S_{11}^z & S_{12}^z & S_{12}^z & 0 & 0 & 0 \\ S_{12}^z & S_{11}^z & S_{12}^z & 0 & 0 & 0 \\ S_{12}^z & S_{12}^z & S_{11}^z & 0 & 0 & 0 \\ 0 & 0 & 0 & S_{44}^z & 0 & 0 \\ 0 & 0 & 0 & 0 & S_{44}^z & 0 \\ 0 & 0 & 0 & 0 & 0 & S_{44}^z \end{bmatrix} \begin{bmatrix} -P \\ -P \\ -P - X \\ 0 \\ 0 \\ 0 \end{bmatrix} .$$

This yields the strain stress relationship for shock compression along the [001] axis in cubic semiconductors:

$$\varepsilon_{11} = \varepsilon_{22} = -\left[S_{11}^z + 2S_{12}^z\right] P - S_{12}^z X \ ; \qquad (4.4.5a)$$

$$\varepsilon_{33} = -\left[S_{11}^z + 2S_{12}^z\right] P - S_{11}^z X \ ; \qquad (4.4.5b)$$

and

$$2\varepsilon_{23} = 2\varepsilon_{31} = 2\varepsilon_{12} = 0 \ . \qquad (4.4.5c)$$

From equation 4.4.5, note that

$$\left[\varepsilon_{11} + \varepsilon_{22} + \varepsilon_{33}\right] = -(S_{11}^z + 2S_{12}^z)(3P + X) \ , \qquad (A2.1a)$$

$$\left[\varepsilon_{11}\left[L_1^2 - \frac{1}{3}L^2\right] + c.p.\right] = -\left[(S_{11}^z + 2S_{12}^z)P\right]$$

$$\times \left[L_1^2 - \frac{1}{3}L^2 + L_2^2 - \frac{1}{3}L^2 + L_3^2 - \frac{1}{3}L^2\right]$$

$$- \left[S_{12}^z X\right]\left[L_1^2 - \frac{1}{3}L^2 + L_2^2 - \frac{1}{3}L^2\right]$$

$$- \left[S_{11}^z X\right]\left[L_3^2 - \frac{1}{3}L^2\right]$$

$$= -\left[(S_{11}^z - S_{12}^z)X\right]\left[L_3^2 - \frac{1}{3}L^2\right] \quad , \qquad \text{(A2.1b)}$$

and

$$\left[\varepsilon_{11}\left[L_1\bar{\sigma}_1 - \frac{1}{3}\mathbf{L}\cdot\bar{\boldsymbol{\sigma}}\right] + c.p.\right] = -\left[(S_{11}^z - S_{12}^z)X\right]$$

$$\times \left[L_3\bar{\sigma}_3 - \frac{1}{3}\mathbf{L}\cdot\bar{\boldsymbol{\sigma}}\right] \quad . \qquad \text{(A2.1c)}$$

Using equations A2.1 and 4.4.5c, the strain Hamiltonians 4.4.2 become

$$H_{orb} = a_1^z\left[\varepsilon_{11}+\varepsilon_{22}+\varepsilon_{33}\right] + 3b_1^z\left[\varepsilon_{11}\left[L_1^2 - \frac{1}{3}L^2\right] + c.p.\right]$$

$$+ 2\sqrt{3}d_1^z\left[\varepsilon_{12}\{L_1, L_2\}+ c.p.\right]$$

$$= -a_1^z(S_{11}^z + 2S_{12}^z)(3P + X) - 3b_1^z\left[(S_{11}^z - S_{12}^z)X\right]\left[L_3^2 - \frac{1}{3}L^2\right] \qquad \text{(A2.2a)}$$

and

$$H_{spin} = 2a_2^z\left[\varepsilon_{11}+\varepsilon_{22}+\varepsilon_{33}\right]\mathbf{L}\cdot\bar{\boldsymbol{\sigma}} + 6b_2^z\left[\varepsilon_{11}\left[L_1\bar{\sigma}_1 - \frac{1}{3}\mathbf{L}\cdot\bar{\boldsymbol{\sigma}}\right] + c.p.\right]$$

$$+ 2\sqrt{3}d_2^z\left[\varepsilon_{12}(L_1\bar{\sigma}_2 + L_2\bar{\sigma}_1) + c.p.\right]$$

$$= -2a_2^z(S_{11}^z + 2S_{12}^z)(3P + X)\mathbf{L}\cdot\bar{\boldsymbol{\sigma}}$$

$$- 6b_2^z\left[(S_{11}^z - S_{12}^z)X\right]\left[L_3\bar{\sigma}_3 - \frac{1}{3}\mathbf{L}\cdot\bar{\boldsymbol{\sigma}}\right] \quad . \qquad \text{(A2.2b)}$$

From equations 4.4.1 ($H_{so} = \frac{2\Delta_o}{3}\mathbf{L}\cdot\bar{\boldsymbol{\sigma}} - \frac{\Delta_o}{3}$) and A2.2, the Hamiltonian for the valence band is

$$H_v \equiv H_{so} + H_{orb} + H_{spin} = C_0 + C_1O_1 + C_2O_2^z + C_3O_3^z \quad , \qquad \text{(A2.3)}$$

where

$$C_0 \equiv -\frac{\Delta_o}{3} - a_1^z(S_{11}^z + 2S_{12}^z)(3P + X) \quad , \qquad \text{(A2.4a)}$$

$$C_1 \equiv \frac{2\Delta_o}{3} - 2a_2^z(S_{11}^z + 2S_{12}^z)(3P + X) \ , \tag{A2.4a}$$

$$C_2 \equiv -3b_1^z(S_{11}^z - S_{12}^z)X \ , \tag{A2.4c}$$

and

$$C_3 \equiv -6b_2^z(S_{11}^z - S_{12}^z)X \ . \tag{A2.4d}$$

The relevant operators are

$$O_1 \equiv \mathbf{L}\cdot\bar{\boldsymbol{\sigma}} \ , \tag{A2.5a}$$

$$O_2^z \equiv L_3^2 - \frac{1}{3}L^2 \ , \tag{A2.5b}$$

and

$$O_3^z \equiv L_3\bar{\sigma}_3 - \frac{1}{3}\mathbf{L}\cdot\bar{\boldsymbol{\sigma}} \ . \tag{A2.5c}$$

The relevant wave functions for [001] stress in GaAs are

$$\Phi_{v2} \equiv \left|\frac{3}{2}, \frac{3}{2}\right\rangle = P_+\chi_\uparrow \ , \tag{4.4.6a}$$

$$\Phi_{v1} \equiv \left|\frac{3}{2}, \frac{1}{2}\right\rangle = \frac{1}{\sqrt{3}}P_+\chi_\downarrow - \frac{\sqrt{2}}{\sqrt{3}}P_z\chi_\uparrow \ , \tag{4.4.6b}$$

and

$$\Phi_{v3} \equiv \left|\frac{1}{2}, \frac{1}{2}\right\rangle = \frac{\sqrt{2}}{\sqrt{3}}P_+\chi_\downarrow + \frac{1}{\sqrt{3}}P_z\chi_\uparrow \ , \tag{4.4.3}$$

where $P_+ \equiv \frac{1}{\sqrt{2}}\left[P_x + iP_y\right]$, P_x, P_y, and P_z, are the p-like basis functions, and $\chi_\uparrow$ and $\chi_\downarrow$ are the spin basis functions.

Using the operators A2.5 on the wave function Φ_{v2} yield

$$O_1 \Phi_{v2} = \frac{1}{2}\Phi_{v2} \quad , \tag{A2.6a}$$

$$O_2^z \Phi_{v2} = \frac{1}{3}\Phi_{v2} \quad , \tag{A2.6b}$$

and

$$O_3^z \Phi_{v2} = \frac{1}{3}\Phi_{v2} \quad . \tag{A2.6c}$$

Using the operators A2.5 on the wave function Φ_{v1} yield

$$O_1 \Phi_{v1} = \frac{1}{2}\Phi_{v1} \quad , \tag{A2.7a}$$

$$O_2^z \Phi_{v1} = -\frac{1}{3}\Phi_{v1} + \frac{\sqrt{2}}{3}\Phi_{v3} \quad , \tag{A2.7b}$$

and

$$O_3^z \Phi_{v1} = -\frac{1}{3}\Phi_{v1} - \frac{\sqrt{2}}{6}\Phi_{v3} \quad . \tag{A2.7c}$$

Using the operators A2.5 on the wave function Φ_{v3} yield

$$O_1 \Phi_{v3} = -\Phi_{v3} \quad , \tag{A2.8a}$$

$$O_2^z \Phi_{v3} = \frac{\sqrt{2}}{3}\Phi_{v1} \quad , \tag{A2.8b}$$

and

$$O_3^z \Phi_{v3} = -\frac{\sqrt{2}}{6}\Phi_{v1} \quad . \tag{A2.8c}$$

Since the wave functions are orthonormal (i.e., $< \Phi_i | \Phi_j >$ is nonzero only for $i = j$), the matrix elements $< \Phi_i | O_k | \Phi_j >$ can be obtained from equations A2.6,

A3.7, and A3.8. The only nonzero matrix elements $< \Phi_i | H_v | \Phi_j >$ are

$$< \Phi_{v2} | H_v | \Phi_{v2} > \equiv \Lambda_2^z = C_0 + \frac{1}{2}C_1 + \frac{1}{3}C_2 + \frac{1}{3}C_3 \ , \qquad \text{(A2.9a)}$$

$$< \Phi_{v1} | H_v | \Phi_{v1} > \equiv \Lambda_1^z = C_0 + \frac{1}{2}C_1 - \frac{1}{3}C_2 - \frac{1}{3}C_3 \ , \qquad \text{(A2.9b)}$$

$$< \Phi_{v3} | H_v | \Phi_{v3} > \equiv \Lambda_3^z = C_0 - C_1 \ , \qquad \text{(A2.9c)}$$

$$< \Phi_{v1} | H_v | \Phi_{v3} > \equiv \Lambda_{13}^z = \frac{\sqrt{2}}{3}C_2 - \frac{\sqrt{2}}{6}C_3 \ , \qquad \text{(A2.9d)}$$

and

$$< \Phi_{v3} | H_v | \Phi_{v1} > \equiv \Lambda_{31}^z = \frac{\sqrt{2}}{3}C_2 - \frac{\sqrt{2}}{6}C_3 = \Lambda_{13}^z \ . \qquad \text{(A2.9e)}$$

This yields the matrix

$$\mathbf{H_\sigma} \equiv \begin{array}{c} \begin{matrix} \Phi_{v2} & \Phi_{v1} & \Phi_{v3} \end{matrix} \\ \begin{bmatrix} \Lambda_2^z & 0 & 0 \\ 0 & \Lambda_1^z & \Lambda_{13}^z \\ 0 & \Lambda_{13}^z & \Lambda_3^z \end{bmatrix} \end{array} \ , \qquad \text{(4.4.7)}$$

where the components (from equation A2.9) are

$$\Lambda_2^z = -\delta E_H^v - \frac{\delta E_{001}}{2} \ , \qquad \text{(4.4.8a)}$$

$$\Lambda_1^z = -\delta E_H^v + \frac{\delta E_{001}}{2} \ , \qquad \text{(4.4.8b)}$$

$$\Lambda_3^z = -\Delta_o - \delta E_H^v \ , \qquad \text{(4.4.8c)}$$

and

$$\Lambda_{13}^z = \frac{\sqrt{2}\delta E_{\overline{001}}}{2} \ ; \qquad \text{(4.4.8d)}$$

with

$$\delta E_{H}^{v} \equiv (a_1^z + a_2^z)(S_{11}^z + 2S_{12}^z)(3P + X) \quad , \tag{4.4.9a}$$

$$\delta E_{H}^{v} \equiv (a_1^z - 2a_2^z)(S_{11}^z + 2S_{12}^z)(3P + X) \quad , \tag{4.4.9b}$$

$$\delta E_{001} \equiv 2(b_1^z + 2b_2^z)(S_{11}^z - S_{12}^z)X \quad , \tag{4.4.9c}$$

and

$$\delta E_{\overline{001}} \equiv 2(b_1^z - b_2^z)(S_{11}^z - S_{12}^z)X \quad . \tag{4.4.9d}$$

The eigenvalues of equation 4.4.7 are

$$\lambda_{v2}^z = \Lambda_2^z \quad , \tag{A2.10a}$$

$$\lambda_{v1}^z = \frac{1}{2}\left[\Lambda_1^z + \Lambda_3^z\right] + \frac{1}{2}\left[\left[\Lambda_1^z - \Lambda_3^z\right]^2 + \left[2\Lambda_{13}^z\right]^2\right]^{1/2} \quad , \tag{A2.10b}$$

and

$$\lambda_{v3}^z = \frac{1}{2}\left[\Lambda_1^z + \Lambda_3^z\right] - \frac{1}{2}\left[\left[\Lambda_1^z - \Lambda_3^z\right]^2 + \left[2\Lambda_{13}^z\right]^2\right]^{1/2} \quad . \tag{A2.10c}$$

Equation A2.10 give the energy of the band edges of the GaAs valence subbands v_1, v_2, and v_3. Note that

$$\frac{1}{2}\left[\Lambda_1^z + \Lambda_3^z\right] = -\frac{\Delta_o}{2} - \delta E_{H}^{v} + \frac{\delta E_{001}}{4} \quad , \tag{A2.11a}$$

and (for $\delta E_{H}^{v} = \delta E_{H}^{v}$ and $\delta E_{\overline{001}} = \delta E_{001}$),

$$\frac{1}{2}\left[\left[\Lambda_1^z - \Lambda_3^z\right]^2 + \left[2\Lambda_{13}^z\right]^2\right]^{1/2} = \frac{\Delta_o}{2} + \frac{\delta E_{001}}{4} + \frac{\delta E_{001}^2}{2\Delta_o} + \ldots \quad . \tag{A2.11b}$$

Using A2.11, equation A2.10 become

$$\lambda_{v1}^{z} = -\delta E_H^v + \frac{\delta E_{001}}{2} + \frac{\delta E_{001}^2}{2\Delta_o} + \ldots \ , \qquad \text{(A2.12a)}$$

$$\lambda_{v2}^{z} = -\delta E_H^v + \frac{\delta E_{001}}{2} \ , \qquad \text{(A2.12b)}$$

and

$$\lambda_{v3}^{z} = -\Delta_o - \delta E_H^v - \frac{\delta E_{001}^2}{2\Delta_o} - \ldots \ . \qquad \text{(A2.12c)}$$

To obtain the transitional energy shifts, the shift of the conduction band with stress is also needed. Using equation A2.1a, the strain Hamiltonian 4.4.3 becomes

$$H_c = -a_c^z \left(\varepsilon_{11} + \varepsilon_{22} + \varepsilon_{33} \right) = a_c^z (S_{11}^z + 2S_{12}^z)(3P + X) \ . \qquad \text{(A2.13)}$$

Therefore, $< \Phi_c \mid H_c \mid \Phi_c > \equiv \Lambda_c^z = a_c^z (S_{11}^z + 2S_{12}^z)(3P + X)$. The transitional energies are

$$E_{c-v1}(P, X) \equiv \bar{E}_g + \Lambda_c^z - \lambda_{v1}^z = \bar{E}_g + \delta E_H^s - \frac{\delta E_{001}}{2} - \frac{\delta E_{001}^2}{2\Delta_o} + \ldots \ ,$$

$$E_{c-v2}(P, X) \equiv \bar{E}_g + \Lambda_c^z - \lambda_{v2}^z = \bar{E}_g + \delta E_H^s + \frac{\delta E_{001}}{2} \ ,$$

and

$$E_{c-v3}(P, X) \equiv \bar{E}_g + \Lambda_c^z - \lambda_{v3}^z = \bar{E}_g + \Delta_o + \delta E_H^s + \frac{\delta E_{001}^2}{2\Delta_o} + \ldots \ ,$$

where $\delta E_H^s \equiv (a_c^z + a_1^z)(S_{11}^z + 2S_{12}^z)(3P + X)$. Then, the shifts of the transitional energies with P and X are

$$\Delta E_{c-v1}(P, X) \equiv E_{c-v1}(P, X) - E_{c-v1}(P = 0kbar, X = 0kbar)$$

$$= \delta E_{II}^{s} - \frac{\delta E_{001}}{2} - \frac{\delta E_{001}^{2}}{2\Delta_o} + \ldots , \tag{4.4.10a}$$

$$\Delta E_{c-v2}(P, X) \equiv E_{c-v2}(P, X) - E_{c-v2}(P = 0kbar, X = 0kbar)$$

$$= \delta E_{II}^{s} + \frac{\delta E_{001}}{2} , \tag{4.4.10b}$$

and

$$\Delta E_{c-v3}(P, X) \equiv E_{c-v3}(P, X) - E_{c-v3}(P = 0kbar, X = 0kbar)$$

$$= \delta E_{II}^{s} + \frac{\delta E_{001}^{2}}{2\Delta_o} + \ldots . \tag{4.4.10c}$$

A3. GaAs Matrix Elements Under Shock Compression

The relevant wave functions for [001] stress in GaAs are

$$\Phi_{v2} \equiv \left| \frac{3}{2}, \frac{3}{2} \right\rangle = P_+ \chi_\uparrow \ , \tag{4.4.6a}$$

$$\Phi_{v1} \equiv \left| \frac{3}{2}, \frac{1}{2} \right\rangle = \frac{1}{\sqrt{3}} P_+ \chi_\downarrow - \frac{\sqrt{2}}{\sqrt{3}} P_z \chi_\uparrow \ , \tag{4.4.6b}$$

and

$$\Phi_{v3} \equiv \left| \frac{1}{2}, \frac{1}{2} \right\rangle = \frac{\sqrt{2}}{\sqrt{3}} P_+ \chi_\downarrow + \frac{1}{\sqrt{3}} P_z \chi_\uparrow \ , \tag{4.4.3}$$

where $P_+ \equiv \frac{1}{\sqrt{2}} \left[P_x + iP_y \right]$, P_x, P_y, and P_z, are the p-like basis functions, and $\chi_\uparrow$ and $\chi_\downarrow$ are the spin basis functions.

From perturbation theory, the first order wave function is

$$\Psi_i = \Phi_i + \sum_{j(\neq i)} \frac{\langle \Phi_j | H_v | \Phi_i \rangle}{E_i^o - E_j^o} \Phi_j \ . \tag{A3.1}$$

With

$$\langle \Phi_{v1} | H_v | \Phi_{v3} \rangle \equiv \Lambda_{13}^z = \frac{\sqrt{2} \delta E_{\overline{001}}}{2} \tag{4.4.8d}$$

and

$$\langle \Phi_{v3} | H_v | \Phi_{v1} \rangle \equiv \Lambda_{31}^z = \Lambda_{13}^z \ , \tag{A2.12e}$$

the first order wave functions are

$$\Psi_{v1} = \Phi_{v1} + \left[\frac{\Lambda_{23}}{-\Delta_o}\right]\Phi_{v3}$$

$$= \left[\sqrt{2} - 2\frac{\Lambda_{23}}{\Delta_o}\right]\frac{1}{\sqrt{6}}P_+\chi_\downarrow - \left[2 + \sqrt{2}\frac{\Lambda_{23}}{\Delta_o}\right]\frac{1}{\sqrt{6}}P_z\chi_\uparrow \quad , \tag{A3.2a}$$

$$\Psi_{v2} = P_+\chi_\uparrow \quad , \tag{A3.2b}$$

and

$$\Psi_{v3} = \Phi_{v1} + \left[\frac{\Lambda_{23}}{\Delta_o}\right]\Phi_{v3}$$

$$= \left[2 + \sqrt{2}\frac{\Lambda_{23}}{\Delta_o}\right]\frac{1}{\sqrt{6}}P_+\chi_\downarrow + \left[\sqrt{2} - 2\frac{\Lambda_{23}}{\Delta_o}\right]\frac{1}{\sqrt{6}}P_z\chi_\uparrow \quad . \tag{A3.2c}$$

The matrix elements are

$$< S\chi_\uparrow | \hat{\mathbf{e}}\cdot\mathbf{p} | \Psi_{v1} > = -\left[2 + \sqrt{2}\frac{\Lambda_{23}}{\Delta_o}\right]\frac{1}{\sqrt{6}}M_z \quad , \tag{A3.3a}$$

$$< S\chi_\uparrow | \hat{\mathbf{e}}\cdot\mathbf{p} | \Psi_{v2} > = M_+ \quad , \tag{A3.3b}$$

$$< S\chi_\uparrow | \hat{\mathbf{e}}\cdot\mathbf{p} | \Psi_{v3} > = \left[\sqrt{2} - 2\frac{\Lambda_{23}}{\Delta_o}\right]\frac{1}{\sqrt{6}}M_z \quad , \tag{A3.3c}$$

$$< S\chi_\downarrow | \hat{\mathbf{e}}\cdot\mathbf{p} | \Psi_{v1} > = \left[\sqrt{2} - 2\frac{\Lambda_{23}}{\Delta_o}\right]\frac{1}{\sqrt{6}}M_+ \quad , \tag{A3.3d}$$

$$< S\chi_\downarrow | \hat{\mathbf{e}}\cdot\mathbf{p} | \Psi_{v2} > = 0 \quad , \tag{A3.3e}$$

and

$$< S\chi_\downarrow | \hat{\mathbf{e}}\cdot\mathbf{p} | \Psi_{v3} > = \left[2 + \sqrt{2}\frac{\Lambda_{23}}{\Delta_o}\right]\frac{1}{\sqrt{6}}M_+ \quad , \tag{A3.3f}$$

where $M_z \equiv \langle S | \hat{\mathbf{e}}\cdot\mathbf{p} | P_z \rangle = \sqrt{6} M_{cv} \hat{\mathbf{e}}\cdot\hat{\mathbf{k}}$ and $M_+ \equiv \langle S | \hat{\mathbf{e}}\cdot\mathbf{p} | P_+ \rangle = \sqrt{3} M_{cv} \hat{\mathbf{e}}\cdot(\hat{\mathbf{i}} + i\hat{\mathbf{j}})$.

The matrix elements $| \langle c | \hat{\mathbf{e}}\cdot\mathbf{p} | v \rangle |^2$ for polarization $\parallel$ to the [001] stress axis are

$$| \langle S\chi_\uparrow | \hat{\mathbf{e}}\cdot\mathbf{p} | \Psi_{v1} \rangle |^2 = \left[2 + \sqrt{2} \frac{\Lambda_{23}}{\Delta_o} \right]^2 M_{cv}^2$$

$$= \left[4 + 4\sqrt{2} \frac{\Lambda_{23}}{\Delta_o} + 2 \frac{(\Lambda_{23})^2}{(\Delta_o)^2} \right] M_{cv}^2 \quad , \tag{A3.4a}$$

$$| \langle S\chi_\downarrow | \hat{\mathbf{e}}\cdot\mathbf{p} | \Psi_{v2} \rangle |^2 = 0 \quad , \tag{A3.4b}$$

and

$$| \langle S\chi_\uparrow | \hat{\mathbf{e}}\cdot\mathbf{p} | \Psi_{v3} \rangle |^2 = \left[\sqrt{2} - 2 \frac{\Lambda_{23}}{\Delta_o} \right]^2 M_{cv}^2$$

$$= \left[2 - 4\sqrt{2} \frac{\Lambda_{23}}{\Delta_o} + 4 \frac{(\Lambda_{23})^2}{(\Delta_o)^2} \right] M_{cv}^2 \quad . \tag{A3.4c}$$

The matrix elements $| \langle c | \hat{\mathbf{e}}\cdot\mathbf{p} | v \rangle |^2$ for polarization $\perp$ to the [001] stress axis are

$$| \langle S\chi_\downarrow | \hat{\mathbf{e}}\cdot\mathbf{p} | \Psi_{v1} \rangle |^2 = \left[\sqrt{2} - 2 \frac{\Lambda_{23}}{\Delta_o} \right]^2 \frac{M_{cv}^2}{2}$$

$$= \left[2 - 4\sqrt{2} \frac{\Lambda_{23}}{\Delta_o} + 4 \frac{(\Lambda_{23})^2}{(\Delta_o)^2} \right] \frac{M_{cv}^2}{2} \quad , \tag{A3.5a}$$

$$| \langle S\chi_\uparrow | \hat{\mathbf{e}}\cdot\mathbf{p} | \Psi_{v2} \rangle |^2 = 3M_{cv}^2 \quad , \tag{A3.5b}$$

and

$$| < S\chi_{\downarrow} | \hat{\mathbf{e}}\cdot\mathbf{p} | \Psi_{v3} > |^2 = \left[2 + \sqrt{2}\frac{\Lambda_{23}}{\Delta_o} \right]^2 \frac{M_{cv}^2}{2}$$

$$= \left[4 + 4\sqrt{2}\frac{\Lambda_{23}}{\Delta_o} + 2\frac{(\Lambda_{23})^2}{(\Delta_o)^2} \right] \frac{M_{cv}^2}{2} \quad . \qquad \text{(A3.5c)}$$

Then, the matrix elements $| < c | \hat{\mathbf{e}}\cdot\mathbf{p} | v > |^2$ for different polarization relative to the [001] stress axis (to first order in $\frac{\delta E_{001}}{\Delta_o}$) are proportional to

	$\parallel$	$\perp$
v_1	$4\left[1 + \frac{\delta E_{001}}{\Delta_o} \right]$	$\left[1 - \frac{2\delta E_{001}}{\Delta_o} \right]$
v_2	0	3
v_3	$2\left[1 - \frac{2\delta E_{001}}{\Delta_o} \right]$	$2\left[1 + \frac{\delta E_{001}}{\Delta_o} \right]$

(4.5.8)

A4. Electron Hole Plasma Photoluminescence Line Shape

The line shape due to band to band transitions has been given by Beeb and Williams[132] as

$$I(h\nu) = \sum_{n,j} G \int d^3\vec{k}_n \left\{ \int d^3\vec{k}_j \left[\frac{| A^+_{n\to j}(\tau) |^2}{\tau} \rho(\vec{k}) \right] \right\} , \qquad \text{(A4.1)}$$

where G is a constant, $\vec{k}_{n(j)}$ are the wave vectors of the electron (hole) in the n^{th} conduction (j^{th} valence) band, $\frac{| A^+_{n\to j}(\tau) |^2}{\tau}$ is the transition probability, and $\rho(\vec{k}) = \rho_n(\vec{k}_n)\, \rho_j(\vec{k}_j)$ is the joint number of carriers per $d^3\vec{k}_n d^3\vec{k}_j$. The number of electrons per $d^3\vec{k}_n$ in the $n^{\underline{th}}$ conduction band is given by the product of the density of states and the Fermi function,

$$\rho_n(\vec{k}_n) = \frac{dN_n}{d^3\vec{k}_n} \left[1 + e^{\beta_n (E(\vec{k}_n) - \mu_n)} \right]^{-1} = \frac{2V}{(2\pi)^3} \left[1 + e^{\beta_n (E(\vec{k}_n) - \mu_n)} \right]^{-1} . \qquad \text{(A4.2a)}$$

Similarly, the number of holes per $d^3\vec{k}_j$ in the $j^{\underline{th}}$ valence band is given by

$$\rho_j(\vec{k}_j) = \frac{dN_j}{d^3\vec{k}_j} \left[e^{-\beta_j (E(\vec{k}_j) - \mu_j)} + 1 \right]^{-1} = \frac{2V}{(2\pi)^3} \left[e^{-\beta_j (E(\vec{k}_j) - \mu_j)} + 1 \right]^{-1} . \qquad \text{(A4.2b)}$$

The transition probability [132] is

$$\frac{| A^+_{n\to j}(\tau) |^2}{\tau} = | \langle \phi_j | W^+_{\vec{Q}\,\alpha} | \phi_n \rangle |^2 \frac{2\pi}{\hbar} \delta(\hbar\omega_{nj}) , \qquad \text{(A4.3)}$$

where $\omega_{nj} = \frac{1}{\hbar} \left[h\nu - (\varepsilon_n - \varepsilon_j) \right]$, $E_{n(j)}(\vec{k}_{n(j)})$ is the electron (hole) energy,

$$W^+_{\vec{Q}\,\alpha} = \frac{-e}{m_n} V_{EM}^{-1/2} \left[\frac{\hbar}{\nu} \right]^{1/2} \sqrt{(n_{\vec{Q}\,\alpha} + 1)\, \rho_{\vec{Q}\alpha}(h\nu)}\ \mathbf{a}^+_{\vec{Q}\,\alpha}\, e^{-i\vec{Q}\cdot r}\, \hat{e}_\alpha \cdot \mathbf{p}$$

is the time independent interaction operator, m_n is the effective mass of the $n^{\underline{th}}$ conduction band, V_{EM} is the volume of the EM field, $\vec{Q}$ is the photon wave vector ($(2\pi\nu)^2 = c^2 |\vec{Q}|^2$), α is the photon polarization index (i.e., unit vectors $\hat{e}_\alpha$ such that $\hat{e}_\alpha \cdot \hat{e}_\beta = \delta_{\alpha\beta}$, and $\vec{Q} \cdot \hat{e}_\alpha = 0$), $n_{\vec{Q}\alpha}$ is the number of photons with wave vector $\vec{Q}$ and polarization $\hat{e}_\alpha$, $\rho_{\vec{Q}\alpha}(h\nu) = \frac{\nu^2}{hc^3} V_{EM}\, d\Omega\, d(h\nu)$ is the density of photon states, and $\mathbf{a}^{\dagger}_{\vec{Q}\alpha}$ is the creation operator for a photon with wave vector $\vec{Q}$ and polarization $\hat{e}_\alpha$. Equation A4.3 can be rewritten as

$$\frac{|A^{+}_{n\to j}(\tau)|^2}{\tau} = \left[\frac{2\pi}{V_{EM}} \frac{e^2 (n_{\vec{Q}\alpha} + 1)\, \rho_{\vec{Q}\alpha}(h\nu)}{m_n^2\, \nu}\right] \delta(\hbar\omega_{nj})$$

$$\times\ |\langle \Phi_j | e^{-i\vec{Q}\cdot\vec{r}} \hat{e}_\alpha \cdot \mathbf{p} | \Phi_n \rangle|^2 \ .$$

For far field radiation (relative to EM wavelength), $\vec{Q} \cdot \vec{r} \ll 1$ and $\langle \Phi_j | e^{-i\vec{Q}\cdot\vec{r}} \hat{e}_\alpha \cdot \mathbf{p} | \Phi_n \rangle \approx \langle \Phi_j | \hat{e}_\alpha \cdot \mathbf{p} | \Phi_n \rangle$. Considering only the transitions from the lowest conduction band ($n = c$) to the two valence subbands ($j = 1, 2$) in zinc-blend semiconductors and using the matrix elements given in Appendix A4, the transition probability is

$$\frac{|A^{+}_{c\to j}(\tau)|^2}{\tau} = \left[\frac{2\pi}{V_{EM}} \frac{e^2 (n_{\vec{Q}\alpha} + 1)\, \rho_{\vec{Q}\alpha}(h\nu)}{m_c^2\, \nu}\right] \delta(\hbar\omega_{cj}) \zeta_j M_{cv}^2 \ , \quad \text{(A4.4)}$$

where M_{cv} is a constant, and $\xi_j \equiv 1, 3$, for $j = 1, 2$ respectively.

Using equations A4.4 and A4.2 in equation A4.1,

$$I(h\nu) = \left[\frac{G\, d\Omega\, d(h\nu)}{2\pi\hbar c^2} \frac{e^2}{\hbar c} (n_{\vec{Q}\,\alpha} + 1) M_{cv}^2\,(h\nu) \right] \sum_j \xi_j\, Z_j \quad , \qquad \text{(A4.5a)}$$

where

$$Z_j \equiv \int d^3\vec{k}_j \, \frac{dN_j}{d^3\vec{k}_j}\, Y_c \quad , \qquad \text{(A4.5b)}$$

and

$$Y_c \equiv \int d^3\vec{k}_c \, \frac{dN_c}{d^3\vec{k}_c} \left[\frac{m_c^{-2}\, \delta(h\nu - E_c(\vec{k}_c) + E_j(\vec{k}_j))}{\left[1 + e^{\beta_c (E_c(\vec{k}_c) - \mu_c)}\right]\left[e^{-\beta_j (E_j(\vec{k}_j) - \mu_j)} + 1\right]} \right] . \qquad \text{(A4.5c)}$$

To simplify calculations, the following (isotropic and parabolic) energy band structures are used:

$$E_c(\vec{k}_c) \equiv \frac{\hbar^2 k_c^2}{2m_c} \quad ;$$

and

$$E_j(\vec{k}_j) \equiv -E_g - \Delta_j - \frac{\hbar^2 k_j^2}{2m_j} = E_1 = -\left[E_g + \Delta_1 + \frac{\hbar^2 k_1^2}{2m_1} \right]$$

$$= E_2 = -\left[E_g + \Delta_2 + \frac{\hbar^2 k_2^2}{2m_2} \right] \quad ;$$

where m_c, m_1, and m_2 are the effect mass of the conduction electron, $v1$ hole, and $v2$ hole, respectively.

For $\vec{k}$-selection, $\vec{k}_c + \vec{k}_j + \vec{Q} = 0$. E_j can be written as $E_j(-\vec{k}_c - \vec{Q}) = -E_g - \Delta_j' - \frac{m_c}{m_j} E_c(\vec{k}_c)$, where $\Delta_j' \equiv \Delta_j + \frac{(h\nu)^2}{2m_j c^2} + \frac{\hbar^2}{m_j} \vec{k}_c \cdot \vec{Q}$. In

what follows, both the $h\nu$ dependence of Δ_j' and the energy difference between Δ_j' and Δ_j will be neglected. Since the bands are isotropic, $d^3\vec{k_c} = 4\pi k_c^2 dk_c = 2\pi (2m_c)^{3/2} \hbar^{-3} E_c^{1/2} dE_c$. Defining the reduced mass as $m_{rcj} \equiv \frac{m_c m_j}{m_c + m_j}$ and integrating Y_c over E_c yields

$$Y_c = \frac{V}{2\pi^2 m_c^2} \left[\frac{2m_{rcj}}{\hbar^2} \right]^{3/2} (h\nu - E_g - \Delta_j)^{1/2} f_j^c(h\nu) f_j^{ch}(h\nu) \quad , \qquad \text{(A4.6a)}$$

where

$$f_j^c(h\nu) = \left[1 + e^{\beta_c \left(\frac{m_{rcj}}{m_c} (h\nu - E_g - \Delta_j) - \mu_c \right)} \right]^{-1} \qquad \text{(4.4.14a)}$$

and

$$f_j^{ch}(h\nu) = \left[e^{\beta_j \left(\frac{m_{rcj}}{m_j} (h\nu - E_g - \Delta_j) + E_g + \Delta_j + \mu_j \right)} + 1 \right]^{-1} \quad . \qquad \text{(4.4.14b)}$$

Using $\eta_j n_{EHP} V_{EHP}$ ($= N_j$) to denote the number of holes in the $j^{\underline{th}}$ valence band,

$$I(h\nu) = I_o \sum_j \xi_j \left[\frac{m_{rcj}}{m_c} \right]^{3/2} \left[\frac{h\nu}{E_g} \right] \left[\frac{h\nu}{E_g} - \frac{\Delta_g}{E_j} - 1 \right]^{1/2}$$

$$\times \eta_j f_j^c(h\nu) f_j^{ch}(h\nu) \quad , \qquad \text{(4.4.13)}$$

where $I_o \equiv G \frac{2V \, d\Omega \, d(h\nu)}{(2\pi\hbar)^3} \frac{m_c c^2}{\hbar c} \frac{e^2}{\hbar c} \left[\frac{2E_g}{m_c c^2} \right]^{3/2} n_{EHP} M_{cv}^2$.

Note that for isotropic parabolic energy band structures, and consistent with the use of the Fermi function to approximate the carrier distribution, the quasi-Fermi levels are determined by the following:

1) conduction electron density,

$$n_c = \frac{1}{2\pi^2}\left[\frac{2m_c}{\hbar^2}\right]^{3/2}\left[\int_0^{\infty} dE \frac{\sqrt{E}}{1 + e^{\beta_c(E-\mu_c)}}\right] ;$$

2) v1 hole density,

$$n_1 = \frac{1}{2\pi^2}\left[\frac{2m_1}{\hbar^2}\right]^{3/2}\left[\int_{-\infty}^{-(E_g+\Delta_1)} dE \frac{\sqrt{-E-E_g-\Delta_1}}{e^{-\beta_1(E-\mu_1)}+1}\right]$$

$$= \frac{1}{2\pi^2}\left[\frac{2m_1}{\hbar^2}\right]^{3/2}\left[\int_0^{\infty} dx \frac{\sqrt{x}}{1 + e^{\beta_1(x-\mu_{r1})}}\right] ; \text{ and}$$

3) v2 hole density,

$$n_2 = \frac{1}{2\pi^2}\left[\frac{2m_2}{\hbar^2}\right]^{3/2}\left[\int_{-\infty}^{-(E_g+\Delta_2)} dE \frac{\sqrt{-E-E_g-\Delta_2}}{e^{-\beta_2(E-\mu_2)}+1}\right]$$

$$= \frac{1}{2\pi^2}\left[\frac{2m_2}{\hbar^2}\right]^{3/2}\left[\int_0^{\infty} dx \frac{\sqrt{x}}{1 + e^{\beta_2(x-\mu_{r2})}}\right] ;$$

where $\mu_{r1} = -(E_g + \Delta_1 + \mu_1)$ and $\mu_{r2} = -(E_g + \Delta_2 + \mu_2)$.

A5. Change in the Absorption Coefficient Under Stress

The stress dependent absorption coefficient has been given by Dutta[133] as

$$\alpha(h\nu) = A_o \int d^3k\ \delta\left[\frac{\hbar^2}{2\mu_{\|}}k_{\|}^2 + \frac{\hbar^2}{2\mu_{\perp}}k_{\perp}^2 - \Delta_1\right]\left[\frac{C_{\|}k_{\|}^2 + C_{\perp}k_{\perp}^2}{k_{\|}^2 + k_{\perp}^2}\right]$$

$$= A_o \int dk_{\|} \int 2\pi \left[\frac{2\mu_{\perp}}{\hbar^2}\right] \frac{d\left[\frac{\hbar^2}{2\mu_{\perp}}\right]k_{\perp}^2}{2}\ \delta\left[\frac{\hbar^2}{2\mu_{\perp}}k_{\perp}^2 - \left[\Delta_1 - \frac{\hbar^2}{2\mu_{\|}}k_{\|}^2\right]\right]$$

$$\times \left[\frac{\frac{\hbar^2}{2\mu_{\perp}}C_{\|}k_{\|}^2 + \frac{\hbar^2}{2\mu_{\perp}}C_{\perp}k_{\perp}^2}{\frac{\hbar^2}{2\mu_{\perp}}k_{\|}^2 + \frac{\hbar^2}{2\mu_{\perp}}k_{\perp}^2}\right],$$

where $\mu_{\|} \equiv \left[\frac{1}{m_{c\|}(X)} + \frac{1}{m_{1\|}(X)}\right]^{-1}$, $\mu_{\perp} \equiv \left[\frac{1}{m_{c\perp}(X)} + \frac{1}{m_{1\perp}(X)}\right]^{-1}$, $C_{\|} = \frac{4}{3}$,

$C_{\perp} = \frac{1}{3}$, and $\Delta_1 \equiv h\nu - E_1$. Integration yields

$$\alpha(h\nu) = A_o\pi\left[\frac{2\mu_{\perp}}{\hbar^2}\right]\int_{k_{z(-)}}^{k_{z(+)}} dk_{\|}\ \frac{\frac{\hbar^2}{2\mu_{\perp}}C_{\|}k_{\|}^2 + C_{\perp}\left[\Delta_1 - \frac{\hbar^2}{2\mu_{\|}}k_{\|}^2\right]}{\frac{\hbar^2}{2\mu_{\perp}}k_{\|}^2 + \left[\Delta_1 - \frac{\hbar^2}{2\mu_{\|}}k_{\|}^2\right]}$$

$$= A_o\pi\left[\frac{2\mu_{\perp}}{\hbar^2}\right]\int_{k_{z(-)}}^{k_{z(+)}} dk_{\|}\ \frac{C_{\perp}\left[1 + \frac{\hbar^2}{2\mu_{\perp}\Delta_1}\left[\frac{C_{\|}}{C_{\perp}} - \frac{\mu_{\perp}}{\mu_{\|}}\right]k_{\|}^2\right]}{1 + \frac{\hbar^2}{2\mu_{\perp}\Delta_1}\left[1 - \frac{\mu_{\perp}}{\mu_{\|}}\right]k_{\|}^2},$$

where $k_{z(\pm)} \equiv \pm\left[\frac{2\mu_{\|}\Delta_1}{\hbar^2}\right]^{1/2}$.

Making a change of variables ($k_{\|} \equiv \left[\frac{2\mu_{\|}\Delta_1}{\hbar^2}\right]^{1/2} z$),

$$\alpha(h\nu) = A_o\pi\left[\frac{2\mu_{\perp}}{\hbar^2}\right]C_{\perp}\int_{-1}^{+1}\left[\frac{2\mu_{\|}\Delta_1}{\hbar^2}\right]^{1/2}dz\ \frac{1+\frac{\hbar^2}{2\mu_{\perp}\Delta_1}\left[\frac{C_{\|}}{C_{\perp}}-\frac{\mu_{\perp}}{\mu_{\|}}\right]\frac{2\mu_{\|}\Delta_1}{\hbar^2}z^2}{1+\frac{\hbar^2}{2\mu_{\perp}\Delta_1}\left[1-\frac{\mu_{\perp}}{\mu_{\|}}\right]\frac{2\mu_{\|}\Delta_1}{\hbar^2}z^2}$$

$$= A_o\pi\left[\frac{2\mu_{\perp}}{\hbar^2}\right]\left[\frac{2\mu_{\|}\Delta_1}{\hbar^2}\right]^{1/2}C_{\perp}\int_{-1}^{+1}dz\ \frac{1+\left[\frac{C_{\|}}{C_{\perp}}\frac{\mu_{\|}}{\mu_{\perp}}-1\right]z^2}{1+\left[\frac{\mu_{\|}}{\mu_{\perp}}-1\right]z^2}$$

$$= A_o\frac{4\pi}{3}(\Delta_1)^{1/2}\left[\frac{2\mu_{\perp}}{\hbar^2}\right]^{3/2}\frac{\mu_{\|}}{\mu_{\perp}}\frac{3C_{\perp}}{4}2\int_0^1 dz\ \frac{1+\left[\frac{C_{\|}}{C_{\perp}}\frac{\mu_{\|}}{\mu_{\perp}}-1\right]z^2}{1+\left[\frac{\mu_{\|}}{\mu_{\perp}}-1\right]z^2}$$

$$= A_o\frac{4\pi}{3}(\Delta_1)^{1/2}\left[\frac{2\mu_{\perp}}{\hbar^2}\right]^{3/2}\frac{u}{2}\int_0^1 dz\ \frac{1+(4u-1)z^2}{1+(u-1)z^2}\ ,$$

where $u = \dfrac{\mu_{\|}(X)}{\mu_{\perp}(X)}$.

Note that without stress, $\mu_{\|}(X=0) = \mu_{\perp}(X=0) \equiv \mu_o$, $\mu_o^{-1} \equiv m_c^{-1} + m_1^{-1}$ (where m_c is the conduction band effective mass and m_1 is the v1 valence band effective mass). Therefore, $u = 1$, and

$$\alpha_o(h\nu) = A_o \frac{4\pi}{3}(\Delta^o)^{1/2}\left[\frac{2\mu_o}{\hbar^2}\right]^{3/2}\frac{1}{2}\int_0^1 dz\ \left[1 + 3z^2\right]$$

$$= A_o \frac{4\pi}{3}(\Delta^o)^{1/2}\left[\frac{2\mu_o}{\hbar^2}\right]^{3/2} ,$$

where $\Delta^o \equiv h\nu - E_g$.

From this, the change in the absorption coefficient as a function of stress is given by

$$\Delta\alpha(h\nu, X) = \left[\frac{\Delta_1(X)}{\Delta^o}\right]^{1/2}\left[\frac{\mu_\perp(X)}{\mu_o}\right]^{3/2}\frac{u}{2}\int_0^1 dz \frac{1 + (4u - 1)z^2}{1 + (u - 1)z^2} , \quad (4.5.9)$$

where $\Delta_1(X) \equiv \Delta^o - \Delta E_{c-v1}(X)$.

A6. Effective Lifetime

Defining τ_{eff} by $\bar{p}(\tau_{eff}) \equiv e^{-1}$,

$$\bar{p}(\tau_{eff}) \equiv e^{-1} = \left[(1 + b_A)\, e^{A\tau_{eff}} - b_A \right]^{-1} .$$

Rearranging,

$$e^{A\tau_{eff}} = \frac{e + b_A}{1 + b_A} .$$

Taking the log,

$$A\tau_{eff} = \ln\left[\frac{e + b_A}{1 + b_A} \right] .$$

Rearranging, yields

$$\tau_{eff} = \frac{1}{A} \ln\left[\frac{Ae + b}{A + b} \right] . \qquad (4.5.10a)$$

A7. List of Publications

1. High Power Picosecond Laser Induced Shock Waves in Condensed Matter, R. Rao, X. Z. Lu, A. G. Doukas, S. Lee, B. Willman, P. Harris, & R. R. Alfano, Proceedings of the International Conference on LASERS' 85, 171-177.

2. Light Emissions from GaSe Semiconductor under Picosecond-Laser-Induced Shock Pressure, R. Rao, X. Z. Lu, B. Willman, S. Lee, A. G. Doukas, & R. R. Alfano, Proceedings of the International Conference on LASERS' 86, 76-83.

3. Effect of Picosecond-Laser-Driven Shock Waves on Spontaneous and Stimulated Emission in GaSe, X. Z. Lu, R. Rao, B. Willman, S. Lee, A. G. Doukas, & R. R. Alfano, Phys. Rev. B 35, 7515 (1987).

4. Photoluminescence due to Exciton-Exciton Scattering in GaSe under Picosecond Laser Excitation, X. Z. Lu, R. Rao, B. Willman, S. Lee, A. G. Doukas, & R. R. Alfano, Phys. Rev. B 36, 1140 (1987).

5. Shock-Wave-Induced Collision Broadening of the Photoluminescence Spectra in GaSe, X. Z. Lu, S. Lee, R. Garuthara, & R. R. Alfano, Appl. Phys. Lett. 51, 1789 (1987).

6. Gallium Arsenide Photoluminescence under Picosecond-Laser-Induced Shock Compression, X. Z. Lu, R. Garuthara, S. Lee, & R. R. Alfano, Appl. Phys. Lett. 52, 93 (1988).

7. An Automated Data Collection System for Ultrafast Spectroscopy, B. Willman, S. Lee, A. G. Doukas, & R. R. Alfano, Am. Lab. 20, 23 (1988).

8. Shock-Wave Effect on the Electron-Hole Plasma in CdSe, R. Garuthara, X. Z. Lu, S. Lee, & R. R. Alfano, J. Appl. Phys. 64, 3737 (1988).

9. Effects of Picosecond-Laser-Driven Shock Waves on the Photoluminescence from Semiconductors, X. Z. Lu, R. Garuthara, S. Lee, & R. R. Alfano in Ultrafast Laser Probe Phenomena in Bulk and Microstructures II, SPIE Vol. 942, p157, 1988.

10. Picosecond-Laser-Driven Shock Wave Dynamics in Semiconductors, X. Z. Lu, R. Garuthara, S. Lee, & R. R. Alfano, in Ultrafast Phenomena VI, Ed. T. Yajima, K. Yoshihara, C. B. Harris, & S. Shionoya, p226, Springer-Verlag Berlin Heidelberg 1988.

11. Search for the Effect of Weak Photon Localization in Second-Harmonic Waves Generated in a Disordered Anisotropic Nonlinear Medium, K. M. Yoo, S. Lee, Y. Takiguchi, & R. R. Alfano, Optics Lett. 14, 800 (1989).

12. Picosecond Laser Generated Shock Profile in GaAs, S. Lee, X. Z. Lu, R. Garuthara, R. R. Alfano, & M. Dutta, submitted to Phys. Rev. B (1991).

13. Hole Lifetimes in [001] Uniaxial Stressed GaAs, S. Lee, K. M. Yoo, R. R. Alfano, H. Qiang, & F. H. Pollak, submitted to Phys. Rev. B (1992).

Bibliography

B1. References for Chapter 1

1. W. Paul, J. Phys. Chem. Solids **8**, 196, (1959).

2. S. D. Hamann, in *Advances in High Pressure Research*, Ed. R. S. Bradley, Vol. 1, pp. 85-137, Academic Press, New York, 1966.

3. F. H. Pollak, Surf. Sci. **37**, 863, (1973).

4. W. J. Murri, D. R. Curran, C. F. Petersen, and R. C. Gourley, in *Advances in High Pressure Research*, Ed. R. H. Wentorf, Jr., Vol. 4, pp. 1-163, Academic Press, 1974.

5. G. Martinez, in *Handbook on Semiconductors*, Ed. M. Balkanski & T. S. Moss, Vol. 2, pp. 181-222, North-Holland Publishing Co., 1980.

6. A. Jayaraman, Rev. Mod. Phys. **55**, 65, (1983).

7. F. H. Pollak, in *Semiconductors and Semimetals*, Ed. R. K. Willardson & A. C. Beer, Vol. 32, pp. 17-52, Academic Press, 1990.

8. F. H. Pollak and M. Cardona, Phys. Rev. **172**, 816, (1968).

9. A. C. Rose-Innes, Proc. Phys. Soc. **72**, 514, (1958).

10. C. P. Kuo, S. K. Vong, R. M. Cohen, and G. B. Stringfellow, J. Appl. Phys. **57**, 5428, (1985).

11. R. M. White, J. Appl. Phys. **34**, 2123, (1963).

12. P. S. Peercy, E. D. Jones, J. C. Bushnell, and G. W. Gobeli, Appl. Phys. Lett. **16**, 120, (1970).

B2. References for Chapter 2

13. J. F. Nye, in *Physical Properties of Crystals*, pp. 82-109, Oxford University Press, New York, 1986.

14. F. H. Pollak, in *Semiconductors and Semimetals*, Ed. R. K. Willardson & A. C. Beer, Vol. 32, pp. 17-52, Academic Press, 1990.

15. W. H. Kleiner and L. M. Roth, Phys. Rev. Lett. **2**, 334, (1959).

16. F. H. Pollak, M. Cardona, and K. L. Shaklee, Phys. Rev. Lett. **16**, 942, (1971).

17. M. Chandrasekhar and F. H. Pollak, Phys. Rev. B **15**, 2127, (1977).

18. H. Qiang, F. H. Pollak, and G. Hickman, Solid State Commun. **76**, 1087, (1990).

19. F. H. Pollak, Surf. Sci. **37**, 863, (1973).

20. L. D. Laude, F. H. Pollak, and M. Cardona, Phys. Rev. B **3**, 2623, (1971).

21. E. O. Kane, Phys. Rev. **178**. 1368, (1970).

22. R. N. Bhargava and M. I. Nathan, Phys. Rev. **161**, 695, (1967).

23. G. W. Arnold and D. K. Brice, Phys. Rev. **178**, 1399, (1969).

24. N. K. Dutta, J. Appl. Phys. **55**, 285, (1984).

25. N. K. Dutta and D. C. Craft, J. Appl. Phys. **56**, 65, (1984).

26. D. E. Aspnes and M. Cardona, Phys. Rev. B **17**, 726, (1978).

27. D. E. Aspnes and M. Cardona, Phys. Rev. B **17**, 741, (1978).

28. K. Suzuki and J. C. Hensel, Phys. Rev. B **9**, 4184, (1974).

29. J. C. Hensel and K. Suzuki, Phys. Rev. B **9**, 4219, (1974).

30. J. C. Hensel and G. Feher, Phys. Rev. **129**, 1041, (1963).

31. H. Hasegawa, Phys. Rev. **129**, 1029, (1963).

32. M. Cardona, Phys. Rev. **121**, 752, (1961).

33. F. H. Pollak and M. Cardona, Phys. Rev. **172**, 816, (1968).

34. C. S. Adams and D. T. Cassidy, J. Appl. Phys. **64**, 6631, (1988).

35. E. Anastassakis, A. Pinczuk, E. Burstein, F. H. Pollak, and M. Cardona, Solid State Commun. **8**, 133, (1970).

36. F. Cerdeira, C. J. Buchenauer, F. H. Pollak, and M. Cardona, Phys. Rev. B **5**, 580, (1972).

37. M. Hunermann, W. Richter, J. Saalmuller, and E. Anastassakis, Phys. Rev. B **34**, 5381, (1986).

38. J. M. Luttinger, Phys. Rev. **102**, 1030, (1956).

39. G. E. Pikus, Soviet Phys. — JETP **14**, 1075, (1962).

40. K. Cho, Phys. Rev. B **14**, 4463, (1976).

41. D. W. Langer, R. N. Euwema, K. Era, and T. Koda, Phys. Rev. B **2**, 4005, (1970).

42. A. J. Nilisk and J. J. Kirs, Phys. Stat. Sol. **31**, K91, (1969).

43. J. M. Besson, K. P. Jain, and A. Kuhn, Phys. Rev. Lett. **32**, 936, (1974).

44. S. I. Subbotin, V. V. Panfilov, and R. T. Molchanova, Phys. Stat. Sol. A **39**, 357, (1977).

45. G. L. Belenkii, E. Yu Salaev, R. A. Suleimanov, and E. I. Mirzoev, Sov. Phys. Solid State **22**, 1842, (1980).

46. R. H. Knell and D. W. Langer, Phys. Lett. **21**, 370, (1966).

47. P. Y. Yu and B. Welber, Solid State Commun. **25**, 209, (1978).

48. D. Olego, M. Cardona, and H. Muller, Phys. Rev. B **22**, 894, (1980).

49. M. Leroux, G. Pelous, F. Raymond, and C. Verie, Appl. Phys. Lett. **46**, 288, (1985).

50. A. R. Goni, K. Strossner, K. Syassen, and M. Cardona, Phys. Rev. B **36**, 1581, (1987).

51. C. Jagannath, S. Zemon, P. Norris, and B. S. Elman, Appl. Phys. Lett. **51**, 1268, (1987).

52. W. P. Dumke, Phys. Rev. **132**, 1998, (1963).

53. C. Trallero-Giner, A. Alexandrou, and M. Cardona, Phys. Rev. B **38**, 10744, (1988).

54. A. Alexandrou, C. Trallero-Giner, G. Kanellis, and M. Cardona, Phys. Rev. B **40**, 1013, (1989).

55. C. S. Smith, in *Solid State Physics*, Ed. F. Seitz & D. Turnbull, Vol. 6, pp. 175-249, Academic Press, 1958.

56. R. I. Cottam and G. A. Saunders, J. Phys. C **6**, 2105, (1973).

B3. References for Chapter 3

57. J. N. Bradley, in *Shock Waves in Chemistry and Physics*, pp. 16-18, John Wiley & Sons Inc., New York, 1962.

58. K. P. Leung, S. S. Yao, A. G. Doukas, P. Harris, and R. R. Alfano, Phys. Rev. B **31**, 942, (1985).

59. R. A. Graham, O. E. Jones, and J. R. Holland, J. Appl. Phys. **36**, 3955, (1965).

60. N. L. Coleburn, J. W. Forbes, and H. D. Jones, J. Appl. Phys. **43**, 5007, (1972).

61. G. Rosenberg, J. Phys. Chem. Solids **41**, 561, (1980).

62. V. N. Mineev, A. G. Ivanov, E. Z. Novitskii, Yu. N. Tyunyaev, and Yu. V. Lisitsyn, JETP Lett. **5**, 244, (1967).

63. V. N. Mineev, A. G. Ivanov, Yu. V. Lisitsyn, E. Z. Novitskii, and Yu. N. Tyunyaev, Sov. Phys. JETP **34**, 131, (1972).

64. J. D. Kennedy and W. B. Benedick, Solid State Commun. **5**, 53, (1967).

65. J. D. Kennedy and W. B. Benedick, J. Phys. Chem. Solids **27**, 125, (1966).

66. Z. P. Tang and Y. M. Gupta, APS Conference Proceeding on Shock Compression of Condense Matter **34**, 1734, (1989).

67. V. B. Mintsev, Yu. B. Zaporoghets, and V. E. Fortov, in *AIP Conference Proceeding 208 Current Topics in Shock Waves*, p. 208, 1990.

68. G. E. Duvall and G. R. Fowles, in *High Pressure Chemistry and Physics*, Ed. R. S. Bradley, pp. 209-287, Academic Press, New York, 1963.

69. V. A. Siminenko, APS Conference Proceeding on Shock Compression of Condense Matter **35**, 1850, (1991).

70. D. S. Hughes, L. E. Gourley, and M. F. Gourley, J. Appl. Phys. **32**, 624, (1961).

71. W. J. Murri, D. R. Curran, C. F. Petersen, and R. C. Gourley, in *Advances in High Pressure Research*, Ed. R. H. Wentorf, Jr., Vol. 4, pp. 1-163, Academic Press, 1974.

72. R. M. White, J. Appl. Phys. **34**, 2123, (1963).

73. P. S. Peercy, E. D. Jones, J. C. Bushnell, and G. W. Gobeli, Appl. Phys. Lett. **16**, 120, (1970).

74. F. Cottet, J. P. Romain, R. Fabbro, and B. Faral, Phys. Rev. Lett. **52**, 1884, (1984).

75. F. Cottet, M. Hallouin, J. P. Romain, R. Fabbro, B. Faral, and H. Pepin, Appl. Phys. Lett. **47**, 678, (1985).

76. B. P. Fairand and A. H. Clauer, J. Appl. Phys. **50**, 1497, (1979).

77. D. Salzmann, I. Gilath, and B. Arad, Appl. Phys. Lett. **52**, 1128, (1988).

78. C. T. Walters, APS Conference Proceeding on Shock Compression of Condense Matter **35**, 1827, (1991).

79. C. Thomsen, H. T. Grahn, H. J. Maris, and J. Tauc, Phys. Rev. B **34**, 4129, (1986).

80. A. Caruso and R. Gratton, Plasma Phys. **10**, 867, (1968).

81. W. C. Mead, E. M. Campbell, W. L. Kruer, R. E. Turner, C. W. Hatcher, D. S. Bailey, P. H. Y. Lee, J. Foster, K. G. Tirsell, B. Pruett, N. C. Holmes, J. T. Trainor, G. L. Stradling, B. F. Lasinski, C. E. Max, and F. Ze, Phys. Fluids **27**, 1301, (1984).

82. R. A. MacDonald and D. H. Tsai, Phys. Rep. **46**, 1, (1978).

83. W. Koechner, in *Solid-State Laser Engineering, Second Edition*, p. 367, Springer-Verlag, Berlin-Heidelberg, 1988.

84. B. Willman, S. Lee, A. G. Doukas, and R. R. Alfano, Am. Lab. **20**, 23, (1988).

B4. References for Chapter 4

85. X. Z. Lu, R. Rao, B. Willman, S. Lee, A. G. Doukas, and R. R. Alfano, Phys. Rev. B **35**, 7515, (1987).

86. X. Z. Lu, S. Lee, R. Garuthara, and R. R. Alfano, Appl. Phys. Lett. **51**, 1789, (1987).

87. T. J. Wieting and J. L. Verble, Phys. Rev. B **5**, 1473, (1972).

88. V. Capozzi, Phys. Rev. B **23**, 836, (1981).

89. Y. Yoshikuni, H. Saito, and S. Shionoya, Solid State Commun. **32**, 665, (1979).

90. T. Moriya and T. Kushida, J. Phys. Soc. Jpn **40**, 1668, (1976).

91. X. Z. Lu, R. Rao, B. Willman, S. Lee, A. G. Doukas, and R. R. Alfano, Phys. Rev. B **36**, 1140, (1987).

92. T. Moriya and T. Kushida, J. Phys. Soc. Jpn **40**, 1676, (1976).

93. V. V. Panfilov, S. I. Subbotin, L. F. Vereshchagin, I. I. Ivanov, and R. T. Molchanova, Phys. Status Solidi B **72**, 823, (1975).

94. A. Yariv, in *Introduction to Optical Electronics, Second Edition*, p. 93, Holt, Rinehart and Winston, New York, 1976.

95. K. P. Leung, S. S. Yao, A. G. Doukas, P. Harris, and R. R. Alfano, Phys. Rev. B **31**, 942, (1985).

96. T. Ugumori, K. Masuda, and S. Namba, J. Phys. Soc. Jpn **41**, 1991, (1976).

97. R. Garuthara, X. Z. Lu, S. Lee, and R. R. Alfano, J. Appl. Phys. **64**, 3737, (1988).

98. D. W. Langer, R. N. Euwema, K. Era, and T. Koda, Phys. Rev. B **2**, 4005, (1970).

99. J. L. Birman, Phys. Rev. **114**, 1490, (1959).

100. K. Cho, Phys. Rev. B **14**, 4463, (1976).

101. G. E. Pikus, Soviet Phys. — JETP **14**, 1075, (1962).

102. O. Madelung, in *Landolt-Börnstein Numerical Data and Functional Relationships in Science and Technology New Series Group III*, Ed. K.-H. Hellwege, Vol. 17a, p. 223, Springer-Verlag, Berlin-Heidelberg, 1986.

103. C. F. Cline, H. L. Dunegan, and G. W. Henderson, J. Appl. Phys. **38**, 1944, (1967).

104. X. Z. Lu, R. Garuthara, S. Lee, and R. R. Alfano, Appl. Phys. Lett. **52**, 93, (1988).

105. O. Madelung, in *Landolt-Börnstein Numerical Data and Functional Relationships in Science and Technology New Series Group III*, Ed. K.-H. Hellwege, Vol. 22a, p. 84, Springer-Verlag, Berlin-Heidelberg, 1987.

106. W. H. Kleiner and L. M. Roth, Phys. Rev. Lett. **2**, 334, (1959).

107. F. H. Pollak, Surf. Sci. **37**, 863, (1973).

108. R. I. Cottam and G. A. Saunders, J. Phys. C **6**, 2105, (1973).

109. E. O. Kane, J. Phys. Chem. Solids **1**, 82, (1956).

110. M. Chandrasekhar and F. H. Pollak, Phys. Rev. B **15**, 2127, (1977).

111. H. Qiang, F. H. Pollak, and G. Hickman, Solid State Commun. **76**, 1087, (1990).

112. D. D. Nolte, W. Walukiewicz, and E. E. Haller, Phys. Rev. Lett. **59**, 501, (1987).

113. J. H. Eggert, K. A. Goettel, and I. F. Silvera, Phys. Rev. B **40**, 5724, (1989).

114. K. Shum, Y. Takiguchi, J. M. Mohaidat, F. Liu, R. R. Alfano, and H. Morkoc, Appl. Phys. Lett. **56**, 2328, (1990).

115. F. H. Pollak and M. Cardona, Phys. Rev. **172**, 816, (1968).

116. H. B. Beeb and E. W. Williams, in *Semiconductors and Semimetals*, Ed. R. K. Willardson & A. C. Beer, Vol. 8, pp. 175-249, Academic Press, 1972.

117. H. J. Zarrabi, W. B. Wang, and R. R. Alfano, Appl. Phys. Lett. **46**, 513, (1985).

118. R. J. Nelson and R. G. Sobers, J. Appl. Phys. **49**, 6103, (1978).

119. M. Takeshima, Phys. Rev. B **23**, 6625, (1981).

120. J. I. Pankov, in *Optical Processes in Semiconductors*, p. 36, Dover Publications, Inc., New York, 1975.

121. J. S. Blakemore, J. Appl. Phys. **53**, R123, (1982).

122. Bo E. Sernelius, Phys. Rev. B **33**, 8582, (1986).

123. F. H. Pollak, in *Semiconductors and Semimetals*, Ed. R. K. Willardson & A. C. Beer, Vol. 32, pp. 17-52, Academic Press, 1990.

124. N. K. Dutta and D. C. Craft, J. Appl. Phys. **56**, 65, (1984).

125. N. K. Dutta, J. Appl. Phys. **55**, 285, (1984).

126. O. Madelung, in *Landolt-Börnstein Numerical Data and Functional Relationships in Science and Technology New Series Group III*, Ed. K.-H. Hellwege, Vol. 17a, p. 223, Springer-Verlag, Berlin-Heidelberg, 1985.

127. M. Capizzi, S. Modesti, A. Frova, J. L. Staehli, M. Guzzi, and R. A. Logan, Phys. Rev. B **29**, 2028, (1984).

128. J. Shah, R. F. Leheny, and C. Lin, Solid State Commun. **18**, 1035, (1976).

129. K. Shum, P. P. Ho, R. R. Alfano, D. F. Welch, G. W. Wicks, and L. F. Eastman, Phys. Rev. B **32**, 3806, (1985).

130. C. Mailhiot and D. L. Smith, Phys. Rev. B **36**, 2942, (1987).

131. C. Jagannath, S. Zemon, P. Norris, and B. S. Elman, Appl. Phys. Lett. **51**, 1268, (1987).

B5. References for Appendix

132. H. B. Beeb and E. W. Williams, in *Semiconductors and Semimetals*, Ed. R. K. Willardson & A. C. Beer, Vol. 8, pp. 175-249, Academic Press, 1972.

133. N. K. Dutta, J. Appl. Phys. **55**, 285, (1984).